Adsorption Science & Technology

Biogeochemical Processes, Interactions, and Control of Pollutants in Soil-Plant Systems 2022

Lead Guest Editor: Linchuan Fang
Guest Editors: Hai-Bo Qin, Haijian Bing, Huihui Du, Qiaohui Fan, and Xue-Tao Guo

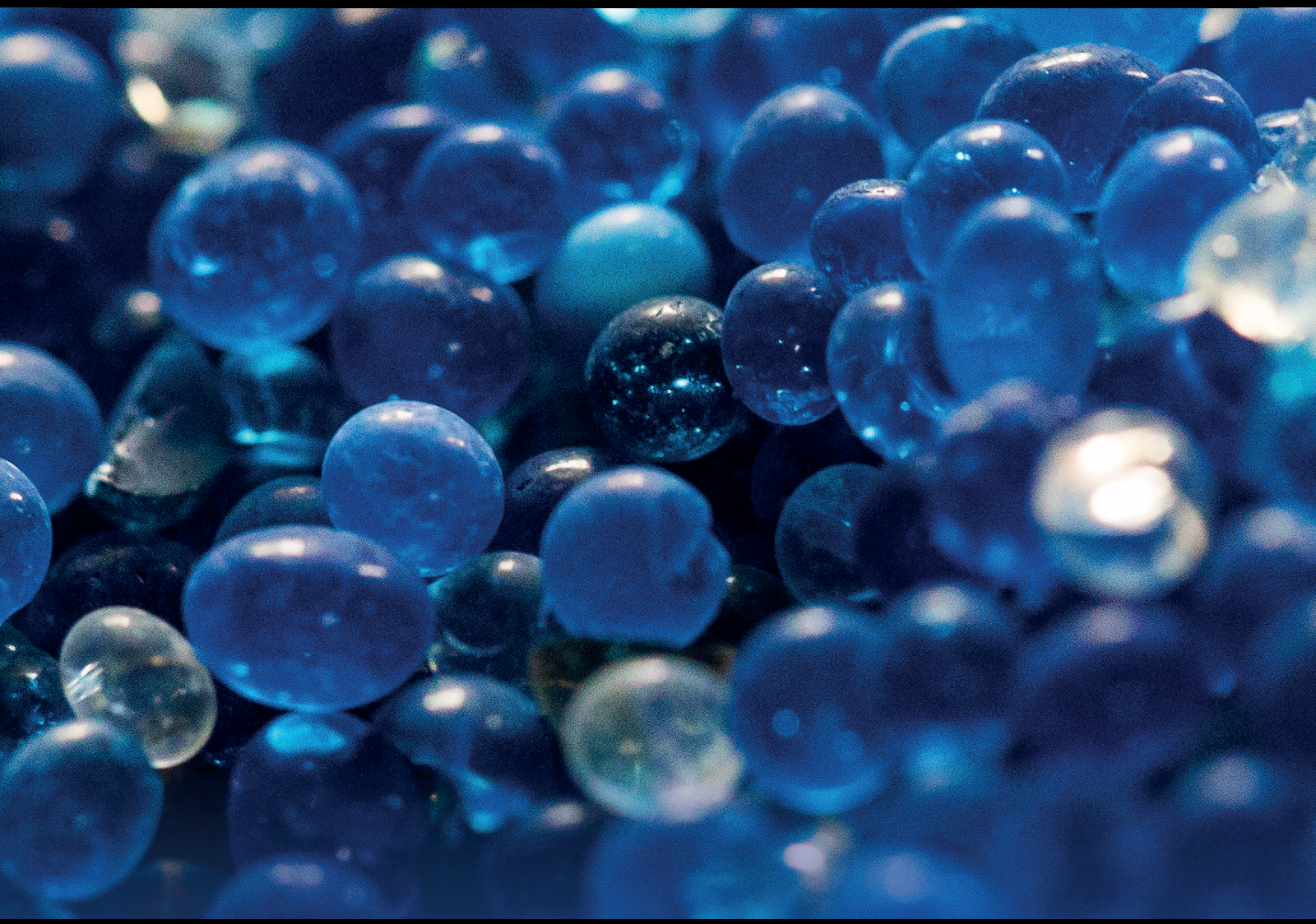

Biogeochemical Processes, Interactions, and Control of Pollutants in Soil-Plant Systems 2022

Adsorption Science & Technology

Biogeochemical Processes, Interactions, and Control of Pollutants in Soil-Plant Systems 2022

Lead Guest Editor: Linchuan Fang
Guest Editors: Hai-Bo Qin, Haijian Bing, Huihui Du, Qiaohui Fan, and Xue-Tao Guo

Contents

Hindawi
Adsorption Science & Technology
Volume 2023, Article ID 4539075, 12 pages
https://doi.org/10.1155/2023/4539075

Research Article

Uptake and Translocation of Cesium in Lettuce (*Lactuca sativa* L.) under Hydroponic Conditions

Leiping Shi,[1,2,3] Longmiao Yuan,[1,2,3] Ruijie Li,[1,2,3] Wei Wang,[1,2,3] Zhe Ding,[1,2,3] Jianjun Liang,[1,2,4] Junli Qiu,[1,2] and Ping Li[1,2,4]

[1]*Northwest Institute of Eco-Environment and Resources, Chinese Academy of Sciences, Lanzhou 730000, China*
[2]*Key Laboratory of Petroleum Resources, Gansu Province, Lanzhou 730000, China*
[3]*University of Chinese Academy of Sciences, Beijing 100049, China*
[4]*Key Laboratory of Strategic Mineral Resources of the Upper Yellow River, Ministry of Natural Resources, Lanzhou 730000, China*

Correspondence should be addressed to Ping Li; liping@lzb.ac.cn

Received 31 August 2022; Revised 24 October 2022; Accepted 24 November 2022; Published 6 February 2023

Academic Editor: Haijian Bing

The uptake of radiocesium (RCs) by plants is key to the assessment of its environmental risk. However, the transfer process of RCs in the water-vegetable system still remains unclear. In this work, the uptake and accumulation processes of Cs^+ (0-10 mM) in lettuce were explored under different conditions by using hydroponics. The results showed that the higher exposure concentration of Cs^+ could lead to a faster uptake rate and would be beneficial to the uptake and accumulation of Cs^+. The uptake of K^+ by roots and leaves was inhibited significantly when Cs^+ concentration increased, but unapparent for Ca^{2+} and Mg^{2+}. It was found that the higher K^+ and Ca^{2+} concentration was, the higher inhibition was found for the uptake of Cs^+ in root. The uptake of Cs^+ leads the decrease of chlorophyll content and brought a negative effect on plant photosynthesis, consequently, a negative effect on lettuce morphology and obvious decrease of biomass and root length. The contents of glutathione (GSH), malondialdehyde (MDA), and root vitality were increasing during the growth following stress of high concentrations of Cs^+, which caused stresses on the antioxidant system of lettuce. The enrichment coefficient for Cs^+ in leaves was in the range of 8-217. Moreover, the transfer factor was in the range of 0.114-0.828, which suggested that the high Cs^+ concentration could enhance the transfer of Cs^+ from lettuce root to leaf. This study provides more information on the transfer of RCs from water to food chain, promoting the understanding of the potential risk of RCs.

1. Introduction

Radiocesium (RCs) is one of the typical and important fission products of uranium in terms of the high fission yield (~10%), with low melting temperature and long half-life. Due to the high radiotoxicity and mobility, RCs is easy to transfer in the environment and accumulate in the food chain, which would possibly induce harm to the whole ecological environment. In the environment, the sources of RCs mainly include the nuclear weapon tests, the leakage of nuclear facility sites, and the nuclear accidents such as Chernobyl and Fukushima. In addition to RCs, the stable cesium also has a certain harm to the environment, mainly originating from the industrial production activities, such as the processes of mining and milling and the production of crushed cesium grenade ore [1]. Moreover, the natural erosion and weathering of rock could also contribute to the accumulation of Cs in water (including ground and surface water) and soil [2].

In the environment, RCs and the stable cesium could enter plants through the roots growing in contaminated water and soil [3]. In general, the translocation of RCs from soil to plants should experience the soil-water, soil-plant, and water-plant interfaces, in which the water-plant interface is extremely important to the migration and translocation of RCs. Plant roots take up Cs^+ from the soil solution firstly and then transported simplistically to the xylem [4]. Due to the similar chemical properties to K^+, there is a relatively high competitive effect between K^+ and Cs^+ at binding sites in proteins [5]. In addition, Cs^+ could inhibit the inward-rectifying potassium channels in the plasma membranes of plant cells, e.g., *AtAKT1* in Arabidopsis (*Arabidopsis thaliana*) [4, 6]. Theoretical

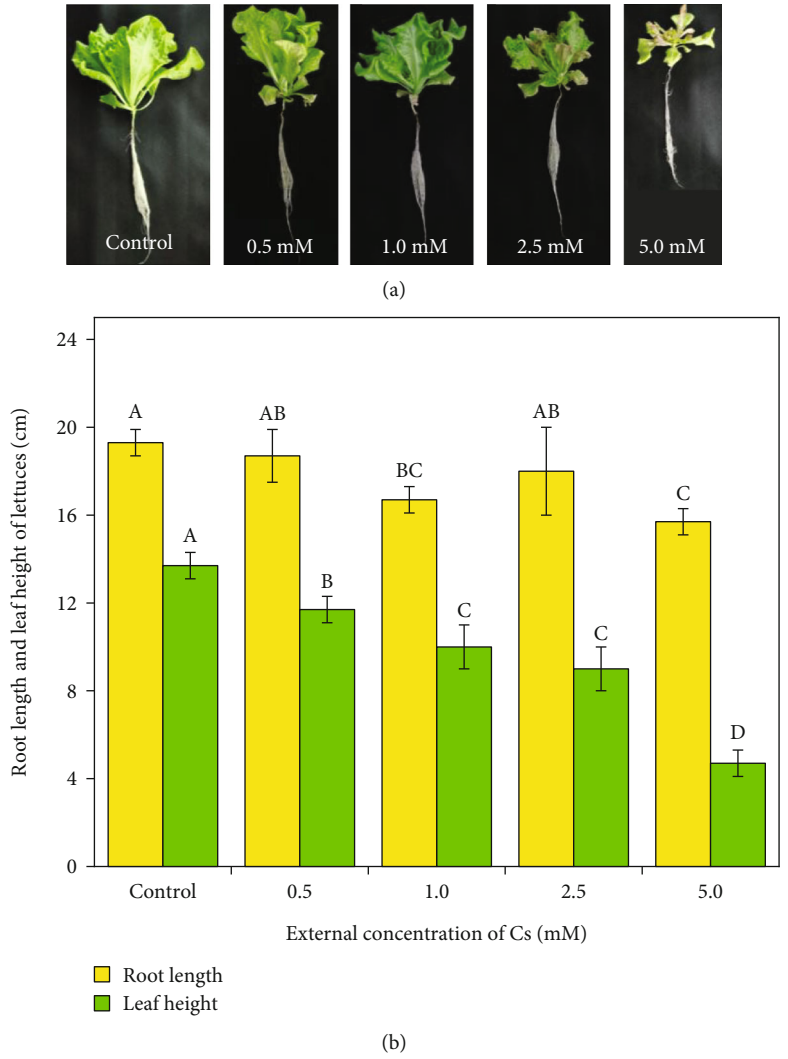

FIGURE 1: Effects of Cs^+ exposure on lettuce root lengths and leaf height. Notes: the different lowercase letters indicate that significant differences ($P < 0.05$) exist between treatment groups with different Cs levels in lettuce (LSD test).

models suggest that, in K-replete plants, the influx of Cs^+ to root cells is predominant through voltage-insensitive cation channels (*VICCs*), with "high-affinity" K1/H1 symporters transporting the remainder [4]. In fact, cesium is not a nutrient element required for the plant growth, and the cells in plant could be damaged due to the radiation of RCs [7]. It is reported that Cs^+ exhibited an obvious phytotoxicity when its concentration was higher than 0.2 mM [4, 8]. Previous studies have confirmed that the accumulation of stable Cs could result in a harmful reaction in plants, which would affect physiological and metabolic processes of plants such as growth, photosynthetic reactions, and genetics [9–12].

Transfer factor (TF) is a macroscopic parameter that integrates soil chemical, biological, hydrological, physical, and plant physiological processes. In a simple model, these transfer parameters represent the ratio of radionuclide concentrations in roots and shoot parts. To determine the radiological impacts, it is essential to understand the uptake and translocation processes and pathways in the soil-plant system. Generally, plants do not discriminate stable and radioactive cesium. Therefore, a high correlation about TFs was frequently observed for ^{133}Cs, ^{134}Cs, and ^{137}Cs [13, 14]. Consequently, the long-term transfer processes of RCs could be predicted well by using the transfer of stable Cs from water and soil to plants. A high distribution correlation between ^{137}Cs and ^{133}Cs in plants showed no significant difference in the uptake of RCs and stable Cs in sunflower. Thus, the uptake patterns of ^{137}Cs and ^{133}Cs are similar in plants [13].

Vegetable is an important medium and a key link for the transmission of mineral elements in the natural environment to humans. Lettuce (*Lactuca sativa* L.) is a popular leafy vegetable and is available worldwide. Lettuce is a good model for identifying determinants controlling cesium accumulation in plant tissues and developing breeding strategies aimed at limiting heavy metal accumulation in edible tissues [15]. In this work, we conducted hydroponic experiments of lettuce by using stable cesium at different treatment conditions. The objective of the cultivation experiment was to elucidate the effects of various factors on Cs^+ uptake and migration, such as Cs^+ concentration, the growth time, and the coexisting ions. Moreover, we attempted to evaluate the

Table 1: Effects of exposure to Cs^+ on biomass of lettuce.

Cs treatment (mM)	Leaf fresh weight (g)	Root fresh weight (g)	Leaf dry weight (g)	Root dry weight (g)
0	42.447 ± 10.96^a	3.247 ± 0.513^a	2.604 ± 0.526^a	0.247 ± 0.066^a
0.005	34.853 ± 2.491^a	2.747 ± 0.264^a	2.318 ± 0.211^a	0.207 ± 0.026^{ab}
0.05	36.100 ± 4.603^a	3.183 ± 0.619^a	2.659 ± 0.055^a	0.239 ± 0.039^a
0.5	37.537 ± 7.342^a	3.227 ± 0.567^a	2.403 ± 0.524^a	0.222 ± 0.037^a
1.0	31.230 ± 0.142^a	2.640 ± 0.529^a	2.062 ± 0.197^b	0.183 ± 0.036^{abc}
5.0	18.710 ± 5.779^b	1.523 ± 0.701^b	1.370 ± 0.423^b	0.118 ± 0.034^c
10.0	16.207 ± 2.199^b	1.490 ± 0.191^b	1.438 ± 0.322^b	0.132 ± 0.026^{bc}

Values are mean ± SD ($n = 3$ individual plants). The same letters and ns indicate no significant difference at the 5% level by Tukey's multiple range test.

potentiality of Cs^+ entering plants by enrichment coefficient (EC) and TF.

In this study, our work enhanced the understanding of the migration of RCs through the environment to food chain. It will have a well prediction to the potential risk of RCs for the human health in the future.

2. Materials and Methods

2.1. Plant Culture and Nutrient Solution. Lettuce seeds were purchased from Mianyang Huaxia Modern Seed Industry Co., Ltd. In this work, lettuce seeds were sterilized with 0.5% NaClO for five minutes and germinated on the filter paper in a suitable temperature, humidity, and avoidance environment in a greenhouse. And then, lettuce seeds were transplanted in the plastic containers ($12 \times 8 \times 10$ cm in length, width, and height) with Hoagland's nutrient solution. The nutrient solution (pH ~6.0) contained 2.0 mM $MgSO_4$, 5.0 mM $Ca(NO_3)_2 \cdot 4H_2O$, 5.0 mM KNO_3, 1.0 mM KH_2PO_4, and micronutrients (i.e., 4.0 μM $MnCl_2 \cdot 4H_2O$, 0.40 nM $Na_2MoO_4 \cdot 2H_2O$, 0.8 nM $ZnSO_4 \cdot 7H_2O$, 45 nM H_3BO_3, 0.3 nM $CuSO_4 \cdot 5H_2O$, and 0.02 mM $C_{10}H_{12}FeN_2NaO_8$). The growth conditions of lettuce were at $25 \pm 2 \circ C$, $50\% \pm 5$ humidity, and photocycle of 12 h light and 12 h dark. The photon flux density during the light period was 1600 $\mu mol\, m^{-2}\, s^{-1}$.

2.2. Hydroponic Experiments

2.2.1. Effects of Cs^+ Dose and Growth Time. Serial culture solutions with different Cs^+ concentrations were prepared in this study, where Cs^+ concentrations were in the range of 0 ~ 10 mM. After lettuce was transferred into nutrient solution after growing to 10 cm in height, the culture solution was replenished every 3 days and maintained at a volume of 0.8 L. At 3, 6, 9, 12, 15, 18, and 21 days after transplanting, lettuce plants were harvested, and then, the roots were rinsed for five times with tap water and deionized water, respectively. The harvested lettuce was separated into leaf and root parts and followed by dried with 48 h in oven at 75°C. Each treatment was carried out with three replicates and four plants per repetition. Taking Cs^+ concentration and growth time as regulation factors, there were 7 treatment groups, respectively, 49 treatment groups in total.

2.2.2. Effects of Na^+, K^+, and Ca^{2+} on Uptake of Cs^+. High (1.0 mM) and low (0.1 mM) Cs^+ concentrations were selected to estimate the effects of Na^+, K^+, and Ca^{2+} on lettuce here. Na^+, K^+, and Ca^{2+} were results from NaCl, KNO_3, and $Ca(NO_3)_2$ solutions. The concentrations of cation were in the range of 0 ~ 10 mM. Lettuces were cultivated in a completely hydroponic solution firstly. When lettuce grew to 10 cm for each seedling, the cultivate solutions were replaced with different concentrations of Na^+, K^+, and Ca^{2+} that contained Cs^+. Lettuce plants were harvested from each group at 21 days after adding cesium.

2.3. Determination of Cs^+ Concentration. In order to determine Cs^+ content in plants, the dried lettuces were incinerated in muffle furnace at 550°C and grounded into powder for further analysis. Approximate 250 mg powder sample was digested in polytetrafluoroethylene tank with a mixed digestion solution (including 2.0 mL HNO_3 and 1.0 mL H_2O_2), and then, the polytetrafluoroethylene tanks were heated for 24 h in baking oven at 195°C. After that, the pH of each sample was set between 3 and 4, and then, the dissolved lettuce samples were diluted to 10 mL. Supernatants were passed through a 0.45 μm filter. The contents of Cs^+ in leaves and roots were determined by using ion chromatography (Thermo Scientific ICS-600).

2.4. Calculation of Enrichment Coefficient and Transfer Factor. Enrichment coefficient (EC) and transfer factor (TF) were calculated using the following formula:

$$\mathrm{EC} = \frac{C_{\text{leave part}}}{C_{\text{culture solution}}}, \quad (1)$$

$$\mathrm{TF} = \frac{C_{\text{leave part}}}{C_{\text{root part}}}, \quad (2)$$

where $C_{\text{leave part}}$ is the concentration ($mg\, g^{-1}$, with respect to dry weight (dw)) of Cs^+ in leave, $C_{\text{culture solution}}$ is the concentration ($mg\, kg^{-1}$) of Cs^+ in culture solution, and $C_{\text{root part}}$ is the concentration ($mg\, g^{-1}$, dw) of Cs^+ in root.

2.5. Statistical Analysis. The data obtained in the experiments were subjected to one-way analysis of variance (ANOVA) with Tukey's multiple range test to determine the significance of the difference between the mean values using SPSS software. Correlation analysis was performed using a bivariate Pearson test, and the differences were considered statistically significant when $P < 0.05$.

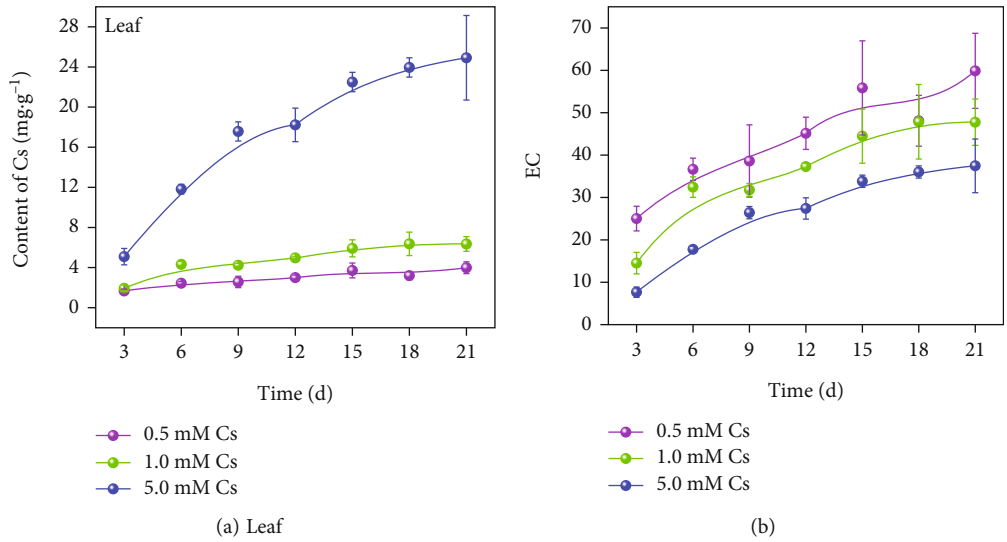

Figure 2: Analysis of the uptake process of cesium in lettuce leaves. (a) was the uptake kinetics of cesium. (b) was the enrichment coefficient of cesium.

3. Results and Discussion

3.1. Effect of Cs^+ Stress on Lettuce Growth. As shown in Figure 1(a), when Cs^+ concentration was higher than 2.5 mM, lettuce leaves appeared withered symptoms and leaf area was significantly reduced. The biomass of lettuces was decreased obviously as revealed in Table 1. Figure 1(b) shows the growth conditions of lettuce root and leaf, and the results indicated that the root length of lettuce was shorter than in the control group and another two groups with 1.0 and 5.0 mM Cs^+, respectively. The leaf height of lettuce was obviously decreasing with the concentration of Cs^+ increased from 0 to 5.0 mM. It could be seen from Section 3.5 that when the concentrations of Cs^+ were greater than 0.5 mM, the chlorophyll content was significantly decreased, which might lead to the inhibition of plant photosynthesis. Therefore, lettuce growth was significantly inhibited under Cs^+ stress, which could be attributed to the disruption of Cs^+ on the enzymatic activity and cellular structure [7]. Previous reports have found that high Cs^+ concentrations could inhibit the growth and the development of *Arabidopsis thaliana*, and the seed germination was reduced with 1.0 mM Cs^+ treatment. Moreover, low Cs^+ concentrations ranged from 500 to 700 μM could cause seedlings to start showing signs of chlorosis [16]. Jung et al. [17] also found that not only chlorosis appeared in specific parts of leaves but also the elongation of primary roots and root hairs was delayed when *Arabidopsis thaliana* was treated with 10 mM CsCl.

As shown in Figure 2(a), the Cs^+ content in leaves treated with 5.0 mM Cs^+ is significantly higher than that in 0.5 mM and 1.0 mM Cs^+. Moreover, the concentration of Cs^+ in leaves obviously increased with the increasing growth time and showed the faster uptake rate at 5.0 mM Cs treatment. It was in accordance with the previous findings that the uptake rate of Cs^+ increased with the increasing biomass of *Napier grass* [18]. As shown in Figure 2(b), the lower Cs^+ level was, the higher EC was observed, and it was more conducive to the enrichment of cesium in lettuce at a long growth time. However, it was noted that the enrichment efficiency of Cs^+ remained a similar level even under various treatment concentrations.

3.2. Evolution of Cs Distribution in Lettuce. As shown in Figures 3(a) and 3(b), the contents of K^+ in lettuce leaf and root obviously decreased with the increase of Cs^+ concentration, while both Mg^{2+} and Ca^{2+} contents did not change significantly. The result indicated that Cs^+ could regulate the uptake of K^+ in terms of the competitive uptake of Cs^+ and K^+. Both Mg^{2+} and Ca^{2+} are alkaline metal elements, and their chemical properties are quite different from Cs^+. In fact, K^+ transport channel has a low affinity to Mg^{2+} and Ca^{2+}; therefore, as expected, there is no obvious influence of Cs^+ and K^+ on the uptake of Mg^{2+} and Ca^{2+} by lettuce. Some previous researches have confirmed that the influx of Cs^+ into root cells was mainly mediated by the alkaline cations, especially for K^+ [4, 19, 20]. Our results confirmed that the stress of Cs^+ could indirectly regulate the uptake of K^+ due to the similar chemical and physical characteristic of Cs^+ and K^+. Sahr et al. [16] found that the transport of K^+ through its transport channels was probably inhibited in the presence of higher Cs^+ levels in leaves, as it was reviewed by [4]. Le Lay et al. [21] observed differences in Cs^+ distribution (1.0 mM) in cells and tissues of plant leaves grown in K-depleted and K-sufficient medium (i.e., 0 and 20.0 mM K^+) and proposed that both elements competed for entry inside plant.

The distribution of Cs^+ in roots and leaves under different culture times is shown in Figures 3(c) and 3(d). The contents of Cs^+ in roots and leaves increased significantly with the increase of culture times under all the Cs^+ treated groups. In general, Cs^+ uptake strongly depends on the plant developmental state, and the interception efficiency of Cs^+ is much higher in mature plants and old leaves [22, 23]. Moreover, it is noted that the content of Cs^+ in roots was much higher than that in leaves at the same culture time in this work (Figures 3(c) and 3(d)), which indicated that more

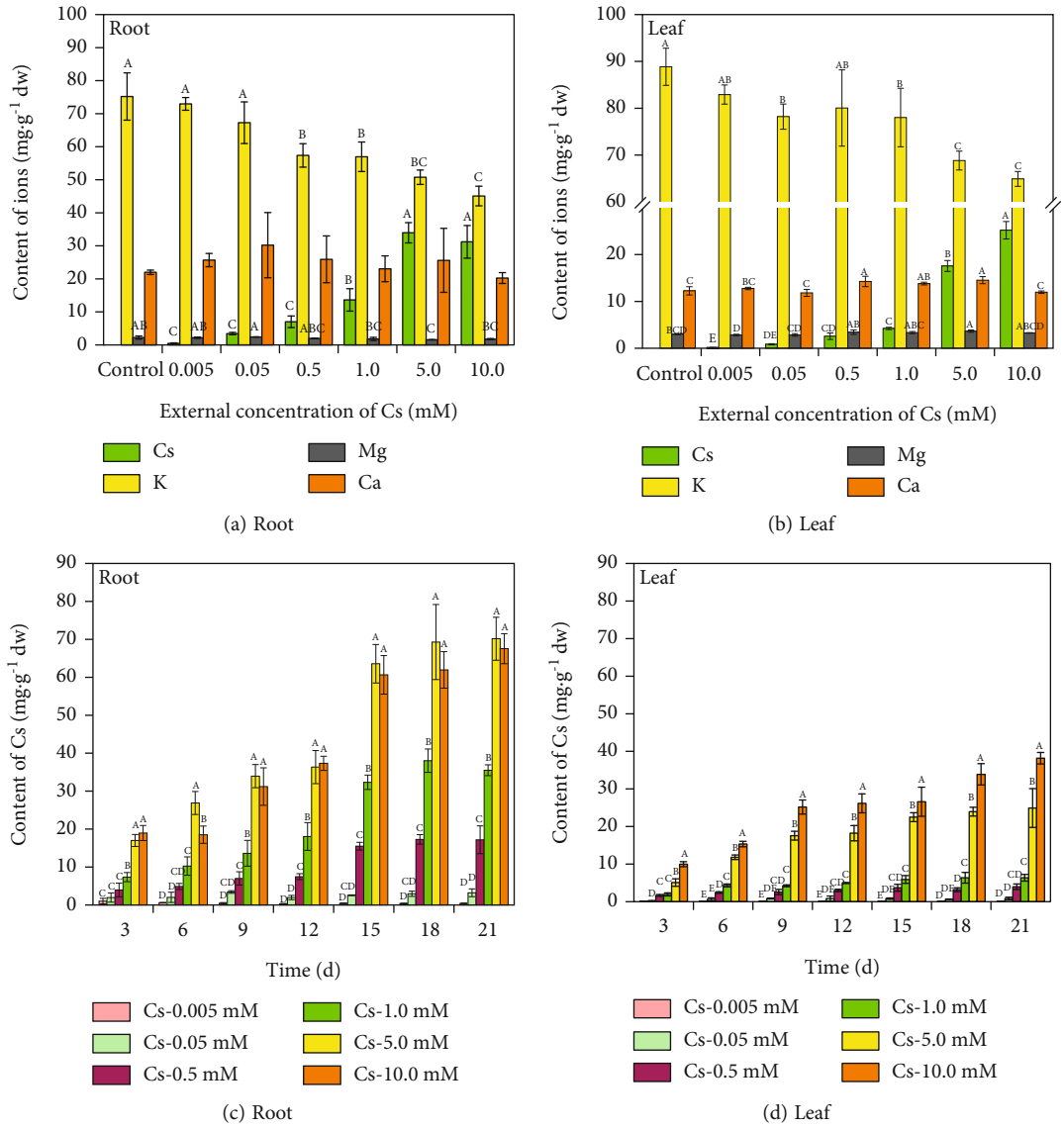

Figure 3: Effects of different Cs^+ concentrations and sampling time on the content of each element (Cs, K, Mg, and Ca) in lettuce. (a) and (c) represented changes of element content in root. (b) and (d) represented changes of element content in leaf. Notes: the different lowercase letters indicate that significant differences ($P < 0.05$) exist between treatment groups with different Cs levels in lettuce (LSD test).

Cs^+ would be transferred from root to leaf. An interesting phenomenon was observed that the content of Cs^+ in roots showed a slight decrease when Cs^+ concentration was higher than 5.0 mM (Figures 3(a) and 3(c)). It was possibly due to the fact that high Cs^+ concentration benefits to the accumulation of Cs^+ on/in the root epidermis and cell wall; the Cs^+ concentration in this position is much higher than outer solution, which resulted in the inhibition of Cs^+ uptake. Another possibility was that the water loss and ion channel destruction of root parts further decreased the uptake of Cs^+. However, the content of Cs^+ in leaves still increased even at Cs^+ concentration of 10 mM, possibly because Cs^+ entered in root vascular bundle which was continuing to transport upward under transpiration power in lettuces.

3.3. Regulation of Cations on Cs^+ Uptake and Distribution. Previous researches have reported that K^+, NH_4^+, Ca^{2+}, and Mg^{2+} have an obvious effect on the uptake of plants to RCs [24, 25]. Figure 4 and Figure S1 show the effects of Na^+, K^+, and Ca^{2+} on the uptake and distribution of Cs^+ in lettuce. As shown in Figures 4(a) and 4(b), the contents of Cs^+ in roots and leaves firstly increased in the K^+ concentration range of 0-0.5 mM and then decreased when K^+ concentration was greater than 0.5 mM. The function of uptake and metabolism of K^+ was normal under the low K^+ concentration treatment, so as the K^+ content increased, the uptake of Cs^+ increased. However, when K^+ concentration was too high, there was a competition between K^+ and Cs^+. Moreover, root activities and metabolic functions were inhibited, resulting in a decrease in Cs^+ content. K^+ concentration in the external medium clearly affected the uptake efficiency of Cs^+. The result was consistent with the previous molecular studies indicating the role of the high-affinity K^+ carrier *AtHAK5* in Cs^+ uptake under K-deprivation [26]. In fact, the discrimination of plants to Cs^+

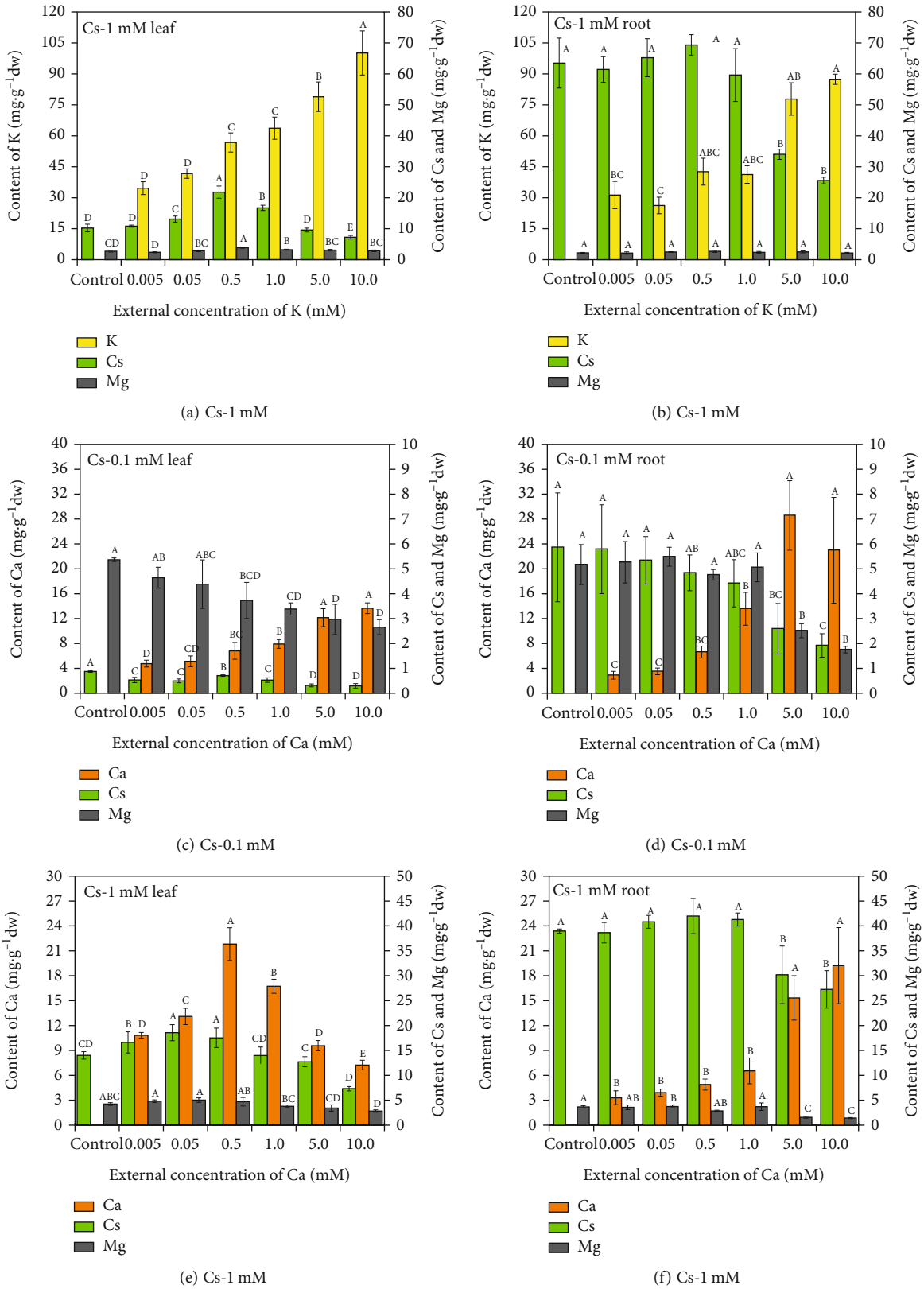

Figure 4: The effect of different concentrations of K^+ and Ca^{2+} on the uptake of different ion in lettuces. (a) Cs-1 mM, leaf;and (b) Cs-1 mM, root; were ion contents in the leaves and roots of lettuces treated with K^+ under 1 mM Cs treated. (c) Cs-0.1 mM, leaf; and (d) Cs-0.1 mM, root; were ion contents in the leaves and roots of lettuces treated with Ca^{2+} under 0.1 mM Cs treated. (e) Cs-1 mM, leaf; and (f) Cs-1 mM, root. were ion content in the leaves and roots of lettuces treated with Ca^{2+} under 1 mM Cs treated. Notes: the different lowercase letters indicate that significant differences ($P < 0.05$) exist between treatment groups with different Cs levels in lettuce (LSD test).

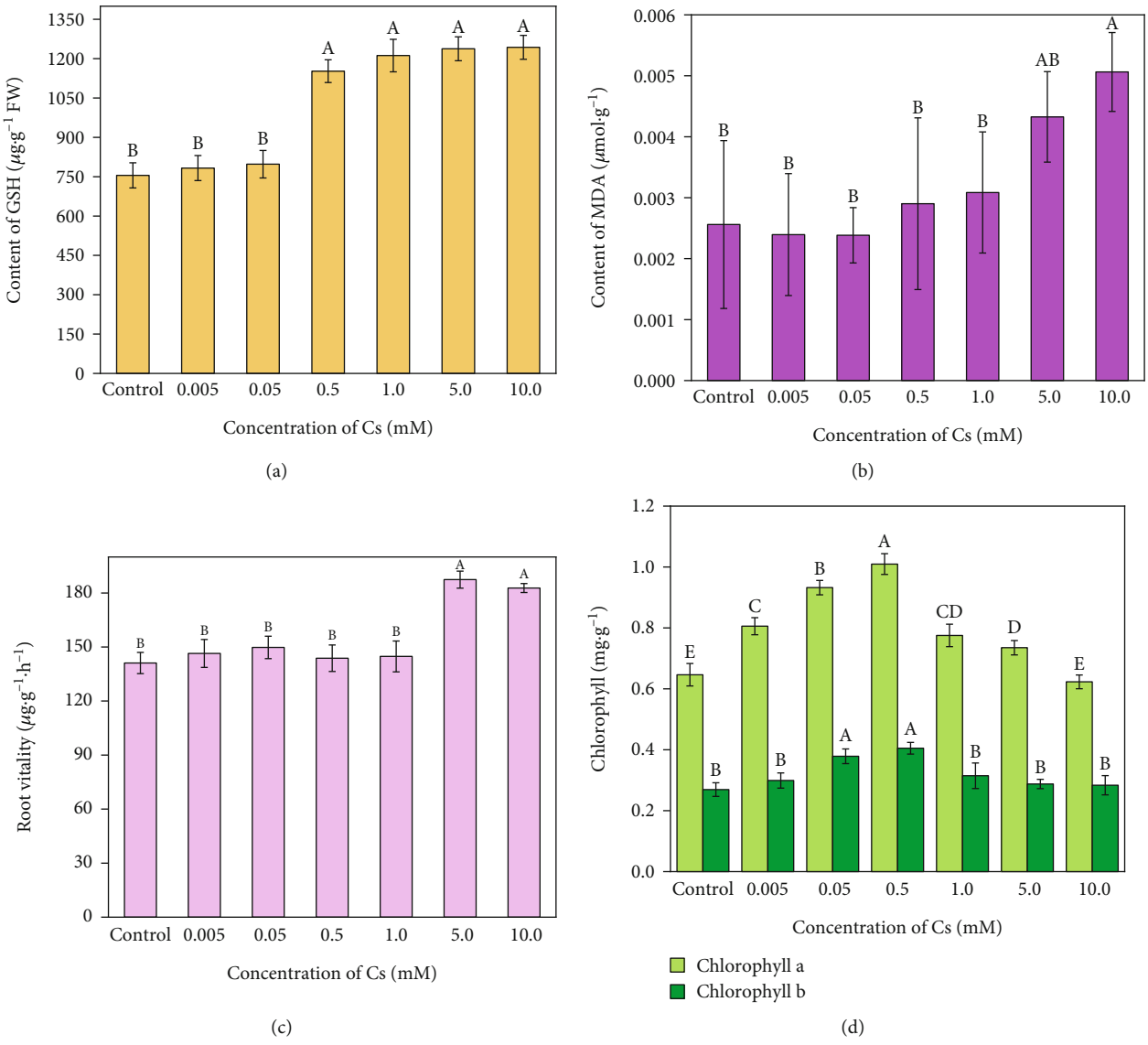

Figure 5: Response of plant physiological indicators to Cs^+ stress. (a–d) The contents of glutathione (GSH), malondialdehyde (MDA), root vitality, and chlorophyll a and chlorophyll b. Notes: the different lowercase letters indicate that significant differences ($P < 0.05$) exist between treatment groups with different Cs levels in lettuce (LSD test).

and K^+ was obviously declining with the decreasing of concentrations of Cs^+ and K^+ due to their similar physiochemical characteristics [27]. Moreover, a large amount of Cs^+ distributed in the cell wall at the low external K^+ concentration, which was also ascribed to the similar adsorption affinity of Cs^+ and K^+ on the root surface [28]. Isaure et al. [29] found that cesium distribution was similar to potassium in *Arabidopsis thaliana* through microfocused synchrotron-based X-ray fluorescence analysis. Both Cs^+ and K^+ were mainly concentrated on the vascular system of stems and leaves, which suggested that Cs^+ could compete with K^+ binding sites in cells [29].

As shown in Figure 4(c), the maximum Cs^+ content in leaves was below 1.0 mg g^{-1} at 0.1 mM Cs^+ treatment group, and Ca^{2+} could slightly inhibit the uptake of Cs^+ in the leaves. However, the content of Cs^+ in roots obviously decreased from ~6.0 mg g^{-1} to ~2.0 mg g^{-1} with the increase of Ca^{2+} concentration in the culture solution (Figure 4(d)). In Figures 4(e) and 4(f), the maximum Cs^+ contents in leaves and roots were below 19 mg g^{-1} and 43 mg g^{-1} at 1.0 mM Cs^+ treatment group, respectively. Simultaneously, the Cs^+ contents in leaves and roots were increased firstly and then decreased with the increase of Ca^{2+} concentration in the culture solution, and the maximum uptake of Cs^+ appeared at 0.5 mM Ca^{2+} treatment (Figures 4(e) and 4(f)). Moreover, the content of Ca^{2+} in leaves gradually decreased from ~22 mg g^{-1} to ~7 mg g^{-1} as the increase of Ca^{2+} concentration from 0.5 to 10 mM (Figure 4(e)). High concentration of Ca^{2+} could lead to excessive salt content in the culture medium and further inhibit the growth and development of roots. Therefore, the uptake of Cs^+ in lettuce was inhibited under the Ca^{2+} stress to some extents. It could be seen from Table S2 that the dry weight biomass slightly decreased to 1.193 g for leaves and 0.130 g for roots in the group at 10.0 mM Ca^{2+}. Due to the competition among coexisting ions in the culture solution, Ca^{2+} indeed

Table 2: Correlation analysis between Cs treatment concentrations and growth parameters and physiological parameters.

Index	Cs concentration	FW_{leaf}	MDA	FW_{root}	GSH	Root vitality	Chl a	Chl b
Cs concentration	1							
Leaf-FW	-0.912**	1						
MDA	0.972**	-0.937**	1					
Root-FW	-0.895**	0.980**	-0.926**	1				
GSH	0.650	-0.734	0.779*	-0.673	1			
Root vitality	0.882**	-0.946**	0.909**	-0.947**	0.602	1		
Chl a	-0.567	0.443	-0.533	0.571	-0.102	-0.454	1	
Chl b	-0.406	0.368	-0.392	0.529	0.006	-0.388	0.952**	1

**At level 0.01 (double-tail), the correlation was significant. *At level 0.05 (double-tail), the correlation was significant.

inhibited the uptake of Mg^{2+} significantly (Figures 4(c)–4(f)). As is well known, porphyrin ring is the main molecular skeleton of chlorophyll, where Mg^{2+} is present in the structure center of porphyrin molecule [30]. The deficiency of Mg^{2+} could significantly inhibit the transformation from coproporphyrinogen III or protoporphyrin IX to chlorophyll [31]. Meanwhile, Mg^{2+} is a synthetic component of many enzymes in plants and an activator of some enzymes [30]. The results clearly showed that high Cs^+ concentrations could cause chlorosis of lettuce leaves (Figure 1(a)) and inhibit the uptake of Mg^{2+}, which indicated that Cs^+ affected the synthesis of chlorophyll and the occurrence of photosynthesis.

No significant change was observed about Cs^+ contents in roots and leaves after lettuce exposed to Na^+ solution (Figure S1C-F). Compared with the K^+- and Ca^{2+}-treated groups, the lowest uptake amount of Cs^+ was observed after Na^+ treated, indicating a stronger inhibition of Na^+ on uptake of Cs^+ by lettuce. The inhibition effect of Na^+ on lettuce growth mainly suppressed the uptake of essential elements and water through the increasing osmotic pressure of root cells [32–36].

As shown in Figure S2A-D, Cs^+ content in roots was much higher than that in leaves, but the accumulation of Cs^+ in leaves was much higher than that in roots, which is due to the fact that the biomass of leaves was much larger than that of roots. Because the leaves of lettuce are the main edible parts, it is deduced that Cs^+ contamination in leaves may bring threats to the safety of food chain and human health.

3.4. Response of Plant Physiological Indicators to Cs^+ Stress. Glutathione (GSH), malondialdehyde (MDA), root vitality, and chlorophyll were determined after a 21-day treatment with Cs^+. The detection methods are shown in the Supplementary Materials (available here). As shown in Figure 5(a), the GSH content significantly increased to ~1200 $\mu g\,g^{-1}{}_{FW}$ from ~800 $\mu g\,g^{-1}{}_{FW}$ when Cs^+ concentration was higher than 0.5 mM. Reactive oxygen was produced due to the oxidative stress when lettuce was subjected to high concentration of Cs^+ stress, which inhibited the normal growth of the plant. To this end, the antioxidant GSH was produced in plant cells to remove the effects of reactive oxygen. And the content of GSH was increased with the increasing of Cs^+ treatment concentration.

In the case of plant tissue aging or under adverse conditions, the membrane lipid peroxidation often occurred, where MDA was one of the final decomposition products of membrane lipid peroxidation [37]. As shown in Figure 5(b), MDA content kept a constant level which was less than 0.003 $\mu mol\,g^{-1}$ when Cs^+ concentration was less than 0.5 mM and then significantly increased to ~0.005 $\mu mol\,g^{-1}$ at 10 mM Cs^+. The results clearly confirmed that the damage of lettuce could be negligible at low dose of Cs^+ due to the low chemical toxicity of stable Cs. However, high Cs^+ concentration could produce certain damage to lettuce tissue. Figure 5(c) shows that the root reactive oxygen species increased significantly in the presence of 5.0 and 10.0 mM Cs^+, and it severely inhibited the growth of plant roots as shown in Figure 1(a). As shown in Table 2, a significant positive correlation was observed among Cs^+ concentration, MDA, and root vitality. Root is the main tissue in which plants absorb water and mineral elements. Root vitality is one of the important parameters to estimate the uptake of nutrients and other substances. Moreover, root vitality could reflect the accumulation of peroxides and free radicals in plants during adversity, which accelerated the oxidation of plant root aging. High Cs^+ level treatment inhibited the growth and the development of lettuce roots, which reduced biomass and influenced the surface area of root part and then further affected the transfer of Cs^+ at the water-root interface.

As shown in Figure 5(d), the contents of chlorophyll a and b increased firstly and then decreased with increasing Cs^+ concentration, and the greatest value occurred at 0.5 mM, which was consistent with the changes in lettuce biomass. Plant physiology began to show obvious symptoms after treated with high Cs^+ concentration. In fact, chlorophyll a could transform light energy into chemical energy by photochemical action in photosynthesis, and chlorophyll b mainly plays a role of absorbing and transferring light energy. The total content of chlorophyll indicates the high sensitivity of lettuce to Cs stress, which affect the photosynthetic efficiency and photosynthetic yield. As shown in Figure 1(a), the leaf color and species of lettuce were changed a lot under different Cs^+ culture solutions, which was

Table 3: Effects of exposure to the different concentrations of Na^+, K^+, and Ca^{2+} on biomass while the lettuces were cultivated in cesium concentration of 1.0 mM.

Treatment	Concentration (mM)	Leaf fresh weight (g)	Root fresh weight (g)	Leaf dry weight (g)	Root dry weight (g)
Na^+	0	17.490 ± 0.879^{ab}	2.110 ± 0.243^{ab}	0.854 ± 0.047^{ab}	0.101 ± 0.009^{bc}
	0.005	21.290 ± 4.312^{a}	2.790 ± 1.012^{a}	1.083 ± 0.227^{a}	0.132 ± 0.027^{ab}
	0.05	8.657 ± 0.761^{c}	0.837 ± 0.163^{c}	0.685 ± 0.048^{b}	0.064 ± 0.007^{c}
	0.5	20.190 ± 4.196^{ab}	2.283 ± 0.660^{ab}	1.147 ± 0.290^{a}	0.157 ± 0.034^{a}
	1.0	18.860 ± 1.380^{ab}	1.933 ± 0.029^{ab}	1.076 ± 0.141^{a}	0.144 ± 0.023^{a}
	5.0	17.390 ± 1.254^{ab}	1.803 ± 0.218^{ab}	0.962 ± 0.078^{ab}	0.133 ± 0.014^{ab}
	10.0	16.090 ± 0.869^{b}	1.317 ± 0.206^{b}	0.875 ± 0.031^{ab}	0.120 ± 0.005^{ab}
	Average	17.14	1.868	0.955	0.122
K^+	0	7.120 ± 1.818^{bc}	0.573 ± 0.204^{bc}	0.670 ± 0.187^{cd}	0.073 ± 0.018^{cd}
	0.005	7.233 ± 1.026^{bc}	0.547 ± 0.083^{bc}	0.726 ± 0.106^{bcd}	0.080 ± 0.010^{bcd}
	0.05	6.920 ± 0.815^{c}	0.450 ± 0.020^{bc}	0.750 ± 0.110^{bcd}	0.088 ± 0.006^{abc}
	0.5	5.210 ± 0.061^{c}	0.330 ± 0.044^{c}	0.534 ± 0.035^{d}	0.056 ± 0.004^{d}
	1.0	9.833 ± 0.822^{b}	0.657 ± 0.081^{b}	0.850 ± 0.069^{abc}	0.087 ± 0.007^{abc}
	5.0	13.317 ± 2.531^{a}	0.980 ± 0.286^{a}	0.944 ± 0.199^{ab}	0.098 ± 0.020^{ab}
	10.0	15.480 ± 1.400^{a}	1.050 ± 0.151^{a}	1.013 ± 0.081^{a}	0.105 ± 0.010^{a}
	Average	9.302	0.655	0.784	0.084
Ca^{2+}	0	9.057 ± 0.663^{c}	1.060 ± 0.098^{ns}	0.684 ± 0.047^{d}	0.065 ± 0.007^{b}
	0.005	9.230 ± 1.297^{c}	1.077 ± 0.395^{ns}	0.731 ± 0.083^{cd}	0.069 ± 0.017^{b}
	0.05	10.053 ± 1.944^{bc}	1.377 ± 0.177^{ns}	0.882 ± 0.121^{bcd}	0.084 ± 0.009^{ab}
	0.5	12.480 ± 1.231^{b}	1.213 ± 0.127^{ns}	0.956 ± 0.066^{ab}	0.090 ± 0.004^{ab}
	1.0	12.330 ± 1.929^{b}	1.040 ± 0.160^{ns}	0.916 ± 0.147^{abc}	0.087 ± 0.018^{ab}
	5.0	17.830 ± 0.807^{a}	1.257 ± 0.260^{ns}	1.110 ± 0.103^{a}	0.108 ± 0.017^{a}
	10.0	16.837 ± 1.990^{a}	1.033 ± 0.199^{ns}	0.994 ± 0.118^{ab}	0.100 ± 0.013^{a}
	Average	12.545	1.151	0.896	0.086

Values are mean ± SD ($n = 3$ individual plants). The same letters and ns indicate no significant difference at the 5% level by Tukey's multiple range test.

possibly related to the lettuce photosynthesis. Kim et al. [38] found that the content of photosynthetic pigments increased or decreased when different varieties of red peppers were irradiated by radioactive elements and believed that this phenomenon was not directly related to the increase in early growth, but related to the varieties of pepper. Therefore, it is speculated that the increase of chlorophyll content is related to the variety of lettuce itself and stimulation of low concentration of Cs on lettuce growth. Previous researchers have found that photosynthesis was inhibited in *A. thaliana* under a wide Cs^+ concentration range from 0.5 to 10 mM [16, 17, 21]. Kamel et al. [39] observed a decrease of chlorophyll content in *Epipremnum aureum* by the addition of RCs to nutrient solution. The concentration of chlorophyll a and b was also significantly decreased in *Phytolacca americana* and *Amaranthus cruentus* with increasing ^{134}Cs concentration in soil [40]. Stable Cs could lead to abnormal expression of genes related to photosynthesis pathway and then block the electron transport process from plastoquinone-QA to plastoquinone-QB, which resulted in abnormal photosynthesis and growth of *B. juncea* [41].

3.5. Effect of Cs^+ Application on Lettuce Biomass. As shown in Table 1 and Table S1, the fresh weight of leaves and roots decreased with the increasing Cs^+ concentration within 6 days for all groups. However, the biomass increased and then decreased when sampling time was longer than 9 days, which was similar to chlorophyll content. The largest biomass was either at 0.05 or 0.5 mM Cs^+ level, and the smaller biomass was either at 5.0 or 10.0 mM Cs^+ level. As shown in Table 2, a significant negative correlation was found between Cs^+ concentration and fresh weight of leaves and roots. It is obvious that high Cs^+ concentration can inhibit significantly the growth of lettuce. In similarity, low concentrations of RCs stimulated the growth of *Lepidium sativum* cultivated in hydroponics with a radiation dose of 0.7 mGy [42]. Moreover, Kim et al. [38] confirmed that the low doses of RCs radiations (2-8 Gy) could enhance the seed germination and early seedling growth of *red pepper*, which was attributed to the activation of plant enzymes promoting plant metabolism as well as growth processes [43].

In Table 3 and Table S2, the average biomass of lettuce was the greatest under regulation of different Ca^{2+} concentrations, but the smallest one was related to K^+ regulation at 0.1 mM Cs^+ concentration. In case of 1.0 mM Cs^+ level, the largest biomass was related to Na^+ treatment, and the lowest one corresponds to the K^+ treatment group. Although the biomass of roots and leaves could be regulated by K^+, Ca^{2+}, and Na^+ ions, however, K^+ and Ca^{2+} could produce more significant effect on lettuce biomass. Such phenomena mainly correspond to the variation tendency of Cs^+ content in root and leaf when lettuces were treated with K^+ and

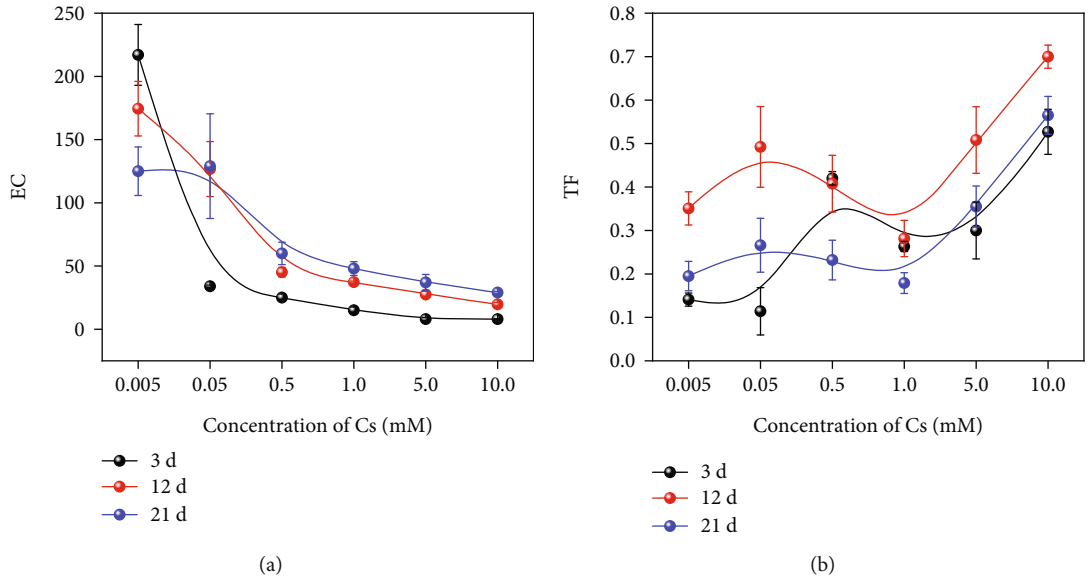

FIGURE 6: Comparison of enrichment coefficient (EC) and transfer factors (TF) at six different Cs^+ concentrations and sampling days ($n = 3$ individual plants).

Ca^{2+}. It suggests that K^+ and Ca^{2+} were main regulation substance on Cs^+ uptake by lettuce in the environment. According to previous views, more Cs^+ will be accumulated in lettuce tissues at the maximum biomass, so it is easily misleading and producing potentially harmful on human health [22, 23].

3.6. Analysis of TF and EC. As shown in Figure 6(a) and Table S3, EC was found to be in the range of 8-217. There was a notable phenomenon that EC increased with the decrease of Cs^+ concentration and the increase of growth time (except for the 5.0 μM Cs^+ treatment group). It indicates that RCs is more likely to enter the plant at low concentrations or trace level. However, there was much higher amount of Cs^+ in leaves when lettuce grew at an exposure of high Cs^+ level for long days (Table S3), which suggests that the edible portion of the plant accumulates more Cs^+, and the chances of entering the human body increase greatly. From Figure 6(b) and Table S3, TF was ranged from 0.114 to 0.828 under the influence of different Cs^+ concentration and sampling time. The transfer factors showed a trend of increasing with the increasing of Cs treatment concentration at first, then gradually decreasing little by little, but increasing at last. At high Cs^+ concentration, TF was much higher than that at low Cs^+ concentration, which indicates that more Cs^+ transferred from roots to edible partial leaves. The TF of stable Cs and RCs become influenced by the presence of other elements. It is therefore very important to consider type and nutritional status of the soil or culture solution.

4. Conclusion

This work presents the distribution and accumulation of Cs^+ in roots and leaves of the lettuce under different hydroponic conditions. The results clearly showed that lettuce growth and development were significantly inhibited at high Cs^+ level treatment, where lettuce biomass and root length significantly decreased. The content of Cs^+ in roots and leaves increased with the increase of Cs^+ concentration and growth time, and it was noticed that the content of Cs^+ in roots was much higher than that in leaves. The external K^+ concentration was negatively correlated with Cs^+ content in lettuce. K^+ was the main factor controlling the uptake of Cs^+ in lettuce. Under the Cs^+ stress, the contents of glutathione and malondialdehyde and the root viability of lettuce were significantly increasing as the Cs^+ concentration increased. The oxidative stress reaction in plant cells after Cs^+ stress caused damage to the antioxidant system in the roots and leaves of lettuce. However, the chlorophyll content decreased at high Cs^+ concentration treatment, which indicates that the stress of Cs^+ could inhibit photosynthesis reaction and results in an abnormal biological activity for lettuce. The lower concentration of Cs^+ treatment was, the higher EC in leaf was determined. Higher concentration of Cs^+ was treated, and more Cs^+ ions were transferred from roots to leaves. The solution-plant system used in this study ignores other factors, such as organic matter, clay minerals, and water content. Further consideration of the process in soil may provide a more comprehensive understanding of the factors affecting the migration of Cs^+ to plants. The findings in this work will be useful for understanding the contamination of vegetable plants in radioactive contaminated areas.

Data Availability

The data used to support the findings of this study are available from the corresponding author upon request.

Conflicts of Interest

The authors have no conflict of interest to disclose.

Acknowledgments

The authors acknowledge financial support from the National Natural Science Foundation of China (21876172), the "Youth Innovation Promotion Association CAS" (2020423), the Gansu Talent and Intelligence Center for Remediation of Closed and Old Deposits, and the Key Laboratory Project of Gansu Province (1309RTSA041).

Supplementary Materials

Figure S1: the effect of K^+ and Na^+ on the uptake of ions in lettuces. Figure S2: the comparison of mean value of the content, accumulation, EC, and TF of Cs under the influence of K^+, Ca^{2+}, Na^+, and two level of Cs. Table S1: effects of exposure to Cs^+ on biomass of lettuce. Table S2: effects of exposure to the different concentrations of Na^+, K^+, and Ca^{2+} on biomass while the lettuces were cultivated in cesium concentration of 0.1 mM. Table S3: cesium concentration, enrichment coefficient (EC), and transfer factor (TF) in lettuce leaves and roots after treatment with different cesium concentrations. *(Supplementary Materials)*

References

[1] HazDat, *Agency for Toxic Substances and Disease Registry (ATSDR)*, 2003, http://www.atsdr.cdc.gov/gsql/getsubstance.script?incas=007440-46-2.

[2] Agency for Toxic Substances and Disease Registry, *Public health statement for cesium. CAS#: 7440-46-2*, 2004, https://www.atsdr.cdc.gov/PHS/PHS.asp?id=575&tid=107.

[3] H. Nishita, E. M. Romney, and K. H. Larson, "Uptake of radioactive fission products by crop plants," *Journal of Agricultural and Food Chemistry*, vol. 9, no. 2, pp. 101–106, 1961.

[4] P. J. White and M. R. Broadley, "Tansley review no. 113," *New Phytologist*, vol. 147, no. 2, pp. 241–256, 2000.

[5] S. V. Avery, "Caesium accumulation by microorganisms: uptake mechanisms, cation competition, compartmentalization and toxicity," *Journal of Industrial Microbiology*, vol. 14, no. 2, pp. 76–84, 1995.

[6] P. J. White, "Cation channels in the plasma membrane of rye roots," *Journal of Experimental Botany*, vol. 48, no. Special, pp. 499–514, 1997.

[7] V. De Micco, C. Arena, D. Pignalosa, and M. Durante, "Effects of sparsely and densely ionizing radiation on plants," *Radiation Environmental Biophysics*, vol. 50, no. 1, pp. 1–19, 2011.

[8] L. L. Cook, R. S. Inouye, T. P. McGonigle, and G. J. White, "The distribution of stable cesium in soils and plants of the eastern Snake River Plain in southern Idaho," *Journal of Arid Environments*, vol. 69, no. 1, pp. 40–64, 2007.

[9] A. Burger and I. Lichtscheidl, "Stable and radioactive cesium: a review about distribution in the environment, uptake and translocation in plants, plant reactions and plants' potential for bioremediation," *Science of the Total Environment*, vol. 618, pp. 1459–1485, 2018.

[10] A. Burger and I. Lichtscheidl, "Strontium in the environment: review about reactions of plants towards stable and radioactive strontium isotopes," *Science of the Total Environment*, vol. 653, pp. 1458–1512, 2019.

[11] C. R. Hampton, H. C. Bowen, M. R. Broadley et al., "Cesium toxicity in Arabidopsis," *Plant Physiology*, vol. 136, no. 3, pp. 3824–3837, 2004.

[12] I. Sowa, M. Wójciak-Kosior, M. Strzemski et al., "Biofortification of soy (Glycine max(L.) Merr.) with strontium ions," *Journal of Agricultural and Food Chemistry*, vol. 62, no. 23, pp. 5248–5252, 2014.

[13] H. Tsukada, H. Hasegawa, S. Hisamatsu, and S. Yamasaki, "Transfer of ^{137}Cs and stable Cs from paddy soil to polished rice in Aomori, Japan," *Journal of Environmental Radioactivity*, vol. 59, no. 3, pp. 351–363, 2002.

[14] S. Yoshida, Y. Muramatsu, A. M. Dvornik, T. A. Zhuchenko, and I. Linkov, "Equilibrium of radiocesium with stable cesium within the biological cycle of contaminated forest ecosystems," *Journal Environmental Radioactivity*, vol. 75, no. 3, pp. 301–313, 2004.

[15] K. Zhang, J. Yuan, W. Kong, and Z. Yang, "Genotype variations in cadmium and lead accumulations of leafy lettuce (Lactuca sativa L.) and screening for pollution-safe cultivars for food safety," *Environmental Science: Processes Impacts*, vol. 15, no. 6, pp. 1245–1255, 2013.

[16] T. Sahr, G. Voigt, H. G. Paretzke, P. Schramel, and D. Ernst, "Caesium-affected gene expression in Arabidopsis thaliana," *New Phytologist*, vol. 165, no. 3, pp. 747–754, 2005.

[17] I. L. Jung, M. Ryu, S. K. Cho et al., "Cesium toxicity alters microRNA processing and AGO1 expressions in Arabidopsis thaliana," *PLoS One*, vol. 10, no. 5, article e0125514, 2015.

[18] D. J. Kang, Y.-J. Seo, T. Saito, H. Suzuki, and Y. Ishii, "Uptake and translocation of cesium-133 in napiergrass (Pennisetum purpureum Schum.) under hydroponic conditions," *Ecotoxicology and Environmental Safety*, vol. 82, pp. 122–126, 2012.

[19] E. Adams, V. Chaban, H. Khandelia, and R. Shin, "Selective chemical binding enhances cesium tolerance in plants through inhibition of cesium uptake," *Scientific Reports*, vol. 5, no. 1, pp. 1–10, 2015.

[20] J. Furukawa, "The terrestrial environmental dynamics of radioactive nuclides released by the Fukushima nuclear accident," *Yakugaku Zasshi Journal Pharmaceutical Society of Japan*, vol. 134, no. 2, pp. 143–148, 2014.

[21] P. Le Lay, M. P. Isaure, J. E. Sarry et al., "Metabolomic, proteomic and biophysical analyses of _Arabidopsis thaliana_ cells exposed to a caesium stress. Influence of potassium supply," *Biochimie*, vol. 88, no. 11, pp. 1533–1547, 2006.

[22] P. Fortunati, M. Brambilla, F. Speroni, and F. Carini, "Foliar uptake of ^{134}Cs and ^{85}Sr in strawberry as function by leaf age," *Journal of Environmental Radioactivity*, vol. 71, no. 2, pp. 187–199, 2004.

[23] C. Madoz-Escande, P. Henner, and T. Bonhomme, "Foliar contamination of Phaseolus vulgaris with aerosols of ^{137}Cs, ^{85}Sr, ^{133}Ba and ^{123}mTe: influence of plant development stage upon contamination and rain," *Journal of Environmental Radioactivity*, vol. 73, no. 1, pp. 49–71, 2004.

[24] Y. Zhu and E. Smolders, "Plant uptake of radiocaesium: a review of mechanisms, regulation and application," *Journal of Experimental Botany*, vol. 51, no. 351, pp. 1635–1645, 2000.

[25] L. V. Kochian and W. J. Lucas, "Potassium transport in corn roots," *Plant Physiology*, vol. 70, no. 6, pp. 1723–1731, 1982.

[26] L. Genies, D. Orjollet, L. Carasco et al., "Uptake and translocation of cesium by Arabidopsis thaliana in hydroponics conditions: links between kinetics and molecular mechanisms,"

Environmental and Experimental Botany, vol. 138, pp. 164–172, 2017.

[27] E. Smolders, L. Kiebooms, J. Buysse, and R. Merckx, "1^{37}Cs uptake in spring wheat (Triticum aestivum L.cv. Tonic) at varying K supply," *Plant and Soil*, vol. 181, no. 2, pp. 211–220, 1996.

[28] Y.-G. Zhu, G. Shaw, A. F. Nisbet, and B. T. Wilkins, "Effects of external potassium supply on compartmentation and flux characteristics of radiocaesium in intact spring wheat roots," *Annals of Botany*, vol. 85, no. 2, pp. 293–298, 2000.

[29] M.-P. Isaure, A. Fraysse, G. Devès et al., "Micro-chemical imaging of cesium distribution in Arabidopsis thaliana plant and its interaction with potassium and essential trace elements," *Biochimie*, vol. 88, no. 11, pp. 1583–1590, 2006.

[30] I. A. N. Fleming, "Absolute configuration and the structure of chlorophyll," *Nature*, vol. 216, no. 5111, pp. 151-152, 1967.

[31] M. Zhou, X. Gong, W. Ying et al., "Cerium relieves the inhibition of chlorophyll biosynthesis of maize caused by magnesium deficiency," *Biological Trace Element Research*, vol. 143, no. 1, pp. 468–477, 2011.

[32] T. J. Flowers and A. R. Yeo, "Breeding for salinity resistance in crop plants: where next?," *Functional Plant Biology*, vol. 22, no. 6, pp. 875–884, 1995.

[33] B. Gupta and B. Huang, "Mechanism of salinity tolerance in plants: physiological, biochemical, and molecular characterization," *International Journal Genomics*, vol. 2014, pp. 1–18, 2014.

[34] T. Horie, T. Kaneko, G. Sugimoto et al., "Mechanisms of water transport mediated by PIP aquaporins and their regulation via phosphorylation events under salinity stress in barley roots," *Plant and Cell Physiology*, vol. 52, no. 4, pp. 663–675, 2011.

[35] M. A. Khan, I. A. Ungar, and A. M. Showalter, "Effects of salinity on growth, water relations and ion accumulation of the subtropical perennial halophyte, Atriplex griffithii var. stocksii," *Annals Botany*, vol. 85, no. 2, pp. 225–232, 2000.

[36] N. Tuteja, "Mechanisms of high salinity tolerance in plants," *Methods in Enzymology*, vol. 428, pp. 419–438, 2007.

[37] Y. Li, S. Zhang, W. Jiang, and D. Liu, "Cadmium accumulation, activities of antioxidant enzymes, and malondialdehyde (MDA) content in Pistia stratiotes L," *Environmental Science and Pollution Research*, vol. 20, no. 2, pp. 1117–1123, 2013.

[38] J.-H. Kim, M.-H. Baek, B. Y. Chung, S. G. Wi, and J.-S. Kim, "Alterations in the photosynthetic pigments and antioxidant machineries of red pepper (Capsicum annuum L.) seedlings from gamma-irradiated seeds," *Journal of Plant Biology*, vol. 47, no. 4, pp. 314–321, 2004.

[39] H. A. Kamel, S. B. Eskander, and M. A. S. Aly, "Physiological response of Epipremnum aureum for cobalt-60 and cesium-137 translocation and rhizofiltration,," *International Journal of Phytoremediation*, vol. 9, no. 5, pp. 403–417, 2007.

[40] S. Tang, S. Liao, J. Guo, Z. Song, R. Wang, and X. Zhou, "Growth and cesium uptake responses of Phytolacca americana Linn. and Amaranthus cruentus L. grown on cesium contaminated soil to elevated CO_2 or inoculation with a plant growth promoting rhizobacterium Burkholderia sp. D54, or in combination," *Journal of Hazardous Materials*, vol. 198, pp. 188–197, 2011.

[41] Y. Zhang and G. Liu, "Effects of cesium accumulation on chlorophyll content and fluorescence of Brassica juncea L," *Journal of Environmental Radioactivity*, vol. 195, pp. 26–32, 2018.

[42] D. Marčiulionienė, B. Luksiene, D. Montvydienė, and D. Kiponas, *Estimation of ^{137}Cs and ^{90}Sr Ionizing Radiation Impact on the Plant Vegetative and Generative Organs*, 2008.

[43] D. Marčiulionienė, "Radiokhemoekologicheskaja situacijav oz. Drukshjaj-vadaeme-okhladitele Ignalinskoj AES [Radiochemoecological situation in Lake Drukšiaicooling water reservoir of the Ignalina NPP, in Russian]," *Drug Metabolism and Disposition*, pp. 1–125, 1992.

Hindawi
Adsorption Science & Technology
Volume 2022, Article ID 3838766, 9 pages
https://doi.org/10.1155/2022/3838766

Research Article

Study on the Behaviors and Mechanism of Ni(II) Adsorption at the Hydroxyapatite-Water Interface: Effect of Particle Size

Xiaolan Zhao,[1,2] Wangsuo Wu,[1,2] Duoqiang Pan,[1,2] and Hanyu Wu [2,3]

[1]*Radiochemistry Laboratory, School of Nuclear Science and Technology, Lanzhou University, Lanzhou 730000, China*
[2]*Key Laboratory of Special Functional Materials and Structural Design, Ministry of Education, Lanzhou University, Lanzhou 730000, China*
[3]*Sino-French Institute of Nuclear Engineering and Technology, Sun Yat-Sen University, Zhuhai 519082, China*

Correspondence should be addressed to Hanyu Wu; wuhy76@mail.sysu.edu.cn

Received 28 July 2022; Revised 25 August 2022; Accepted 27 August 2022; Published 29 September 2022

Academic Editor: Huihui Du

Hydroxyapatite (HAP) was a highly efficient decontamination material for its strong adsorption capacity used in the immobilization of heavy metals, while the particle-size effect was insufficiently investigated during the sorption process. In the present study, the mechanisms of nickel (Ni(II)) adsorption on HAPs with two different particle sizes were investigated by combing batch experiments, desorption, and XRD analysis. The results showed that the adsorption capacity of 20 nm HAP (nano-HAP) was much higher than that of 12 μm HAP (micro-HAP). It was noticed that the results of the present study also clarified the distinct mechanisms in each adsorption process. As for micro-HAP, Ni^{2+} adsorbed through slow diffusion and replacement with Ca^{2+} and then incorporated in the lattice at pH between 6.5 and 9.0, which was confirmed by the results of kinetics, thermodynamics, and desorption. And a more compact crystalline structure and irreversible desorption behavior of micro-HAP after Ni(II) adsorption was confirmed by results of XRD and desorption isotherms, respectively. At pH > 9.0, lattice incorporation and precipitation controlled together. However, for nano-HAP, the sharp increase of Ni(II) adsorption and ionic strength dependent at pH 6.5 to 9.0 revealed that the dominant mechanisms were ionic exchange and inner-sphere complexation. XRD results showed that characteristic peaks of cassidyite appeared in Ni(II)-loading nano-HAP. At pH > 9.0, a precipitate of Ni(II) was the dominant mechanism. The experimental finds demonstrated that nanoscale HAP was a more fast, efficient, and desorbable adsorbent than micro-HAP for Ni(II) removal. These findings would be favorable for investigating the removal mechanisms of heavy metals on the HAP materials and designing the synthesis methods.

1. Introduction

Increasing human activities including mining and smelting production have resulted in growing heavy metal pollution (e.g., cadmium (Cd), lead (Pb), nickel (Ni), etc.) into the soil, water, and air [1–3]. Therefore, a fast and effective technology is urgent and important to deal with such heavy metal pollution in the environment [4–6]. Adsorption has been recognized as a clean and remarkably effective treatment technology as compared to conventional chemical precipitation, oxidation, and electrochemical [7, 8]. Common natural adsorbents studied in former research include clay minerals [9, 10], iron-manganese oxide [11, 12], and hydroxyapatite (HAP) [2, 4, 5, 8, 13–20]. Among these, HAP has gained extensive attention because of its low cost, widespread, and great adsorption capacities [21–26].

HAP is the most abundant phosphate mineral in the geological environment. Natural HAP minerals contain mainly calcium and phosphorus ($Ca_{10}(PO_4)_6(OH)_2$) [2, 27]. In addition, HAP is a kind of green and environment-friendly material, which possesses a robust hexagonal atomic framework based on two distinct calcium sites (Ca(I), Ca(II)), a tetrahedral-phosphate site, and an anion column along four edges of the unit cell [24]. Indeed, HAP turned out to be very efficient in immobilizing heavy metals in the environment, especially for Cd(II), and Pb(II) [4–6, 24, 27]. So far, dissolution-precipitation, cation exchange, and surface complexation have been proved to be the significant

mechanisms of heavy metals immobilization by HAP [2, 6]. In the dissolution-precipitation mechanism, HAP occurs a dissolution and supplies the media with phosphate ions which are capable of precipitating other surrounding metal cations (M), especially for Pb(II) [24]. This process can be portrayed by these two equations [2, 28]:

$$Ca_{10}(PO_4)_6(OH)_2 + 14\,H^+ \longrightarrow 10\,Ca^{2+} + 6\,H_2PO_4^- + 2\,H_2O, \quad (1)$$

$$10\,M^{2+} + 6\,H_2PO_4^- + 2\,H_2O \longrightarrow M_{10}(PO_4)_6(OH)_2 + 14\,H^+. \quad (2)$$

A different but equally common adsorption mechanism is cation exchange, in which metal cations could substitute the Ca sites into the HAP crystal lattice. The process was portrayed as followed [2, 28]:

$$Ca_{10}(PO_4)_6(OH)_2 + x\,M^{2+} \longrightarrow Ca_{10-x}M_x(PO_4)_6(OH)_2 + x\,Ca^{2+}. \quad (3)$$

When it comes to some metal ions such as Cd [4, 6, 14, 26, 27], Zn [14, 20], or Ni [18, 29], the cation exchange mechanism is rapid and more favorable to take place than a dissolution-precipitation process because the ionic radii of these metals are similar or smaller than Ca^{2+}(0.099 nm) [2, 6]. Moreover, according to the former studies, Ca deficiency promotes the adsorption of heavy metals on HAP [27]. Thereinto, a series of studies have confirmed Ca/P molar ratio of HAP acted as a key factor in the adsorption mechanisms [19, 20, 23, 27, 29]. Abound Ca-deficient sites and higher specific promote the heavy metals removal performance [27]. The effect of particle size on the removal of heavy metals pollution by HAP has also been studied by previous studies [30–32]. Wang et al. [31] used three particle-sized HAP to immobilize Pb in low-acidity soil and observed that HAP in the particle size of 20.08 nm has the best efficiency compared with other sizes . However, despite numerous investigations into the effect of HAP particle size, more attention has been focused on the nanoscale thus neglecting micron-scale HAP and the comparison.

Ni(II) is one of the most typical and widespread heavy metals in the environment [9, 10, 33]. A large number of previous studies investigated the adsorption mechanisms of Ni(II) on clay minerals and iron-manganese oxides [9, 10, 33]. The Ni(II) adsorption was strongly influenced by environmental factors such as pH, ionic strength, temperature, and organic matters. The primary mechanisms include ion exchange, outer-sphere complexes, inner-sphere complexes, and surface precipitates [9, 10, 33]. However, only a few studies have paid attention to the adsorption of Ni(II) on HAP [18, 34]. Mobasherpour et al., [34] revealed that the removal capacity of Pb^{2+}, Cd^{2+}, and Ni^{2+} increased in the following order: $Pb^{2+} > Cd^{2+} > Ni^{2+}$ because of the different acidity strength and ionic radii among these ions. However, the detailed mechanism of Ni(II) adsorption on HAP is not explored. Therefore, two different particle sizes of HAP were chosen to conduct the adsorption experiments with Ni(II). The aims of this study were (i) to characterize the different properties between these two types of HAP, (ii) to investigate the adsorption of Ni(II) on the HAP, and (iii) to elucidate the mechanisms of the adsorption of these two processes. The results of this study will provide important insights into the treatment of Ni(II) in the environment by using HAP.

2. Materials and Methods

2.1. Materials. All chemicals used in the experiments were purchased at analytic purity and used directly without any further purification. Hydroxyapatite (HAP) samples of 12 μm and 20 nm were purchased from Nanjing Emperor Nano Materials Co., Ltd., which were defined as micro-HAP and nano-HAP, respectively. Ni(II) stock solution (500.0 mg/L) was prepared by $Ni(NO_3)_2{\cdot}6H_2O$. All the stock solutions and suspensions were prepared with ultrapure water (18.2 MΩ·cm).

2.2. Adsorption and Desorption Experiments. The investigations of the Ni(II) behaviors and mechanisms on HAP of 12 μm and 20 nm were conducted through batch experiments in a series of 10 mL polyethylene centrifuge tubes. Certain volumes of HAP suspensions, stock solutions of $NaClO_4$ background electrolyte and Ni(II), and ultrapure water were pipetted into tubes achieving total volumes of 6.0 mL. In each adsorption system, the solid-to-liquid ratio (s/l) was maintained at 0.6 g/L, and the pH was adjusted to the desired value using a negligible volume of $HClO_4$ or NaOH solution. The pH values ranged from 4 to 11. The kinetic and thermodynamic experiments were maintained at pH 6.7 ± 0.1. Adsorption isotherms were conducted with initial concentrations from 0.8 to 66.7 mg/L. After shaking for 24 hours (kinetic experiments carried out until 72 hours) in a constant-temperature shaker (IS-RDD3, CRYSTAL) at 298 ± 1 K (thermodynamic experiments carried out at 318 ± 1 K as well), solid and liquid phases were separated by centrifugation at 12000 rpm for 30 min. The supernatant was used to determine the aqueous concentration of Ni(II) (C_e, mg/L) by spectrophotometry at a wavelength of 530 nm using dimethylglyoxime and disodium ethylenediaminetetraacetic acid. Blank samples are inserted in each batch of sample testing to control the standard deviations. The detection limit of spectrophotometry was 0.01 mg/L. The calculations of adsorption percentage (adsorption%) and adsorption quantity (Q, mg/g) of Ni(II) were illustrated in previous works [9, 35]. The solid phases were freeze-dried for further characterization. Desorption experiments were conducted following adsorption isotherms. After centrifugation, half of the supernatant was replaced by an equal volume of $NaClO_4$ background solution of pH 6.7 ± 0.1. Subsequently, the desorption systems were shaken for 168 hours at 298/318 ± 1 K and then analyzed as described in the adsorption experiments. All of the experimental data were the averages of duplicate/triplicate results, and the relative errors of data were less than 5%.

Kinetic and thermodynamic fit employed several validated models, such as pseudo-second-order, Weber-Morris, and Langmuir models, and described in detail in previous works [36, 37]. Thus, the equations and parameters would not repeat and mainly displayed key information.

2.3. Characterization. The pristine and Ni(II)-loading HAP samples were characterized in terms of morphology, specific surface area, and structure. The morphology images were obtained from a Hitachi S-4800 cold field emission high-resolution scanning electron microscope (FE-SEM). The Brunauer-Emmett-Teller (BET) method was used to determine the specific surface area of micro-HAP and nano-HAP. Brunauer-Emmett-Teller (BET) specific surface area (SSA) was measured using a Micrometrics ASAP 2020 Accelerated Surface Area. X-ray diffraction (XRD) patterns were obtained using a powder X-ray diffractometer (X' Pert PRO, Malvern PANalytical) equipped with a rotation anode using Cu-Kα radiation and operated at 40 kV and 30 mA. The scanning angle started from 5° to 65° with a step interval of 0.02° at a rate of 4.0°/min. The experimental curves were normalized to the absolute values without any smooth process and then identified the diffractions in contrast to the PDF standards of hydroxyapatite (PDF#09-0432), cassidyite (PDF#20-0228), gaspeite (PDF#12-0771), and theophrastite (PDF#14-0117) using Jade 5.0. HAP samples were measured using Nicolet Nexus 670 Fourier transform infrared spectrometer (FTIR) in the spectral range from 4000 to 400 cm^{-1}. The samples are diluted to 1% with KBr (spectrum pure). Then, the mixture was blended for 3 min and pressed to a pellet with a thickness of 10 mm at 120 Pa.

3. Results and Discussion

3.1. Characterization of HAP. HAP samples used in this study were divided into two different particle sizes including 12 μm and 20 nm, respectively. The SEM images are shown in Figure 1, and it can be noticed that micro-HAP represents an aggregative and agglomerative with a uniform spherical particle, and the surface was clean and smooth (Figure 1(a)), which exhibited a specific surface area of approximately 11.94 m^2/g. In comparison with micro-HAP, nano-HAP exhibited an amorphous feature of around 20 nm in size (Figure 1(b)). And it has been confirmed from the high specific surface area of nano-HAP about 63.53 m^2/g, which was about 5.3 times greater than that of micro-HAP. It suggested that nano-HAP possibly possessed a higher adsorption capacity to metal cations as an example of Ni(II).

The FTIR spectra of micro-HAP and nano-HAP were shown in Figure 2(a). In the range 400 to 4000 cm^{-1}, the absorption band at 3400 and 1600 cm^{-1} is mainly assigned to the OH stretching and bending vibrations of absorbed water, respectively. The hydroxyl group of hydroxyapatites exhibited characteristic spike absorption peaks at 3420 cm^{-1} and 633 cm^{-1}. The characteristic bands at 1100–1040 and 600–500 cm^{-1} were assigned to phosphate and carbonate bands at 1550, 1460, 1445, 1415, and 870 cm^{-1}. The results showed that the main functional groups of both HAP samples were consistent. And the nano-HAP contained less adsorbed water. As shown in the XRD patterns of HAP samples in Figure 2(b), compared to the PDF standard hydroxyapatite (PDF#09-0432), it can be noticed that pristine micro-HAP and nano-HAP exhibited obvious characteristic peaks at 25.88°, 31.77°, 32.20°, and 32.90° corresponding {002} and {211}, {112} and {300} crystallographic facets, respectively [5, 27].

3.2. Kinetic Estimation. The kinetics of Ni(II) adsorption on micro-HAP and nano-HAP as a function of contact time was shown in Figure 3. Knowledge of kinetics is important for the elucidation of adsorption mechanisms. From the results of kinetics, one can see that both of the adsorption with micro-HAP and nano-HAP were close to equilibrium at approximately 500 mins. This equilibrium time was longer than the adsorption time of Ni(II) on clay minerals (1-4 h) [9, 10, 30], indicating a different mechanism of adsorption between HAP and clay minerals. The adsorption capacity of nano-HAP was much higher than micro-HAP, which was consistent with the results of the specific surface area. It was worth noting that the adsorption of Ni(II) on nano-HAP has almost reached equilibrium after 500 minutes of reaction, while the micro-HAP reaction was still slowly increasing. This indicated that the mechanisms of adsorption were different between the two adsorbents.

In order to better understand the adsorption behavior and mechanism of Ni(II) on HAP, two different types of kinetic models (i.e., the pseudo-second-order model and the Weber-Morris model) were employed to simulate the interaction, and the relative parameters of each model were summarized in Table 1. One noticed that the correlation coefficient of the pseudo-second-order model was much closer to the unity of both two types of HAP (micro-HAP: $R^2 = 0.9960$; nano-HAP: $R^2 = 0.9999$), suggesting that the chemistry adsorption of Ni(II) on HAP possibly be retelimited by two different affected by two variables. The Weber-Morris model revealed that during that adsorbate uptake varies were controlled by more than one mechanism since the plot was multilinear in Figure 3 [36, 37]. The initial stage was attributed to the exterior boundary layer diffusion or instantaneous adsorption of the most readily available adsorbing sites on the HAP surface [37], while the second stage can be ascribed to the interior boundary layer diffusion [36]. It was worth noticing that the second stage was clearly different for the two-particle sizes of HA, indicating different adsorption mechanisms.

3.3. Effect of pH and Ni(II) Initial Concentration. Figure 4 showed the adsorption edge of Ni(II) on micro-HAP and nano-HAP as a function of pH at different initial Ni(II) concentrations. It can be seen that the adsorption percentage of Ni(II) on nano-HAP was much higher than on micro-HAP, which was scarcely influenced by the specific surface area. In view of this, the smaller particle size resulted in a larger specific surface area and more available adsorption sites, thus the amount of Ni adsorbed increased significantly. It was noticed that the adsorption edge of Ni(II) on micro-HAP and nano-HAP was significantly different in pH ranging from 7.5 to 9.0. For micro-HAP, the adsorption began at

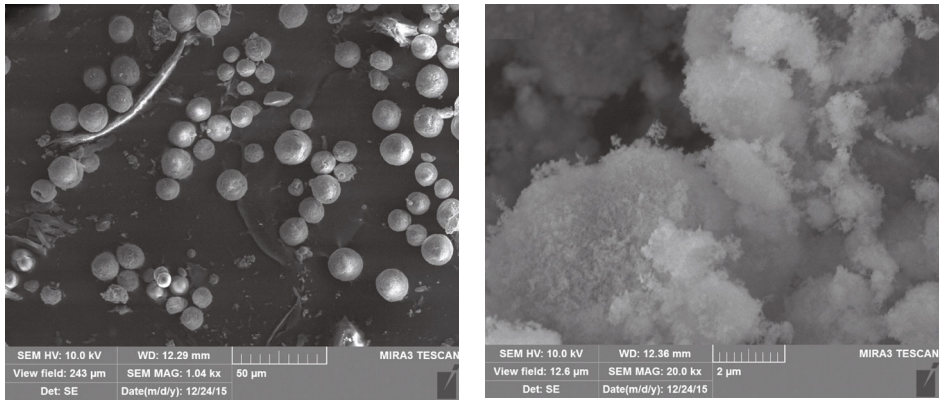

(a) (b)

Figure 1: SEM images of (a) micro-HAP (12 μm) and (b) nano-HAP (20 nm).

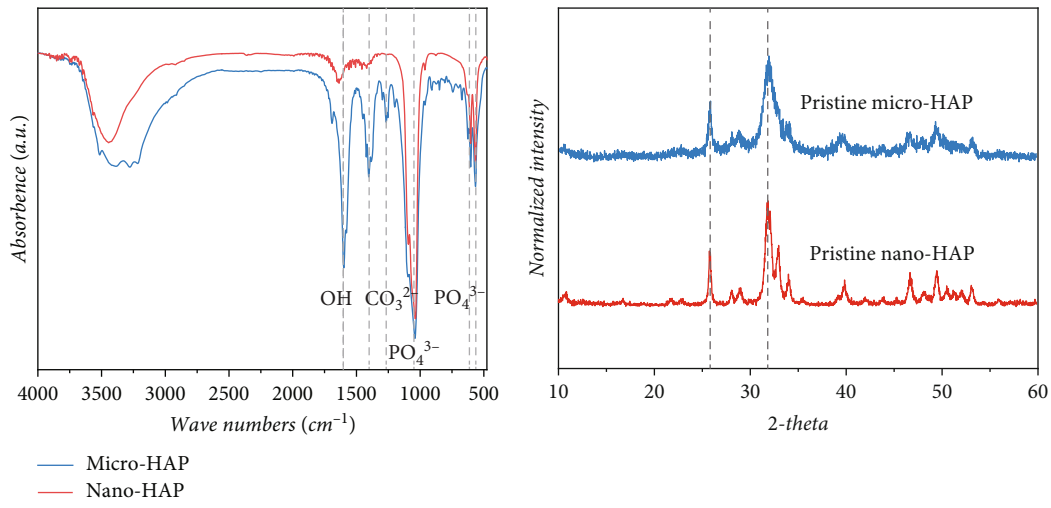

(a) (b)

Figure 2: FTIR spectrum (a) and XRD pattern (b) of micro-HAP and nano-HAP.

pH > 7.5 and with the increase of pH, the adsorption percentage exhibited steady growth. Moreover, the adsorption edge of Ni(II) on micro-HAP was independent of the initial concentration of Ni(II). Therefore, it can be assumed that at pH < 9.0, Ni(II) occurred slowly solid diffusion into the crystal lattice of micro-HAP and underwent lattice exchange with Ca(II) [2]. This pattern immobilized the Ni(II) stably. At pH > 9.0, it is controlled by both lattice exchange and precipitation mechanisms. Compared with the Ni(II) adsorption on micro-HAP, the adsorption on nano-HAP showed distinctly different mechanisms. The adsorption exhibited a start at pH > 5.0 and sparkly increased between 6.0 and 9.0. Over 90% of Ni(II) was adsorbed on nano-HAP above 9.0. The strong pH dependence suggested that the ionic exchange (IC) and inner-sphere complexes (ISCs) possibly controlled Ni(II) adsorption behavior [9]. At pH > 9.0, precipitation was the dominant mechanism. Unlike the adsorption of micro-HAP, the adsorption of Ni(II) on nano-HAP was obviously affected by the initial concentration of Ni(II). At higher initial Ni(II) concentration (50 mg/L), the adsorption shifted to higher pH with more than 1.0 pH units, which was similar to the Ni(II) uptake on illite [9].

3.4. Effect of Ionic Strength. Ionic strength is another important factor affecting the interaction, especially the adsorption behavior of heavy metals in the environment [35]. The effect of $NaClO_4$ concentration on Ni(II) adsorption by micro-HAP and nano-HAP at the pH adsorption edge was shown in Figure 5. As for micro-HAP from Figure 5(a), the adsorption of Ni(II) was completely independent of ionic strength, indicating the mechanism was without the influence of external ionic exchange. The results were mutually confirmed with the above results. Generally, the variation of ionic strength tended to affect the electrostatic interaction and outsphere surface complexes rather than lattice substitution or inner-sphere complexes [27]. In view of this, the negligible effect of ionic strength on the adsorption behavior of Ni(II) pointed the potential immobilization mechanisms of lattice replacement reaction with higher

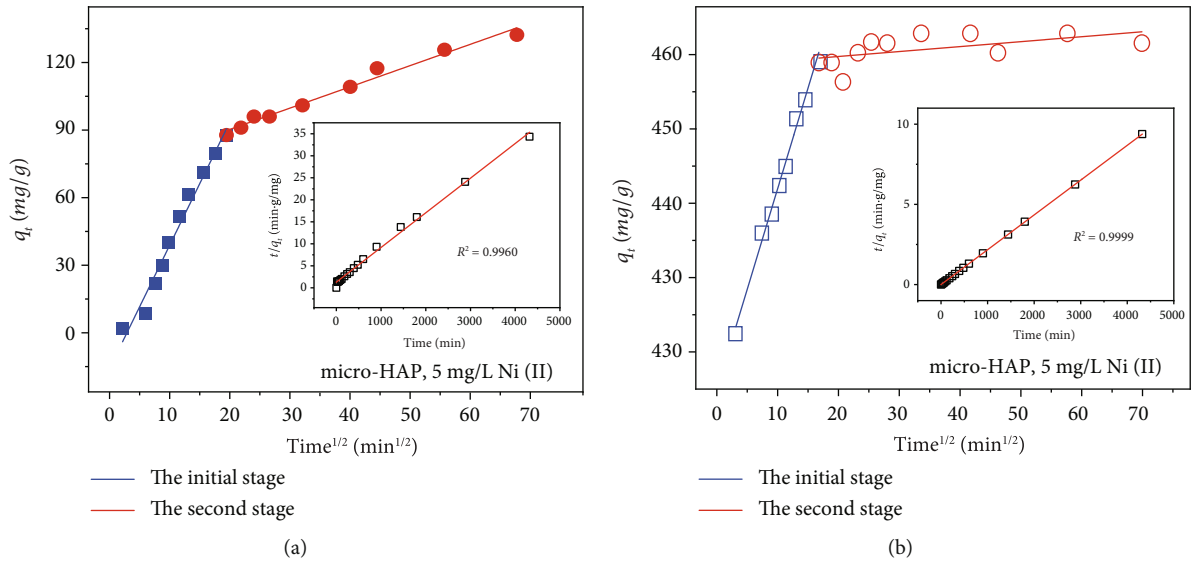

Figure 3: The kinetics of Ni(II) sorption on (a) micro-HAP and (b) nano-HAP (the solid lines: fitting plots of the Weber-Morris model). Bottom right figures: the fitting plots of the pseudo-second-order equation. ($T = 298 \pm 1$ K, $I = 0.1$ mol/L $NaClO_4$, $s/l = 0.6$ g/L, [Ni(II)] = 5.0 mg/L, and pH = 6.7 ± 0.1).

Table 1: The parameters of pseudo-first-order and Weber-Morris models of Ni(II) adsorption on micro-HAP and nano-HAP.

Models and parameters	Micro-HAP	Nano-HAP
Pseudo-first-order model		
q_e (mg/g)	127.06	460.83
k_1 (g/mg·min)	4.75×10^{-5}	1.68×10^{-3}
R^2	0.9960	0.9999
Weber-Morris model		
$k_{id,1}$ (mg/g·min$^{-1/2}$)	5.10	2.70
C_1	-1.63	422.91
R_1^2	0.9759	0.9919
$k_{id,2}$ (mg/g·min$^{-1/2}$)	0.88	0.07
C_2	70.79	457.49
R_2^2	0.9810	0.3116

thermodynamic stability or inner-sphere complexes (i.e. the covalent binding of Ni(II) with ≡Ca-OH and ≡P-OH functional groups). In a series of former studies, the adsorption of Hg(II) and Cd(II) by HAP were also found to be the independent phenomenon of ionic strength variation [21, 27]. However, for the nano-HAP, the adsorption of Ni(II) was controlled by the ionic strength, especially between 6.5 and 8.5. There was an obvious decline in Ni(II) adsorption with the increase of the ionic strength concentrations. There may be two reasons for these phenomena. One was that ionic exchange controlled the adsorption reaction [13, 27]. Rather, higher ionic strength might cause a greater possibility for the agglomeration of nanoparticles and inhibit the adsorption of Ni(II) [27]. More characterization and experiments were needed to support the specific conclusions.

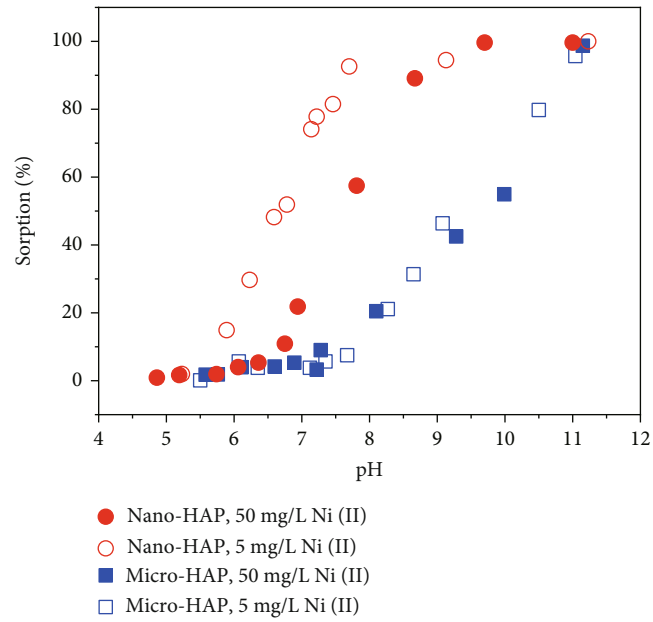

Figure 4: The influence of pH on Ni(II) sorption on micro-HAP and nano-HAP under varying nickel concentrations ($T = 298 \pm 1$ K, $I = 0.1$ mol/L $NaClO_4$, and $s/l = 0.6$ g/L).

3.5. Thermodynamics and Desorption. Ni(II) adsorption on micro-HAP and nano-HAP with respect to the temperature effect is demonstrated in Figure 6. The solid square and circle represented adsorption isotherms at 298 and 318 K, respectively. It was obvious that the isotherms of nano-HAP were higher than micro-HAP, which was supported by adsorption % at pH 6.7 (Figure 4). The enhanced Ni(II) adsorption induced by temperature increase indicated that Ni(II) adsorption was endothermic, in accordance with the results of Ni(II) adsorption on illite [9], smectite [38], and palygorskite [10]. The temperature effect raised the rate of

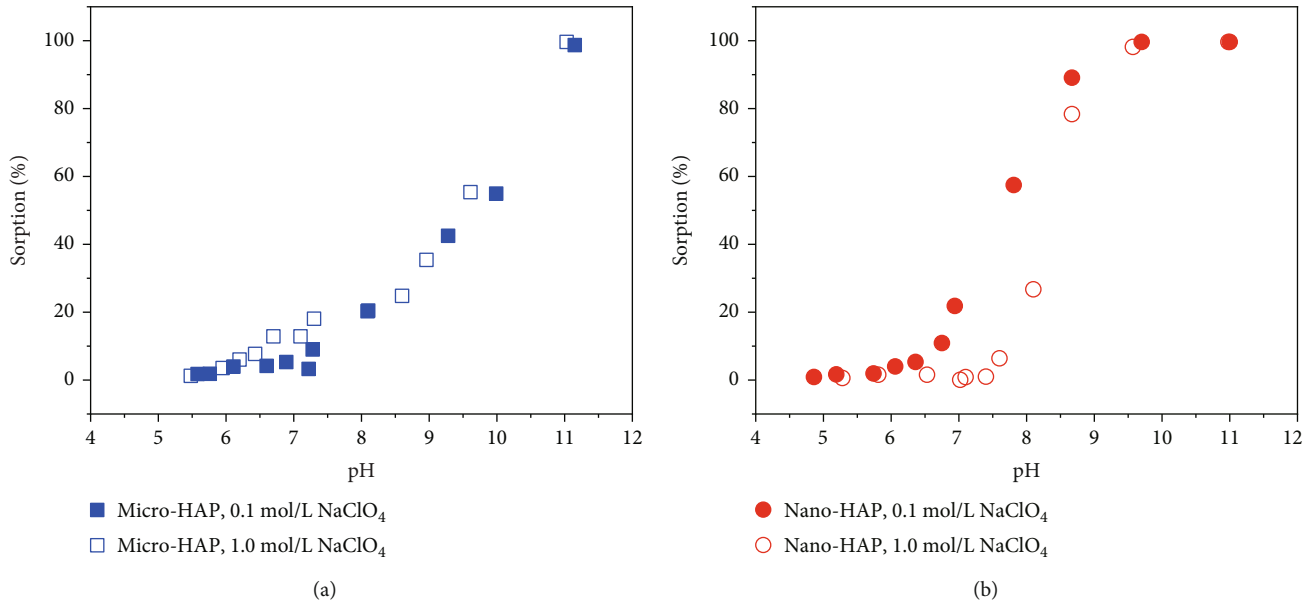

FIGURE 5: The influence of ionic strength on Ni(II) sorption on (a) micro-HAP and (b) nano-HAP ($T = 298 \pm 1\,K$, $s/l = 0.6$ g/L, and [Ni(II)] = 5.0 mg/L).

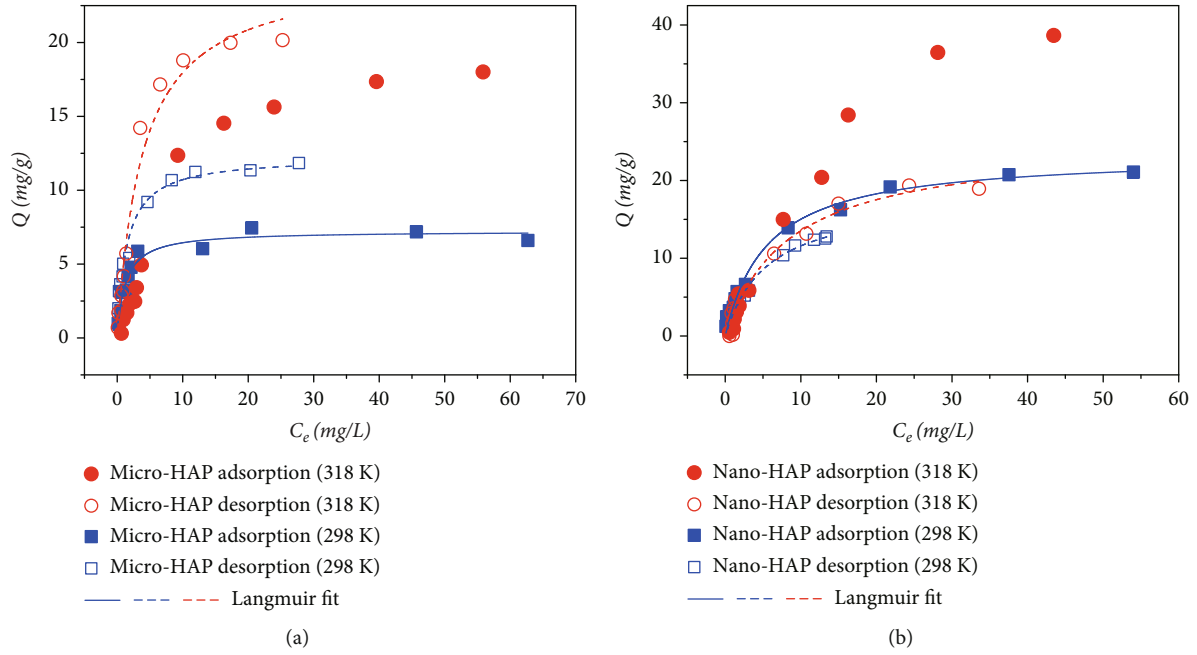

FIGURE 6: Adsorption/desorption isotherms at 298 K and 318 K of Ni(II) adsorption on (a) micro-HAP and (b) nano-HAP ($I = 0.1$ mol/L $NaClO_4$, $s/l = 0.6$ g/L, and pH = 6.7 ± 0.1).

approaching equilibrium [9, 36]. Moreover, the Langmuir fits evidenced that monolayer adsorption of Ni(II) occurred on both micro-HAP and nano-HAP even in the desorption process (Figure 6), except for the adsorption at 318 K (fitted by Freundlich model, data not shown). The parameters of Langmuir models are listed in Table 2, q_{max} supported the temperature effect on Ni(II) adsorption. Although temperature increase might cause changes in adsorption mechanism, such as accelerated adsorption at the surface of micro-HAP and nano-HAP, the monolayer adsorption equilibrium of Ni(II) reached afresh during the 168-hour desorption.

The results of desorption showed opposite phenomena in Ni(II) desorption from micro-HAP and nano-HAP (hollow square and circle). The higher desorption plots of micro-HAP represented that Ni(II) adsorption was irreversible and enlarged slowly at either 298 K or 318 K, which was verified by the kinetics of Ni(II) adsorbed on micro-HAP (Figure 6(a)). On the contrary, Ni(II) adsorption of nano-HAP was

Table 2: The Langmuir parameters of Ni(II) sorption/desorption and sorption-desorption hysteresis (HC%) on micro-HAP and nano-HAP.

Adsorption/desorption system	Langmuir model			HC%
	q_{max} (mg/g)	K_L (mL/g)	R^2	
Micro-HAP, 298 K				60.6
Adsorption	7.23	815.46	0.9480	
Desorption	12.25	695.90	0.9728	
Micro-HAP, 318 K				75.7
Adsorption	—	—	—	
Desorption	24.88	259.34	0.9736	
Nano-HAP, 298 K				-71.6
Adsorption	23.36	180.05	0.9883	
Desorption	17.94	182.66	0.9755	
Nano-HAP, 318 K				-2.0
Adsorption	—	—	—	
Desorption	24.90	118.94	0.9718	

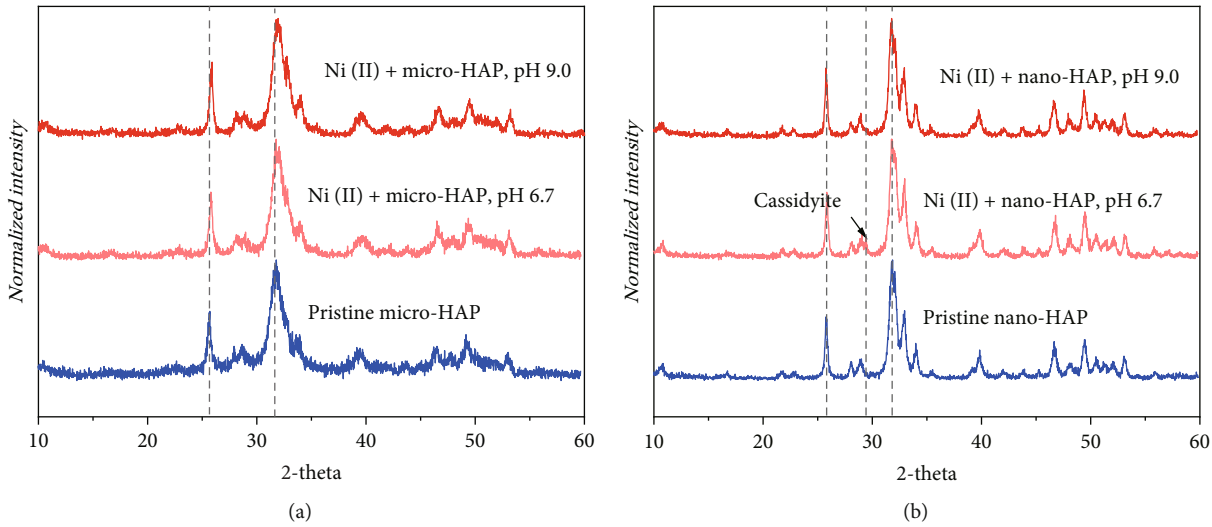

Figure 7: XRD patterns of pristine HAPs and Ni(II)-loading HAPs at pH 6.7 and 9.0. (a) micro-HAP and (b) nano-HAP.

reversible, which demonstrated that the quick ionic exchange of Ni(II) (Figure 6(b)) existed a weak bind on nano-HAP. The extents of irreversible or reversible adsorption could be quantified by the hysteresis coefficient (HC%) in Table 2, and the equation was described in previous works [36, 37].

3.6. XRD Results. XRD technique was the most intuitive and efficient method to investigate the crystal structure of materials. By comparing the crystal structures before and after adsorption experiments, it was possible to distinguish and identify the difference and mechanisms of Ni(II) on the micro-HAP and nano-HAP. The XRD patterns of pristine HAPs and adsorbed samples were shown in Figure 7. As shown in Figure 7(a), the diffraction peaks ascribed to {002} and {211} of Ni(II)-loading micro-HAP samples slightly shift towards high angles, including samples at pH 6.7 and 9.0. This phenomenon pointed to the appearance of a lattice incorporation mechanism [27]. In micro-HAP lattice, Ni^{2+} (0.072 nm) with a smaller ionic radius than Ca^{2+} (0.099 nm) substituted Ca^{2+}. The lattice replacement implied the enhancement of the entire micro-HAP crystalline structure and verified the effectiveness of Ni(II) substitution. Thus, it can be seen that the crystallization and orientation were enhanced by Ni(II) adsorption. These results also verified the previously speculated mechanism of *Ni(II)* adsorption on micro-HAP, in which Ni was slowly diffused into the HAP lattice and underwent lattice substitution with Ca^{2+}. This adsorption form and mechanism was stable and irreversible. Compared with the XRD patterns of Ni(II) adsorption on micro-HAP, there was no obvious shift in XRD patterns of Ni(II) adsorption on nano-HAP. However, there was a small peak at approximately 29° of the XRD pattern of nano-HAP adsorption sample at pH 6.7. Based on the comparison, this band might be

associated with the characteristic peak of the cassidyite ($Ca_2Ni(PO_4)_2{\cdot}2H_2O$), indicating that Ni(II) underwent ionic exchange with Ca^{2+}. There was neither a shift nor a new peak in XRD pattern of Ni(II) adsorption on nano-HAP at pH 9.0, indicating that precipitation of Ni(II) was the dominant mechanism at pH 9.0. It was consistent with the results of the ionic strength effect.

4. Conclusion

This work integrally investigated the different mechanisms of Ni(II) adsorption on HAP with two different particle sizes (12 μm and 20 nm). These two different HAPs exhibited specific surface areas and crystal structures, resulting in significant differences in the behaviors and mechanisms of Ni(II) adsorption. The results showed that adsorption percentage of Ni(II) on nano-HAP was much higher than that on micro-HAP, and it was inhibited by initial Ni(II) concentration and ionic strength only in the nano-HAP adsorption systems at pH 6.5-9.0. Nevertheless, Ni(II) adsorption on micro-HAP was independent of both Ni(II) concentration and ionic strength. These results implied the effect of particle size of HAPs, which was further investigated in adsorption/desorption isotherms at 298 K and 318 K. It can be summarized that the adsorption of Ni(II) on micro-HAP was mainly controlled by the slow diffusion and incorporation with Ca^{2+} from pH 6.5-9.0. At pH > 9.0, precipitation mechanisms are incorporated, but lattice incorporation still played a dominant role. The adsorption of Ni(II) on micro-HAP was spontaneous, endothermic, and irreversible. As for nano-HAP, a sharp increase in adsorption of Ni(II) from pH 6.5 to 9.0 mainly revealed that the adsorption was controlled by the ionic exchange and ISCs. When the pH increased to 9.0, precipitation was the dominant mechanism. These findings revealed that the nanoscale HAP removed heavy metals more effectively than microscale and provided a new perspective on condition control and material structure design for using HAP to remove the heavy metals contamination in the environment.

Data Availability

All data are available on request from the authors.

Conflicts of Interest

The authors declare that they have no conflicts of interest.

Acknowledgments

This work was supported by the National Natural Science Foundation of China [grant numbers 21906187], the China Postdoctoral Science Foundation (2021 M691372), the Fundamental Research Funds for the Central Universities [grant number lzujbky-2022-kb01], and the Key Laboratory Project of Gansu Province (1309RTSA041).

References

[1] X. L. Zhao, B. H. He, H. Y. Wu et al., "A comprehensive investigation of hazardous elements contamination in mining and smelting-impacted soils and sediments," *Ecotoxicology and Environmental Safety*, vol. 192, article 110320, 2020.

[2] M. Ibrahim, M. Labaki, J. M. Giraudon, and J. F. Lamonier, "Hydroxyapatite, a multifunctional material for air, water and soil pollution control: a review," *Journal of Hazardous Materials*, vol. 383, article 121139, 2020.

[3] Y. P. Yan, B. Wan, M. Mansor et al., "Co-sorption of metal ions and inorganic anions/organic ligands on environmental minerals: a review," *Science of the Total Environment*, vol. 803, article 149918, 2022.

[4] M. M. Wu, L. M. Mo, and E. Bi, "Effects of fulvic acid and montmorillonite colloids at different concentrations on Cd(II) sorption onto nano-hydroxyapatite," *Chemosphere*, vol. 248, article 125992, 2020.

[5] C. L. Zhou, X. Y. Wang, X. Song et al., "Insights into dynamic adsorption of lead by nano-hydroxyapatite prepared with two-stage ultrasound," *Chemosphere*, vol. 253, article 126661, 2020.

[6] C. L. Zhou, X. Song, Y. W. Wang, H. Wang, and S. F. Ge, "The sorption and short-term immobilization of lead and cadmium by nano- hydroxyapatite/biochar in aqueous solution and soil," *Chemosphere*, vol. 286, Part 3, article 131810, 2022.

[7] Y. H. Zhang, C. Q. Zhu, F. Q. Liu, Y. Yuan, H. D. Wu, and A. Li, "Effects of ionic strength on removal of toxic pollutants from aqueous media with multifarious adsorbents: a review," *Science of the Total Environment*, vol. 646, pp. 265–279, 2019.

[8] A. Nayak and B. Bhushan, "Hydroxyapatite as an advanced adsorbent for removal of heavy metal ions from water: focus on its applications and limitations," *Materials Today: Proceedings*, vol. 46, pp. 11029–11034, 2021.

[9] X. L. Zhao, S. R. Qiang, H. Y. Wu et al., "Exploring the sorption mechanism of Ni(II) on illite: batch sorption, modelling, EXAFS and extraction investigations," *Scientific Reports*, vol. 7, no. 1, p. 8495, 2017.

[10] X. X. Mo, M. G. Siebecker, W. X. Gou, and W. Li, "EXAFS investigation of Ni(II) sorption at the palygorskite-solution interface: new insights into surface-induced precipitation phenomena," *Geochimica et Cosmochimica Acta*, vol. 314, pp. 85–107, 2021.

[11] D. Ociński, I. Jacukowicz-Sobala, P. Mazur, J. Raczyk, and E. Kociołek-Balawejder, "Water treatment residuals containing iron and manganese oxides for arsenic removal from water - characterization of physicochemical properties and adsorption studies," *Chemical Engineering Journal*, vol. 294, pp. 210–221, 2016.

[12] C. M. McCann, C. L. Peacock, K. A. Hudson-Edwards, T. Shrimpton, N. D. Gray, and K. L. Johnson, "In situ arsenic oxidation and sorption by a Fe-Mn binary oxide waste in soil," *Journal of Hazardous Materials*, vol. 342, pp. 724–731, 2018.

[13] Y. J. Lee, E. J. Elzinga, and R. J. Reeder, "Sorption mechanisms of zinc on hydroxyapatite: systematic uptake studies and EXAFS spectroscopy analysis," *Environmental Science & Technology*, vol. 39, no. 11, pp. 4042–4048, 2005.

[14] A. Corami, S. Mignardi, and V. Ferrini, "Cadmium removal from single- and multi-metal (Cd+Pb+Zn+Cu) solutions by sorption on hydroxyapatite," *Journal of Colloid and Interface Science*, vol. 317, no. 2, pp. 402–408, 2008.

[15] F. Fernane, M. O. Mecherri, P. Sharrock, M. Hadioui, H. Lounici, and M. Fedoroff, "Sorption of cadmium and

copper ions on natural and synthetic hydroxylapatite particles," *Materials Characterization*, vol. 59, no. 5, pp. 554–559, 2008.

[16] D. X. Liao, W. Zheng, X. M. Li et al., "Removal of lead(II) from aqueous solutions using carbonate hydroxyapatite extracted from eggshell waste," *Journal of Hazardous Materials*, vol. 177, no. 1-3, pp. 126–130, 2010.

[17] Z. Z. Zhang, M. Y. Li, W. Chen, S. Z. Zhu, N. N. Liu, and L. Y. Zhu, "Immobilization of lead and cadmium from aqueous solution and contaminated sediment using nano-hydroxyapatite," *Environmental Pollution*, vol. 158, no. 2, pp. 514–519, 2010.

[18] I. Mobasherpour, E. Salahi, and M. Pazouki, "Removal of nickel (II) from aqueous solutions by using nano-crystalline calcium hydroxyapatite," *Journal of Saudi Chemical Society*, vol. 15, no. 2, pp. 105–112, 2011.

[19] W. Q. Tang, R. Y. Zeng, Y. L. Feng, X. M. Li, and W. Zhen, "Removal of Cr(VI) from aqueous solution by nano-carbonate hydroxylapatite of different Ca/P molar ratios," *Chemical Engineering Journal*, vol. 223, pp. 340–346, 2013.

[20] K. Viipsi, S. Sjöberg, K. Tõnsuaadu, and A. Shchukarev, "Hydroxy- and fluorapatite as sorbents in Cd(II)-Zn(II) multi-component solutions in the absence/presence of EDTA," *Journal of Hazardous Materials*, vol. 252-253, pp. 91–98, 2013.

[21] Y. Kim and Y. J. Lee, "Characterization of mercury sorption on hydroxylapatite: batch studies and microscopic evidence for adsorption," *Journal of Colloid and Interface Science*, vol. 430, pp. 193–199, 2014.

[22] A. A. Rouff, N. Ma, and A. B. Kustka, "Adsorption of arsenic with struvite and hydroxylapatite in phosphate-bearing solutions," *Chemosphere*, vol. 146, pp. 574–581, 2016.

[23] S. Campisi, C. Castellano, and A. Gervasini, "Tailoring the structural and morphological properties of hydroxyapatite materials to enhance the capture efficiency towards copper(II) and lead(II) ions," *New Journal of Chemistry*, vol. 42, no. 6, pp. 4520–4530, 2018.

[24] D. X. Guan, C. Ren, J. Wang, Y. Zhu, Z. Zhu, and W. Li, "Characterization of lead uptake by nano-sized hydroxyapatite: a molecular scale perspective," *ACS Earth and Space Chemistry*, vol. 2, no. 6, pp. 599–607, 2018.

[25] M. Ferri, S. Campisi, M. Scavini, C. Evangelisti, P. Carniti, and A. Gervasini, "In-depth study of the mechanism of heavy metal trapping on the surface of hydroxyapatite," *Applied Surface Science*, vol. 475, pp. 397–409, 2019.

[26] X. Han, Y. Zhang, L. Y. Li et al., "Nanosized hydroxyapatite supported on natural sepiolite: a novel adsorbent for cd(II) removal from simulated groundwater," *Materials Research Express*, vol. 6, no. 12, article 125518, 2019.

[27] Y. W. Zhang, H. Y. Tang, Q. Xiao, Y. Zhang, X. L. Zhao, and S. T. Yang, "New strumming sleight for old tunes: exploration on the sorption mechanisms of Cd(II) by hydroxyapatite synthesized with different molar Ca/P ratios," *Journal of Environmental Chemical Engineering*, vol. 10, no. 3, article 107919, 2022.

[28] C. Stötzel, F. A. Müller, F. Reinert, F. Niederdraenk, J. E. Barralet, and U. Gbureck, "Ion adsorption behaviour of hydroxyapatite with different crystallinities," *Colloids and Surfaces B: Biointerfaces*, vol. 74, no. 1, pp. 91–95, 2009.

[29] S. Rout, N. Khandelwal, A. K. Poswal, V. Pulhani, and A. V. Kumar, "Inducing non-stoichiometry in nano-hydroxyapatite for ultra-fast sequestration of uranyl ions in water: mechanism delineation using XAS," *Environmental Science Nano*, vol. 8, no. 5, pp. 1256–1268, 2021.

[30] W. Liu, G. M. Qian, L. L. Liu, B. Zhang, and X. Y. Fan, "A simple method to controlled synthesis of nano hydroxyapatite in different particle size," *Materials Letters*, vol. 217, pp. 177–180, 2018.

[31] Y. Wang, X. Q. Dong, J. Cui, Z. G. Wei, and X. H. Wang, "Effect of hydroxyapatite particle size on the formation of chloropyromorphite in anglesite–hydroxyapatite suspensions," *RSC Advances*, vol. 7, no. 20, pp. 11896–11903, 2017.

[32] Z. Zhao, G. Jiang, and R. Mao, "Effects of particle sizes of rock phosphate on immobilizing heavy metals in lead zinc mine soils," *Journal of Soil Science and Plant Nutrition*, vol. 14, 2014.

[33] B. Gueguen, J. V. Sorensen, S. V. Lalode, J. Pena, B. M. Toner, and O. Rouxel, "Variable Ni isotope fractionation between Fe-oxyhydroxides and implications for the use of Ni isotopes as geochemical tracers," *Chemical Geology*, vol. 481, pp. 38–52, 2018.

[34] I. Mobasherpour, E. Salahi, and M. Pazouki, "Comparative of the removal of Pb^{2+}, Cd^{2+} and Ni^{2+} by nano crystallite hydroxyapatite from aqueous solutions: adsorption isotherm study," *Arabian Journal of Chemistry*, vol. 5, no. 4, pp. 439–446, 2012.

[35] X. L. Zhao, Y. Wang, H. Y. Wu et al., "Insights into the effect of humic acid on Ni(II) sorption mechanism on illite: batch, XPS and EXAFS investigations," *Journal of the Molecular Liquids*, vol. 248, pp. 1030–1038, 2017.

[36] H. Y. Wu, P. Li, D. Q. Pan, Z. X. Yin, Q. H. Fan, and W. S. Wu, "Interactions between silicon oxide nanoparticles (SONPs) and U(VI) contaminations: effects of pH, temperature and natural organic matters," *PLoS One*, vol. 11, article 0149632, 2016.

[37] H. Y. Wu, Z. Xu, L. Zhu, X. Cheng, and M. L. Kang, "Adsorption of strontium at K-feldspar-water interface," *Applied Radiation and Isotopes*, vol. 181, article 110111, 2022.

[38] E. Tertre, G. Berger, S. Castet, M. Loubet, and E. Giffaut, "Experimental sorption of Ni^{2+}, Cs^{+} and Ln^{3+} onto a montmorillonite up to 150°C," *Geochimica et Cosmochimica Acta*, vol. 69, no. 21, pp. 4937–4948, 2005.

Hindawi
Adsorption Science & Technology
Volume 2022, Article ID 4421932, 28 pages
https://doi.org/10.1155/2022/4421932

Research Article

Structural Alteration, Hydration Stability, Heavy Metal Removal Efficiency, and Montmorillonite Porosity Fate by Coupling the Soil Solution pH and a Thermal Gradient

Chadha Mejri, Walid Oueslati, and Abdesslem Ben Haj Amara

Université de Carthage, Faculté des Sciences de Bizerte, LR19ES20: Ressources, Matériaux, Et Ecosystèmes (RME), 7021 Bizerte, Tunisia

Correspondence should be addressed to Walid Oueslati; walidoueslati@ymail.com

Received 9 June 2022; Revised 28 July 2022; Accepted 4 August 2022; Published 27 August 2022

Academic Editor: Linchuan Fang and Huihui Du

Clay minerals are considered as a promising material in the context of geological barrier for the confinement of radioactive and industrial waste. Understanding the usefulness of the smectite mineral, in this approach, remains insufficient. The deep investigation about structural response/changes, hydrate stability, cation exchange process, permeability, and heavy metal/radionuclide adsorption/removal efficiency under external constraints is needed. To explore the structural alteration, the hydration stability, and the evolution of montmorillonite porosity under a first order of external applied constraints coupling, a reference Na-rich montmorillonite specimen is used as a starting material, and three exchangeable heavy metal cations (Ba^{2+}, Cu^{2+}, and Co^{2+}) have been selected. The applied constraint coupling is realized at laboratory scale and assured by simultaneously varying of the soil solution pH and the thermal gradient. The evaluation of the mineral fraction response is established by correlation of quantitative XRD analysis results, thermal analysis, and porosity measurements. The quantitative XRD analysis allows rebuilding of the theoretical model describing the interlamellar space (IS) configurations/damages, structural heterogeneity degrees, and hydrous stability. Obtained results show a dominant interstratified hydration character, for all studied complexes, attributed to a new IS organization versus the applied constraint strength. Furthermore, all samples exhibit a heterogeneous hydration behavior traduced by the coexistence of different layers of type population within the crystallite. Additionally, the theoretical XRD profile decomposition allowed us to prove link between the domination of the segregated stacking layers mode against the constraint strength. Thermal analysis allowed us to develop theoretical models describing the decrease of the water molecule amounts as a function of the increase in temperature and soil solution pH. Moreover, a specific hydration footprint response and an interstratification mapping are assigned for each corresponding stress degrees. The evolution of montmorillonite porosity is determined by adsorption measurement, based on Brunauer, Emmett, and Teller (BET) and Barrett-Joyner-Halenda (BJH) pore size distribution analyses which confirms for all samples, the exfoliation process, and the mesopore diameter rise by increasing the constraint intensity.

1. Introduction

Montmorillonite is a 2 : 1 phyllosilicate type belonging to the smectite family. The montmorillonite structure consists of a stack of an octahedral (O) sheet (MO_4 $(OH)_2$) where (M) can be (Al) or (Mg) ions sandwiched between two tetrahedral (T) sheets (SiO_4). This structure is labeled by T-O-T, and the associated layer thickness along the c^* axis is about 10 Å [1–4]. The montmorillonite differs from the other dioctahedral smectites (beidellite and nontronite) by the existing isomorphous substitutions which occurs in the tetrahedral sheet (i.e., Al^{3+} substitutes for Si^{4+}) rather than in the octahedral sheet [5]. Indeed, the isomorphic substitutions appearing in the (T) or/and (O) sheets are defined by the localization of different type of cations in the various cavities. These substitutions result in a load deficit that is compensated on the outside of the layer, by compensating cations (CC) [5–7]. The intrinsic montmorillonite properties find a large environmental application domain as depolluant [8–11], ion exchanger [12–16], natural geological barrier for

industrial and radioactive waste confinement [17], clay-based nanocomposite for drug delivery [18–27], cosmetic compounds [28–31], medicinal application [32–35], antibacterial properties, and as a topical treatment for skin problems [36–39]. The structural and morphological properties are at the origin of this efficiency and the great exploitability in several fields of application. Indeed, the layer type with its infinite lateral extension (2D), the interlamellar space (IS) allowing the individual layer swelling (then the swelling of the crystallites) with the possibility of solvent insertion (due to the capacity of cation exchange CEC), and the macroporosity associated with the high specific surface (SA) (external and internal) are essential assets favoring the exploitation of such minerals [40, 41]. The montmorillonite layer expansion amount is affected, respectively, by the intrinsic layer charge location, the type/size/charge of exchangeable cation, the abundance/organization of water molecule in the IS, the type/size of organic/inorganic fraction present in the contact solution, the material history (fatigue/stress/strain), and the surrounding environmental/geochemical/mechanical conditions [42–46]. The CC and water molecules are positioned inside the IS, during cation exchange process, following a discreet arrangement allowing a progressive swelling process (hydration process) confirmed by the discretization of the basal spacing distance (d_{001}) fluctuations. The literature proposed basal spacing level defined by [5, 6, 47–49] is as follows: dehydrated 0 W (d_{001}~10 Å), one water layer 1 W (d_{001}~12.4 Å), two water layers 2 W (d_{001}~15.4 Å), three water layers 3 W (d_{001}~18.2 Å), and finally, four water layers 4 W (d_{001}~21 Å).

Montmorillonite is widely exploited (in adsorption science) for neutralizing the soil heavy metal dispersion/diffusion [50–52]. The adsorption factor usually depends on the solid/liquid ratio parameters in such kind of application. Usman et al. (2004) [53] demonstrate that low doses of clay (about 4% to 8%) eliminate up to 70% of heavy metals. In addition, the increase in the dose of the clay fraction is accompanied by the increase in the rate of adsorption [54, 55]. Also, the required dose and the remediation force may be affected by the variation in the mineral structural composition [56]. In the other hand, clay plays an essential role in the basic design of deep storage sites for radioactive and industrial waste confinement process [57–60]. The architecture of the sites is achieved by the association of several types of barriers (multibarrier concept). It consists of filler which is the waste in metal packages, incubated by a thick of concrete layer, covered by a clay films buried in well-determined host rock, at a depth of about 500 m below sea level. Several reasons, like the high radioactive element's adsorption capacity and the low permeability which slows down the radionuclides migration in the host rock, detailed in the work of [61–66] are in favor of the use of clay as a geological coating.

The clay adsorption capacity and the clay permeability properties are very sensitive to the variation of the soil solution pH [67–72], the surrounding temperature gradient [56, 67, 68, 72, 73], the kinetic effect during the cation exchange process [74], the surrounding atmospheric pressure variation [75, 76], the surrounding relative humidity (RH) constraint [77–81], the solid-liquid ratio effect during heavy metal removal [41], and the type and nature of the compensating cations [82–85]. Several works [67–72] show that there is a linearly proportional relationship between the pH level fluctuation and the performance of the heavy metal absorber (clay fraction). Es-Sahbany et al. (2019) [72] show that at room temperature, an optimal value of heavy metal adsorption rate was obtained; although at slightly lower or higher temperatures, this result may still be more ideal. Chantawon et al. (2003) [86] and Usman et al. (2004) [53] demonstrate good adsorption results at relatively high temperatures of around 36°C unlike some researchers [87] that observed a decrease in the adsorption rate at temperatures above 30°C. Other authors [88, 89] have proven that chemical adsorption reactions are essentially faster for temperatures that gradually increase with continuous increases in temperature.

On the other hand, the experimental approach in the study of the interaction (adsorption, cationic exchange and intercalation) of montmorillonite with heavy metals (and even organic molecules) by XRD analysis has been confirmed by theoretical calculations. Zhang et al. (2018) [90] studied the uranyl ion complexation on montmorillonite edges using a combined first-principle molecular dynamics and surface complexation modeling approach. Obtained results in the case of four selected representative complexing sites show that uranyl ions form hydrolyzed bidentate complexes on these sites. Liu et al. (2021) [91] used the molecular dynamic simulations to explain the sorption behaviors of heavy metal ions (zinc, cadmium, and lead) in the interlayer and nanopore of Wyoming montmorillonite. The calculated diffusion coefficients of the selected three cations in interlayer and nanopore indicated that their diffusion abilities were significantly impaired, implying that montmorillonite adsorbents have a strong ability to fix and retard heavy metal ions. Zhang et al. (2022) [92] investigates by the molecular dynamic simulations of the exchange behavior of radionuclides into montmorillonite. Authors demonstrate that multivalent cations prefer to stay in the mid-plane of interlayer region, and Cs+ and Rb+ cations are located closer to the basal plane via inner-sphere complexation. Furthermore, the orientations of interlayer uranyl ions are nearly perpendicular to basal surface. Density functional theory (DFT) is used to validate XRD data in the case of hydrated Na-hectorite exchanged with Cs-, Ca-, and Sr-cations [93]. Also, the first-principle DFT provides a prediction of the structure, stability, and dynamic properties of organoclays based on montmorillonite (Mt) intercalated with two types of organic cations—tetrabutylammonium (TBA) and tetrabutylphosphonium (TBP) [94]. The Cs adsorption on montmorillonite clay is investigated by ^{133}Cs chemical shift calculations, ^{133}Cs magic-angle-spinning nuclear magnetic resonance (MAS NMR) spectroscopy, X-ray diffraction under controlled relative humidity, and DFT calculations [95]. Obtained results shows that all Cs atoms were positioned around the center of hexagonal cavities in the upper or lower tetrahedral sheets. The calculated ^{133}Cs chemical shifts were highly sensitive to the tetrahedral Al (Al^{T})-Cs distance and d-spacing, rather than to the Cs coordination number.

Work on the linkage of constraints has not been adequately addressed in the literature. Indeed, Meftah et al. (2010) [84] showed that for a well-determined pH value and at a precise temperature clay can permanently change its structure. Thus, Marty et al. (2020) [85] explained that the coupling between the chemistry and hydration of clays shows a specific behavior for most water molecules considering RH and interlamellar space composition. The constraint coupling affecting, respectively, the clay hydration behavior, the absorber performance, and the ion exchanger efficiency is timidly approached during the main works carried out in the last decade focusing the use of clay in the context of multibarrier [41, 79, 96]. Several works [41, 79, 96] have concentrated on the effect of individual parameter and neglecting the coupling and the interaction between existing/surrounding parameters which generally affect the functionality of the material. Very few works are based on this very realist approach [12, 71]. To take full advantage of the huge possibilities of use of these minerals, it is necessary to simulate, at the laboratory scale, what happens during the real use. This approach is realized by respecting a scientific methodology based on five steps. The first is to decipher the nature and intensity of the constraints affecting the mineral (in question), and secondly, to determine the order of the possible couplings constraints and their nature (e.g., first coupling order: coupling of two constraints (e.g., T-%RH, T-pH, T-CEC, S/L ratio-T, …) and second coupling order: coupling of three constraints T-pH-S/L ratio and mechanical stress-T-%RH, …). The third step is to create and implement these constraint coupling types on a laboratory scale. The fourth step is to characterize the material's response. The last step is the evaluation/optimization based on the eventual results. The tremendous combination of constraints increases the challenges. For this purpose, we will focus on this work only at the first-order coupling between soil solution pH and thermal gradient designated by (T-pH).

Essentially, this work focuses the structural alteration, hydration stability, and evolution of montmorillonite porosity by (T-pH) in the case of Na-rich montmorillonite exchanged with heavy metals M^{2+}. This necessarily requires the realization/validation at the laboratory scale of an experimental first-order coupling which consists of the variations of geochemical and thermal stresses strength simultaneously. The structural evaluation is realized by a specific quantitative XRD analysis based on the modeling of the 001 reflections. Thermal analysis is used to develop the model describing interlamellar water molecule amount evolution versus constraint strength. The adsorption specificities and the porosity growth are investigated by BET and BJH pore size distribution analyses.

2. Materials and Methods

2.1. Baseline Material. A standard dioctahedral smectite SWy-2 extracted from the cretaceous formations of Wyoming (USA) and provided by the clay mineral repository is selected for the present study [1]. The structural formula per half-cell is given by [43]:

$$\left(Si^{4+}_{3.96}, Al^{3+}_{0.04}\right)\left(Al^{3+}_{1.53}, Fe^{3+}_{0.18}, Fe^{2+}_{0.045}, Mg^{2+}_{0.26}, Ti^{4+}_{0.01}\right) \cdot O_{10}(OH)_2\left(Ca^{2+}_{0.07}, K^{+}_{0.01}Na^{+}_{0.2}\right) \quad (1)$$

This bentonite exhibits a low octahedral charge and extremely limited tetrahedral Substitutions. The clay cation exchange capacity (CEC) is 101 meq/100 g [43].

2.2. Pretreatment. A pretreatment of the starting material consists of preparing Na-rich montmorillonite suspension (SWy-Na) is realized following a classic protocol detailed by [41] as shown in Figure 1.

2.3. Exchangeable Cations. Three heavy metal cations (Ba^{2+}, Cu^{2+}, and Co^{2+}) were the subject of the cation exchange process. The cation preference is explained by the wonderful abundance of the latter in industrial and radioactive waste and the specific characteristics of each one [97].

2.4. First-Order Coupling Constraints. First-order stress coupling is based on the association of geochemical (soil solution pH) and the thermal gradients (obtained by varying T °C) at the laboratory scale. To achieve this goal, an MCl_2 solution (where M is the metal cation Ba^{2+}, Cu^{2+} and Co^{2+}) at a well-determined pH is prepared at a low concentration (0.1 M), followed by the addition of Na-rich montmorillonite powder (SWy-Na). For each constraint pair created (fixed pH and fixed T), an adjustment of the overall volume (200 mL) is made by adding the metal chloride solution and the acid or base additive. Subsequently, and after several mechanical shaking cycle, a cation exchange process will take place at a well-determined temperature for a fixed specified period (24 h) (Figure 2). The soil solution pH variation and temperature values (T°C) are carried out on the same sample. All experimental parameters are summarized in Table 1.

2.5. Cation Exchange Process. A cation exchange process is carried out for each bivalent metal cations Ba^{2+}, Cu^{2+}, and Co^{2+} brought into contact with the starting sample. The experimental protocol established for each sample consists of applying a mechanical shake throughout 48 h, followed by centrifugation at 4000 rpm. This step is repeated five times to ensure process achievement. After recovery of the solid fraction, a series of washes with distilled water will take place to remove excess of salt from chloride ions. The obtained sample is labeled SWy-M with M that is the metal cation type (e.g., SWy-Ba, SWy-Cu, and SWy-Co). The experimental protocol is summarized in Figure 3.

To be able to analyze the complexes obtained using XRD, oriented sample was prepared by placing the obtained suspensions on a glass slide at air dry for 24 h.

2.6. X-Ray Diffraction (XRD). Structural characterization is carried out using XRD analysis by a Bruker D8 ADVANCE (Bruker AXS GmbH, Karlsruhe, Germany) with CuKα monochromatic radiation ($\lambda = 0.15406$ nm) at 40 kV and 20 mA. The usual scanning parameters were 0.01 ($2\theta^{\circ}$) as the step size and 6 s as the counting time per step over the

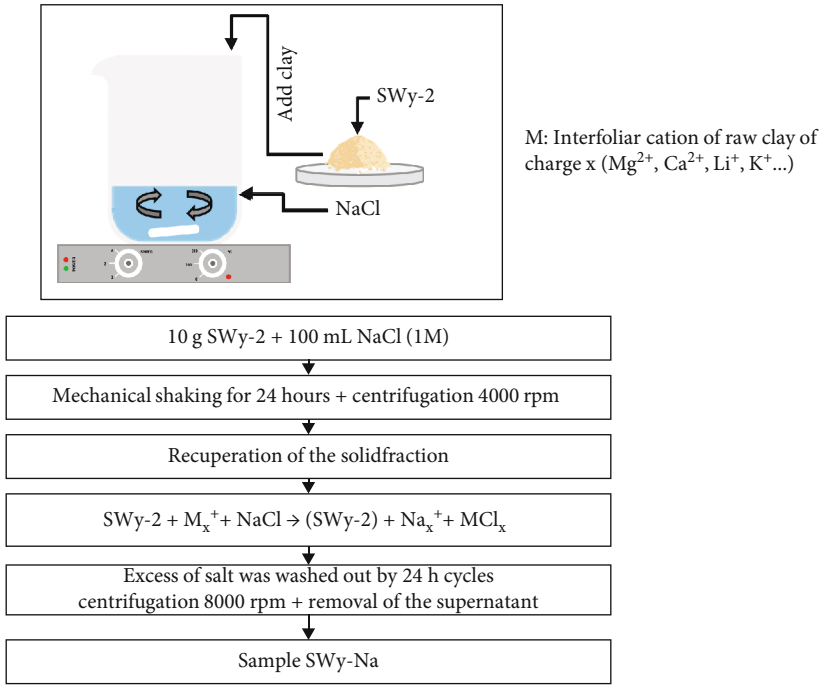

Figure 1: Experimental protocol for the purification of the starting material. Excess of salt was washed out by 24 h cycles: centrifugation 8000 rpm + removal of the supernatant.

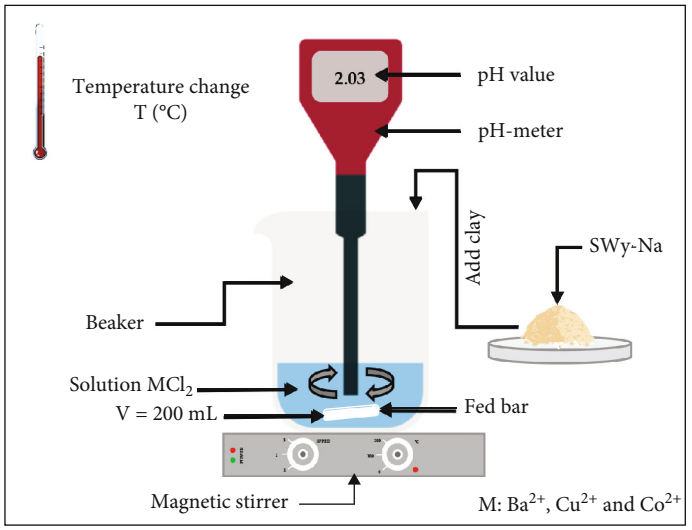

Figure 2: Experimental assembly of the 1st order coupling.

Table 1: Soil solution pH and temperatures of the coupling of the 1st order of the stresses.

Soil solution pH		Coupling of the 1st order		
		Temperature (°C)	Time (h)	V (mL)
Acid	3	50	24	200
	5	60		
Neutral	7	70		
Basic	9	80		
	11	90		

explored angular range. Indeed, the XRD profiles were recorded in the $2\theta^{\circ}$ range from 3.5 to 60 for all specimens. All records are made at room temperature under atmospheric pressure. XRD investigations were directed by the correlation between qualitative and quantitative analyses.

2.6.1. Semiquantitative XRD Analysis. The semiquantitative XRD investigation is carried out by determining, respectively, the observed homogeneity structure based on the 001 reflections shape, the experimental d_{001} basal spacing value, the calculated full width at the maximum half FWHM, the calculated crystallite size D, and the calculated rationality parameter ξ [98, 99]. This preliminary analysis

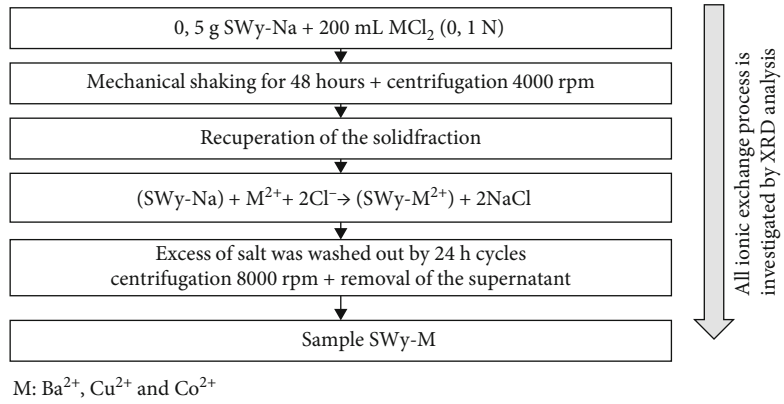

Figure 3: Experimental cation exchange protocol.

Table 2: The z atomic coordinates within the 2 : 1 layer framework along the c^* axis [42].

Atom type	O_1	O_2	O_3	O_4	O_5	O_6	OH_1	OH_2	Si_1	Si_2	Al
Number	2	1	2	2	1	2	1	1	2	2	2
Zn (Å)	0	0.20	2.25	4.31	6.26	6.59	1.98	4.28	0.59	6.04	3.43

remains insufficient to deeply identify interlamellar space (IS) contents, layer stacking mode at the crystallite size, the average layer number per stacking, the water molecule abundance and configuration, the saturation of the exchangeable intern and extern site, the hydration heterogeneities, the cause of the observed heterogeneity and the position, and the abundance of the exchangeable cation, and more.

2.6.2. XRD Profile Modeling: Theoretical Diffracted Intensity and Modeing Strategy. The modeling XRD approach is based on a matrix mathematical formalism developed by [42]. The expression of the intensity of the diffracted waves along the c^* axis is as follows:

$$I_{001}(2\theta) = L_p \mathrm{Spur}\left(\mathrm{Re}\,[\phi][W]\left\{[I] + 2\sum_{n}^{M-1}\left[\frac{M-n}{n}\right][Q]^n\right\}\right), \quad (2)$$

where Re means the real part of the final matrix, Spur is the sum of the diagonal terms of the real matrix, L_p is the Lorentz polarization factor, M is the number of layers per stack, $n = 1, \ldots, 1–M–1$, $[\Phi]$, is the matrix of the structural factor, $[I]$ is the unitary matrix, $[W]$ is the diagonal matrix of the proportions of the different types of layers, and $[Q]$ is the matrix representing the interference phenomena between the adjacent layers.

The modeling approach allowed us to identify the abundance of different layer types abundances (W_i), the type and the abundance of the mixed layer structure MLS, the stacking mode of different layer types, the average number M of layers per coherent scattering domain (CSD), and the IS water molecule distribution [78]. Within a CSD, layer stacking is described by a set of junction probabilities (P_{ij}). Briefly, the relationship between probabilities and W_i abundance of two different types of layers (i and j) can be summarized as follows: (i) the segregation tendency is given by $W_i < P_{ii}$ and $W_j < P_{jj}$, (ii) total demixing is obtained for $P_{ii} = P_{jj} = 1$, (iii) the regular tendency is obtained if $W_i < P_{ji} < 1$ and $W_j < P_{ij} < 1$, and (iv) finally, the boundary between the last distribution labeled chaotic/or random is obtained when $W_i = P_{ji} = P_{ii}$ and $W_j = P_{ij} = P_{jj}$ with $\Sigma W_i = 1$ and $\Sigma P_{ij} = 1$ [42, 100].

The modeling strategy consists of the theoretical reproduce of the experimental XRD profile initially from a homogeneous structure subsequently improved by adding other supplementary contributions. The existence of two mixed-layer structures (MLS) does not reflect the presence of two populations of particles physically present in the sample [48, 79, 101]. Therefore, layers with the same hydration state present in different MLS contributing to the diffracted intensity are assumed to have identical properties (chemical composition, layer thickness, and z-coordinates of atoms). The details of the XRD modeling approach are explained in detail in previous work of [41, 48, 78, 79, 101]. The atomic coordinates z in the 2 : 1 layer framework (octahedral layer sandwiched between two tetrahedral layers) are shown in Table 2. The z-coordinates of the IS content (exchangeable cation, molecules, etc.) are optimized, during the modeling process [66, 102], to improve the agreement R_{wp}:

$$R_{\mathrm{WP}} = \sqrt{\frac{\sum\left\{I(2\theta_i)_{\mathrm{exp}} - I(2\theta_i)_{\mathrm{calc}}\right\}^2}{\sum\left\{I(2\theta_i)_{\mathrm{exp}}\right\}^2}} \times 100\%, \quad (3)$$

where $I(2\theta_i)_{\mathrm{exp}}$ is the experimental diffracted intensity, and $I(2\theta_i)_{\mathrm{calc}}$ is the calculated ones.

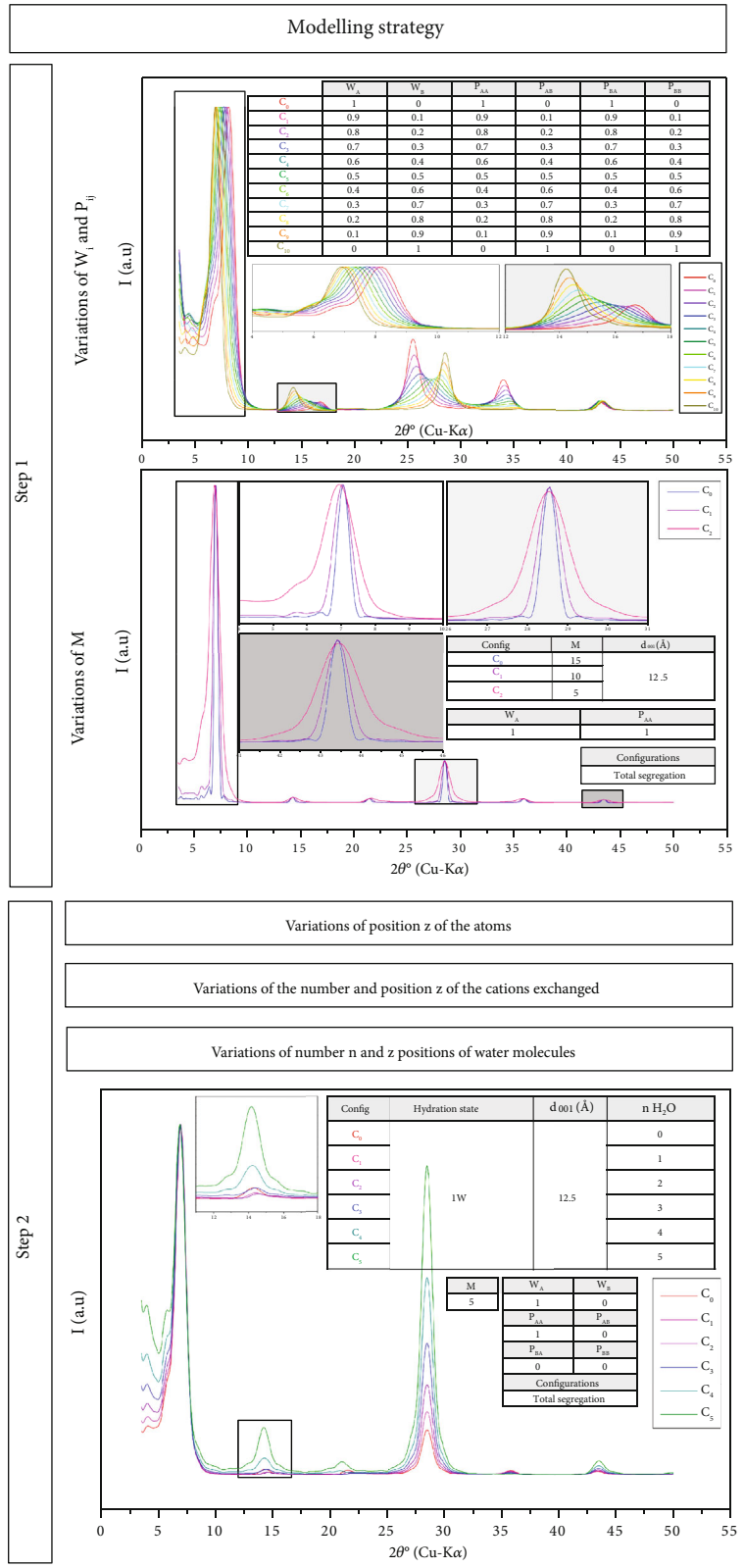

Figure 4: The main input structural parameter for the XRD modeling approach.

2.6.3. Modeling Strategy. The search for optimal structural parameters passes necessary through the determination of the shape function called "modulation function." It is related to the positions of the characteristic XRD reflections, by making the variations of the following parameters: (i) the W_i proportions of the different distances and the relative probabilities P_{ij} of succession law between layer type i and layer type j and (ii) the average layer number M per stack.

Table 3: Examples of half-cell structural formulas for raw montmorillonite SWy-2 and exchanged (SWy-2) with sodium and heavy metals at full saturation.

Samples	Structural half-cell formula
SWy-2	$(Si^{4+}_{3.96}, Al^{3+}_{0.04})\ (Al^{3+}_{1.53}, Fe^{3+}_{0.18}, Fe^{2+}_{0.045}, Mg^{2+}_{0.26}, Ti^{4+}_{0.01})\ O_{10}\ (OH)_2\ (Ca^{2+}_{0.07}, K^{+}_{0.01}, Na^{+}_{0.2})$
SWy-Na	$(Si^{4+}_{3.96}, Al^{3+}_{0.04})\ (Al^{3+}_{1.53}, Fe^{3+}_{0.18}, Fe^{2+}_{0.045}, Mg^{2+}_{0.26}, Ti^{4+}_{0.01})\ O_{10}\ (OH)_2\ (Na^{+}_{0.28})$
SWy-Co	$(Si^{4+}_{3.96}, Al^{3+}_{0.04})\ (Al^{3+}_{1.53}, Fe^{3+}_{0.18}, Fe^{2+}_{0.045}, Mg^{2+}_{0.26}, Ti^{4+}_{0.01})\ O_{10}\ (OH)_2\ (Co^{2+}_{0.14})$
SWy-Cu	$(Si^{4+}_{3.96}, Al^{3+}_{0.04})\ (Al^{3+}_{1.53}, Fe^{3+}_{0.18}, Fe^{2+}_{0.045}, Mg^{2+}_{0.26}, Ti^{4+}_{0.01})\ O_{10}\ (OH)_2\ (Cu^{2+}_{0.14})$
SWy-Ba	$(Si^{4+}_{3.96}, Al^{3+}_{0.04})\ (Al^{3+}_{1.53}, Fe^{3+}_{0.18}, Fe^{2+}_{0.045}, Mg^{2+}_{0.26}, Ti^{4+}_{0.01})\ O_{10}\ (OH)_2\ (Ba^{2+}_{0.14})$

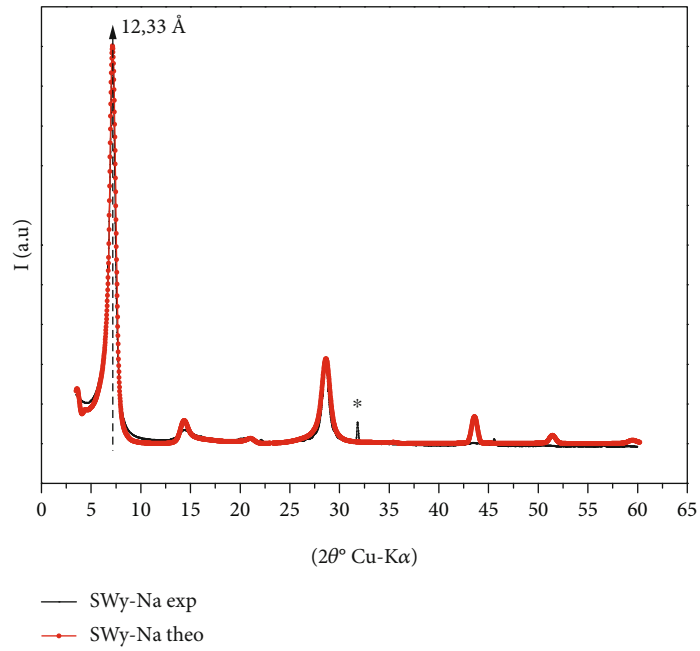

Figure 5: Best agreement between theoretical and experimental XRD profiles obtained in the case of SWy-Na. *Halite (NaCl).

Table 4: Qualitative XRD investigation in the case of the samples SWy-Na, SWy-Co, SWy-Cu, and SWy-Ba [47, 97].

Sample	$2\theta^\circ$	d_{001} (Å)	FWHM ($2\theta^\circ$)	D (Å)	ξ (Å)	Character
SWy-Na	7.16	12.33	0.74	18.77	0.062	Homogeneous
SWy-Co [47]	5.86	14.88	0.71	19.55	0.520	Interstratified
SWy-Cu [47]	7.14	12.36	0.61	22.77	0.100	Homogeneous
SWy-Ba [91]	5.91	14.94	1.55	08.96	0.970	Interstratified

Notes: $2\theta^\circ$: Bragg's angle; d_{001}: basal distance of the 1st reflection; D: average crystalline size; FWHM: full width at half maximum; ξ: rationality deviation parameters.

The agreement between theoretical and experimental profile is improved (decrease of R_{WP} value) by some adjustment attributed to the following parameters: (i) the z position of the layer atom composition along the c^* axis, (ii) the number and position z of the exchangeable cations, and (iii) the abundance and the configuration (their z positions following the normal at the sheet plane [82, 99, 103, 104] of the interlayer water molecules). A brief modeling strategy summary is reported in Figure 4.

2.7. Thermal Analysis: Thermogravimetry/Differential Thermal Analysis (TG/DTA). The hydration properties are very sensitive to the amount of water molecule which is identified by TG-DTA thermal analyses coupled with the "Labsys TG" model. All TG-DTA records are realized at variable temperatures from 0 to 500°C at a speed of 5°C/min. The used gas stream is argon. Approximately 10 mg of sample was used in platinum pans in each analysis. The determination of nH_2O necessarily depends on the results drawn from the TG-DTA curves followed by a theoretical calculation via modeling. After having optimized the theoretical XRD models, a structural formula per half unit cell can be determined by taking into account the weighting of each MLS and then of each layer population and its specific weighting as well as the average number of layers per crystallite (Table 3). Subsequently, the molar mass of the obtained results is calculated. The number of nH_2O (abundance) is estimated according to the following parameters: the initial

Table 5: Optimum structural parameters used for modeling XRD profiles in the case of baseline samples [47, 97].

Sample	% MLS	d_{001}	nH_2O	W_A	P_{AA}	S_M	M	R_{WP} (%)
SWy-Na	80	10.5	0	0.80	0.85	R_{1-seg}	10	2.27
	20	12.5	2					
SWy-Co [47]	16	12.4	1.1	0.16	0.30	R_{1-seg}	8	4.25
	84	15.2	1.9					
SWy-Cu [47]	95	12.4	1.1	0.95	0.05	R_{1-seg}	8	3.82
	05	15.2	1.9					
SWy-Ba [91]	64	12.4	1.1	0.15	0.15	R_0	8	3.77
		15.2	1.9					
	36	12.4	1.1	0.65	0.77	R_{1-seg}		
		15.2	2.0					

Notes: d_{001}: interlamellar distance; nH_2O: number of water molecules per half-cell; zH_2O: position of the molecules along the c^* axis of the H_2O molecule is attached to 9.6 Å for hydration states 1 W. The position of the exchangeable cations per half-cell calculated along the axis c^* is fixed à 9.6 Å for hydration states 1 W [41]. M: average number of sheets per stack; S_M: layer stacking mode; R_0: maximum order; R_1: random stacking; R_{1-X}, associated stacking (segregation-partial order); C: characters; Ho: homogeneous; He: heterogeneous; R_{WP}: confidence factor.

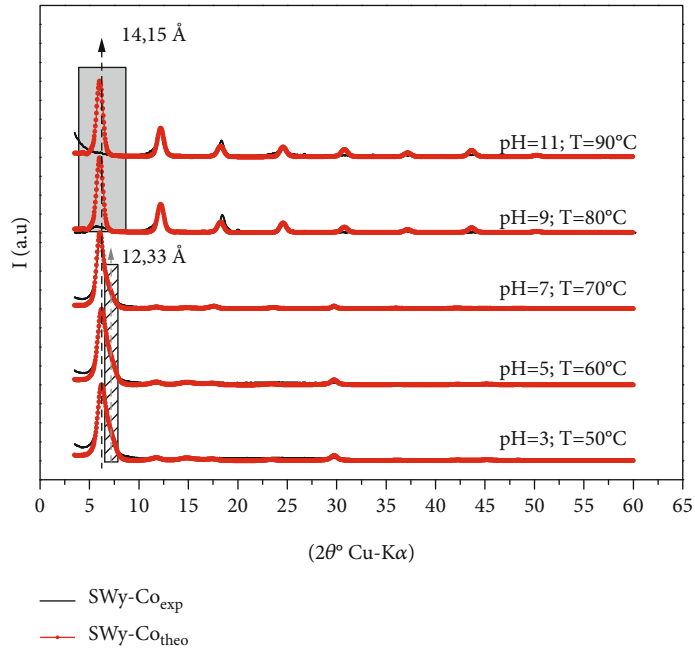

Figure 6: Best agreement between theoretical and experimental XRD profiles obtained in the case of SWy-Co.

mass $m_{initial}$ of the sample before analysis, the variation in sample mass Δm, the average number of layers M, and the number of moles n (deduced from masse molar).

2.8. Adsorption Analysis and Porosity Investigation. This study uses BET analysis in order to gain insight in particular surface area (SA) estimation in the case of porous materials, yielding knowledge in the effects of porosity fate and particle size evolution versus constraint strength [41, 105, 106]. This goal is achieved by multilayer nitrogen adsorption isotherm variation (performed at 77 K) versus relative pressure (P /P0~0.95). This task is fully automated manipulating Quantachrome NOVA 2000e series volumetric gas adsorption instrument. BJH analysis is employed to define pore area and specific pore volume by means of adsorption and desorption procedures. Also, the pore size distribution (PSD) was identified assuming several pores shape approximations. The adsorbed nitrogen and oxygen were eliminated under reduced (vacuum) pressure at 100°C for 8 h before measuring SA and PSD [107–110].

3. Results and Discussion

3.1. Semiquantitative XRD Investigation of the Baseline Samples. The experimental XRD profile of the starting SWy-Na complex (Figure 5) shows three characteristic reflections ($n = 1$, 2, and 4). The first reflection (001) is located at $2\theta = 7.16°$ ($d_{001} = 12.33$ Å) probably indicating a hydration 1 W state (Table 4). By calculating the FWHM and ξ parameter value, the homogeneous observed character is confirmed [111, 112]. This result is consistent with the results of [48] on the same sample. Na-rich montmorillonite

Table 6: Qualitative XRD investigation in the case of the samples SWy-Co SWy-Cu and SWy-Ba.

Samples		$2\theta^{\circ}$	d_{001} (Å)	FWHM ($2\theta^{\circ}$)	D (Å)	ξ (Å)	Characters
SWy-Co	pH = 3; T = 50°C	06.22	14.20	1.27	10.93	0.563	Interstratified
	pH = 5; T = 60°C	06.24	14.15	1.18	11.77	0.653	
	pH = 7; T = 70°C	06.09	14.50	1.00	13.89	0.406	
	pH = 9; T = 80°C	06.07	14.55	1.93	07.19	0.109	
	pH = 11; T = 90°C	*	*	*	*	*	
SWy-Cu	pH = 3; T = 50°C	07.16	12.34	0.61	22.77	0.016	Homogeneous
	pH = 5; T = 60°C	07.03	12.57	0.71	19.57	0.096	
	pH = 7; T = 70°C	07.08	12.48	1.74	07.98	0.114	
	pH = 9; T = 80°C	07.06	12.51	1.97	07.05	0.207	Interstratified
	pH = 11; T = 90°C	07.00	12.62	2.14	06.49	0.270	
SWy-Ba	pH = 3; T = 50°C	07.18	12.30	0.70	19.85	0.055	Homogeneous
	pH = 5; T = 60°C	07.14	12.37	1.30	10.69	0.013	Interstratified
	pH = 7; T = 70°C	07.20	12.27	0.55	25.26	0.091	
	pH = 9; T = 80°C	07.18	12.30	0.68	20.43	0.216	Homogeneous
	pH = 11; T = 90°C	07.35	12.02	0.57	24.38	0.064	

Notes:*absence of the 001 reflection.

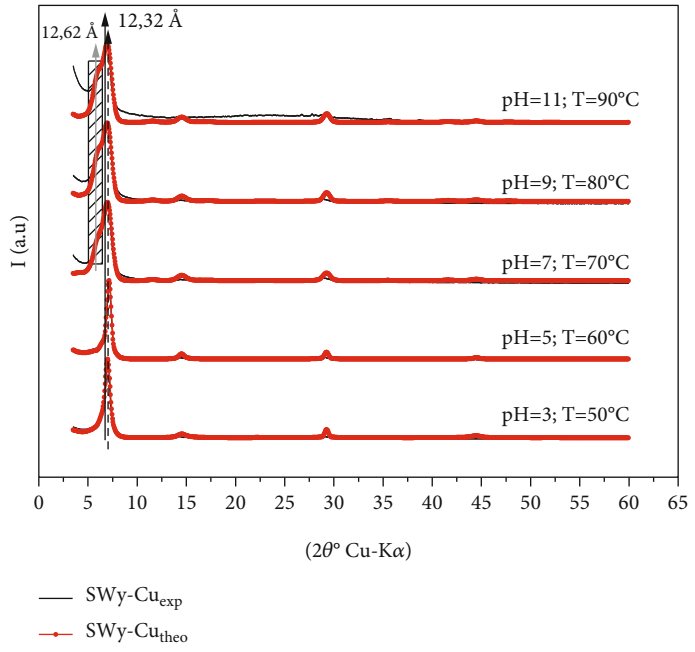

Figure 7: Best agreement between theoretical and experimental XRD profiles obtained in the case of SWy-Cu.

(SWy-Na) has been studied extensively before since it is considered a reference sample [5–7, 41, 48, 78–79, 89, 113]. At this level, our goal is to refine the obtained literature results related to the SWy-Na sample. For the SWy-Cu, SWy-Co, and SWy-Ba samples, qualitative and quantitative XRD results extracted from the same authors earlier works [47, 97] are used (Tables 4 and 5).

3.2. Modeling of XRD Profiles in the Case of SWy-Na Sample. The mixed layer structure (MLS) used to achieve the best agreement between the experimental and calculated XRD model (Figure 5) shows an heterogeneous hydration character that results in the coexistence of two types of layers (0 W and 1 W) with a strong dominance for the 1 W phase at about 80%. This opposes the obtained qualitative description.

Indeed, the distribution of IS water molecules has respected the previous work [5, 6, 48, 88, 101] with a water sheet located in the middle of the IS for 1 W phase and the absence of water in the IS for the dehydrated state 0 W. Regardless of the type of hydration state, the exchangeable cations Na (per half-cell unit) are positioned in the center of the IS along the c^* axis respecting the configuration of

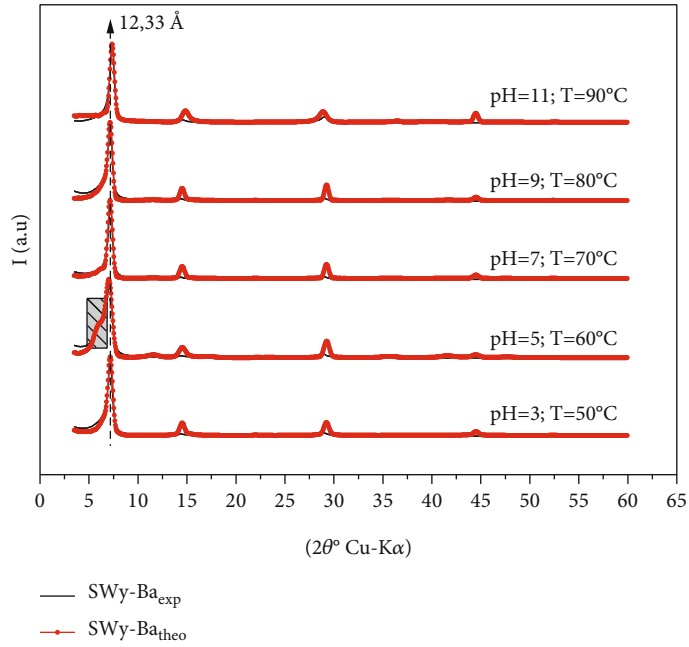

Figure 8: Best agreement between theoretical and experimental XRD profiles obtained in the case of SWy-Ba.

the data provided by the literature [5, 48]. The average number of layers per crystallite M is equal to 10. The confidence factor R_{WP} is very low (2.27%), which reflects the high quality of fitting. The structural parameters are summarized in Table 5.

3.3. Semiquantitative Description of XRD Analysis after Applying First-Order Coupling Stress

3.3.1. Case of the SWy-Co Sample. The experimental XRD results for the SWy-Co samples obtained are shown in Figure 6. For the first three constraint coupling levels (pH = 3; T = 50°C ⟶ pH = 7; T = 70°C), there is an asymmetry for the main 001 reflections located at 6.1 in 2θ° with d_{001} ~ 14.5 Å synonymous of a minor 2 W hydration state presence attributed to the Co^{2+} cation in IS. Also, a shoulder towards the wide angles around in 7.2° in 2θ (d_{001} ~ 12.3 Å) attributed to the existence of the sodium residue resulting from the starting sample. Generally, the observed asymmetric 001 reflections indicates the coexistence of several hydration states within the crystallite and/or a partial cation exchange process. The values of the FWHM and ξ parameters confirms this idea (Table 6).

In Table 6, for the rest of the samples, a different hydration behavior was observed. The diffracted intensity ratio I_{001}/I_{002}, I_{001}/I_{003}, and I_{001}/I_{004} of the complex studied under (pH = 9, T = 80°C/pH = 11, T = 90°C) decreases if compared with the three first studied samples. Also, a drastic decrease in the 001-reflection intensity is observed in both samples and which probably indicates a bottom transformation that affected the structure when increasing constraints strength. This strange structural behavior finds an explanation by the effect of the increase in temperature and the basic aspect of the soil solution pH on the cohesion energy between layers and even destruction of the chemical bonds within octahedral and tetrahedral sheet forming the layer. The main structure is affected and an elevated layer's exfoliation trends within the crystallites favoring a total transformation of the original 2 : 1 phase to a 1 : 1 clay structure that was established. The raised value of the 002-reflection intensity and the absence of the 001 line can be interpreted in this case by the beginning of a great structural transformation. This remains to be proven by quantitative XRD analysis and by studying the porosity evolution of these two samples.

3.3.2. Case of the SWy-Cu Sample. The experimental XRD models, in the case of SWy-Cu, obtained by varying the external constraint strength are summarized in Figure 7. For the first two constraints of the coupling value (pH = 3; T = 50°C and pH = 5; T = 60°C), the experimental XRD models are almost identical with a low FWHM value (Table 6) indicating probably either the coexistence, within the stacks, of several hydration states [77] or an unfinished (partial) cation exchange, knowing that Cu^{2+} cation is indistinguishable from the starting sodium by simple XRD analysis at room conditions from the starting sodium cation [47]. All qualitative parameters are summarized in Table 6. For the rest of the complexes (pH = 7; T = 70°C ⟶ pH = 11; T = 90°C), a stack towards the small angles (5.9° ⟶ 15 Å) appeared and ascribed to the material response to the applied stress. Indeed, a beginning of 2 W transition, without a real domination, is confirmed by increasing the coupling constraint intensity. It remains to be noted that the higher-order peaks have a relatively low intensity regardless surrounding environment change and from soil solution pH value = 7 and temperature T = 70°C, an abrupt structural change is observed.

3.3.3. Case of the SWy-Ba Sample. The experimental XRD profiles of SWy-Ba sample are reported in Figure 8. An

Table 7: Structural parameters of SWy-Co, SWy-Cu, and SWy-Ba.

Samples		% MLS	xW-echa.cat	d_{001}	nH_2O	W_A	P_{AA}	S_M	M	M_{tot}	R_{WP}
SWy-Co	pH = 3; T = 50°C	16.68	1 W-Na	12.2	0.0442	1	1	R_0	05		
		83.28	1 W-Na	12.2	0.0346	0.40	0.55	R_{1-seg}	10	9	3.61
			2 W-Co	15.2	0.0259						
					0.0259						
	pH = 5; T = 60°C	16.70	1 W-Na	12.2	0.0322	1	1	R_0	05		
		83.30	1 W-Na	12.2	0.0252	0.40	0.55	R_{1-seg}	10	9	3.79
			2 W-Co	15.2	0.0189						
					0.0189						
	pH = 7; T = 70°C	35	1 W-Na	12.2	0.0230	0.35	0.63	R_{1-seg}	08	8	3.42
		65	2 W-Co	15.2	0.0300						
					0.0300						
	pH = 9; T = 80°C	40	1 W-Na	12.2	0.0200	0.40	0.40	R_0	07	7	7.45
		60	2 W-Co	15.2	0.0243						
					0.0243						
	pH = 11; T = 90°C	40	1 W-Na	12.2	0.0101	0.40	0.40	R_0	07	7	9.12
		60	2 W-Co	15.2	0.0113						
					0.0113						
SWy-Cu	pH = 3; T = 50°C	81.23	1 W-Na	12.2	0.1166	0.95	0.95	R_0	14	12	3.84
			2 W-Cu	15.2	0.0031						
					0.0031						
		18.77	1 W-Na	12.2	0.0333	0.95	0.95	R_0	04		
			2 W-Cu	15.2	0.0009						
					0.0009						
	pH = 5; T = 60°C	84.20	1 W-Na	12.2	0.0797	0.85	0.86	R_{1-seg}	14	12	3.56
			2 W-Cu	15.2	0.0070						
					0.0070						
		15.80	1 W-Na	12.2	0.0228	0.85	0.86	R_{1-seg}	04		
			2 W-Cu	15.2	0.0020						
					0.0020						
	pH = 7; T = 70°C	75	1 W-Na	12.2	0.0410	0.75	0.90	R_{1-seg}	10	10	4.92
		25	2 W-Cu	15.2	0.0068						
					0.0068						
	pH = 9; T = 80°C	70	1 W-Na	12.2	0.0250	0.70	0.87	R_{1-seg}	08	8	6.04
		30	2 W-Cu	15.2	0.0148						
					0.0148						
	pH = 11; T = 90°C	70	1 W-Na	12.2	0.0284	0.70	0.87	R_{1-seg}	08	8	7.73
		30	2 W-Cu	15.2	0.0061						
					0.0061						
SWy-Ba	pH = 3; T = 50°C	72.17	1 W-Na	12.2	0.1001	1	1	R_0	12		
		27.83	1 W-Na	12.2	0.0446	0.90	0.89	$R_{1-p.ord}$	06	10	5.41
			2 W-Ba	15.2	0.0045						
					0.0045						
	pH = 5; T = 60°C	84	1 W-Na	12.2	0.0978	0.84	0.91	R_{1-seg}	10	10	5.96
		16	2 W-Ba	15.2	0.0093						
					0.0093						
	pH = 7; T = 70°C	95	1 W-Na	12.2	0.0905	0.95	0.97	R_{1-seg}	12	12	5.22
		05	2 W-Ba	15.2	0.0045						
					0.0045						

Table 7: Continued.

Samples	% MLS	xW-echa.cat	d_{001}	nH_2O	W_A	P_{AA}	S_M	M	M_{tot}	R_{WP}
pH = 9; T = 80°C	65.75	1 W-Na	12.2	0.0611	1	1	R_0	13	13	5.37
	34.25	1 W-Na	12.2	0.0202	0.80	0.85	R_{1-seg}	13		
		2 W-Ba	15.2	0.0025						
				0.0025						
pH = 11; T = 90°C	15	0 W-Na	10.2	0.0000	0.85	0.83	$R_{1-p.ord}$	13	13	5.16
	85	1 W-Ba	12.2	0.0750						

Notes: xW-echa.cat: layer type and associated exchangeable cation; d_{001}: interlamellar distance; nH_2O: number of water molecules per half-cell; zH_2O: position of the molecules along the c^* axis of the H_2O molecule is attached to 9.6 Å and 11.3 Å–13.9 Å for hydration states 1 W and 2 W, respectively. The position of the exchangeable cations per half-cell calculated along the axis c^* is fixed with 9.60 Å and 12.25 Å for hydration states 1 W and 2 W [41]; n-echa.cat: number of exchangeable cations per half-cell is set to 0.28 (for the cation Na^+) and at 0.14 (for bivalent metal cations), indicating complete saturation of cation exchange capacity (CEC); M: average number of sheets per stack; M_{tot}, total average number of sheets per stack; S_M: layer stacking mode; R_0: maximum order; R_1: random stacking; R_{1-X}: associated stacking (segregation-partial order); C: characters; Ho: homogeneous; He: heterogeneous; R_{WP}: confidence factor.

Table 8: Results from TG/DTA analyses in the case of samples SWy-Co, SWy-Cu, and SWy-Ba.

Samples		$m_{initial}$ (mg)	Δm (mg)
SWy-Co	pH = 3; T = 50°C	15.90	09.974
	pH = 5; T = 60°C	16.60	13.387
	pH = 7; T = 70°C	06.80	01.820
	pH = 9; T = 80°C	17.10	11.074
	pH = 11; T = 90°C	12.30	08.605
SWy-Cu	pH = 3; T = 50°C	17.50	12.975
	pH = 5; T = 60°C	17.40	14.246
	pH = 7; T = 70°C	15.70	12.836
	pH = 9; T = 80°C	11.30	06.972
	pH = 11; T = 90°C	14.00	10.848
SWy-Ba	pH = 3; T = 50°C	15.00	06.773
	pH = 5; T = 60°C	23.60	19.570
	pH = 7; T = 70°C	15.00	06.731
	pH = 9; T = 80°C	15.40	03.501
	pH = 11; T = 90°C	19.10	12.462

Notes: $m_{initial}$: initial mass of the samples before analysis; Δm: change in mass during analysis.

Table 9: Radius and ionic potential of some cations [110].

Cations	Ionic potential (eV)	Ionic radius (Å)
Na^+	1.05	0.95
Ba^{2+}	1.48	1.35
Cu^{2+}	2.74	0.73
Co^{2+}	3.08	0.65

intense 001 reflection situated at 7.2° (2θ) (d_{001} ~ 12.3 Å) indicating a 1 W hydration state dominates all sample. This probably reflects the existence of a Na^+ residue originating from the starting sample or from added NaOH solution used to balance the pH solution. This opposes the earlier results [41, 97] on cation exchange in the case of Ba^{2+} which demonstrate a 2 W hydration state behavior.

For pH = 5/T = 60°C, the XRD profile shows a shoulder towards the low angles (5.8° ⟶ d_{001} = 15.23 Å) with an increase in the FWHM and ξ parameter value indicating the 2 W hydration state transition beginning. Also, it can be interpreted by the coexistence, within the stacks, of several states of hydration [77] or an unfinished (partial) cation exchange knowing that the barium hydrate baseline to two layers of water 2 W (15 Å). All qualitatively estimated parameters are summarized in Table 6.

3.4. XRD Modeling Profiles after Applying First-Order Coupling Stress

3.4.1. Case of the SWy-Co Samples. The qualitative XRD analysis suggested heterogeneous hydration behavior for SWy-Co samples, regardless of the strength of the stresses applied. This interstratification has been approved by the 001 reflection modeling approach which assumes the coexistence of two different hydration states (e.g., 1 W and 2 W). To improve the agreement between the calculated and experimental models (Figure 6) and for each constraint strength from pH = 5/T = 60°C towards pH = 11/T = 90°C, the proposed MLS is theoretically decomposed into two layer populations type (i.e., 1 W: d_{001} ~ 12.2 Å and 2 W: d_{001} ~ 15.2 Å) stacked according to specific succession probability laws. The structural parameters associated with this modeling approach are summarized in Table 7. The proposed MLS is obtained by weighted layer populations that are tolerated to have an identical chemical composition, identical layer thickness, and identical z-atoms coordinates [40, 48]. The CEC of the results is partially saturated by the Na^+ and Co^{2+} cations since, under ambient conditions, sodium always has a hydration state of 1 W [41, 48], and cobalt has a hydration state of 2 W.

The theoretical decomposition of the SWy-Co sample, (pH = 11; T = 90°C) which has undergone fundamental changes in its basic structure, can be followed by two major hypotheses:

The 1st consists in considering that it is still a T-O-T type structure despite the absence of the main 001 reflection which must be positioned around 6.1° (2θ) (d_{001} ~ 14.5 Å) and can be attenuated (is no longer sensitive to X-rays during diffractogram recordings) following the increase in the

Table 10: Evolution of the nH_2O amounts versus constraint strength for samples SWy-Co, SWy-Cu, and SWy-Ba.

Samples		Phases	Saturation		m_{molar} (g/mol)	M	nH_2O
			% Na^+	% M^{2+}			
SWy-Co	pH = 3; T = 50°C	Phase 1	100	0	370.864	05	0.0442
		Phase 2	16.68	83.28	379.250	10	0.0865
	pH = 5; T = 60°C	Phase 1	100	0	370.864	05	0.0322
		Phase 2	16.70	83.30	379.248	10	0.0630
	pH = 7; T = 70°C	Ø	35	65	377.406	08	0.0833
	pH = 9; T = 80°C	Ø	30	70	377.909	07	0.0686
	pH = 11; T = 90°C	Ø	30	70	377.909	07	0.0327
SWy-Cu	pH = 3; T = 50°C	Phase 1	95	05	371.432	14	0.1228
		Phase 2	95	05	371.432	04	0.0351
	pH = 5; T = 60°C	Phase 1	85	15	372.568	14	0.0937
		Phase 2	85	15	372.568	04	0.0268
	pH = 7; T = 70°C	Ø	75	25	373.703	10	0.0546
	pH = 9; T = 80°C	Ø	70	30	374.271	08	0.0358
	pH = 11; T = 90°C	Ø	70	30	374.271	08	0.0406
SWy-Ba	pH = 3; T = 50°C	Phase 1	100	00	370.864	12	0.1001
		Phase 2	90	00	374.066	06	0.0496
	pH = 5; T = 60°C	Ø	84	16	375.988	10	0.1164
	pH = 7; T = 70°C	Ø	95	05	372.465	12	0.0995
	pH = 9; T = 80°C	Phase 1	100	00	370.864	13	0.0611
		Phase 2	80	20	377.267	13	0.0252
	pH = 11; T = 90°C	Ø	15	85	398.076	13	0.0750

Notes: phases: modeling phase of each sample; Ø: absence of phases; m_{molar}: molar mass of the sample related to each phase; 4: average number of layers per stack; nH_2O: number of water molecules per half-cell bound to each phase.

applied stress strength. In this case, a theoretical model based on the heterogeneous mixed 1 W/2 W structure with a major domination for the phase 2 W was adopted with very low average layer number per crystallite. This hypothesis can be practically verified for the good agreement towards higher diffraction orders.

The 2nd considers that the basic clay structure has been strictly modified following the coupled increase in temperature T and the soil solution pH during the cation exchange process. This supposition is justified through the destruction of chemical bonds within the crystallite and/or which give rise to a new structure derived from smectite. This result, despite its originality, agrees with the work of [108, 109] which focuses on the hydrothermal synthesis of zeolite from clay minerals by controlling the pH effect on the synthesis process. Hence, the transition from a T-O-T phyllosilicate type (montmorillonite) to another kaolinite T-O phyllosilicate type is probabilistic, knowing that kaolinite has a dioctahedral structure [114–116]. Its structural half-cell formula is defined by (Si_4 Al_4 O_{10} $(OH)_8$), whose basal distance d_{001} is of the order of 7 Å [117–119] with a closed IS accompanied by the absence of isomorphic substitutions (not CC in the middle of IS). For this hypothesis (Figure 6), we consider that the first reflection (in the 1st hypothesis was considered as 2nd reflection 002) is positioned around 12° (2θ) (d_{001}~7 Å) from where the second reflection is necessarily positioned around 24° (2θ) (Table 7). For this hypothesis, we note the presence of a relatively intense reflection around 18° (2θ). A rational reflection position is obtained for the three reflections order (12° ⟶ 18° ⟶ 24°). Also, the exchangeable cation has no place in this configuration, which even calls into question the cation exchange process. Therefore, the first supposition seems more scientifically logical. The 1st hypothesis has been adopted in the rest of the calculations. It remains to be noted that the quality of the fitting is controlled by the R_{WP} parameter.

3.4.2. Case of the SWy-Cu Samples. The best agreement between theoretical and experimental XRD patterns (Figure 7) of the SWy-Cu samples is obtained using an interstratified structure of two MLS comprising various relative layers proportions with different hydration states (Table 7). This variability confirms the heterogeneous hydration character and the intermediate 1 W-2 W hydration phase observed regardless of the intensity of the applied constraints. In detail, a minor contribution of the 2 W phase increases from 5% to 30% by increasing the intensity of the external applied stress (pH = 3; T = 50°C ⟶ pH = 11; T = 90°C). Indeed, the 2 W hydration phase implemented in the theoretical model is necessarily attributed to the layer fraction whose CEC is saturated by Cu^{2+}. This weighting fluctuation is evidence of an incomplete cation exchange process (d_{001} < 15 Å). On the other hand, the dominance of

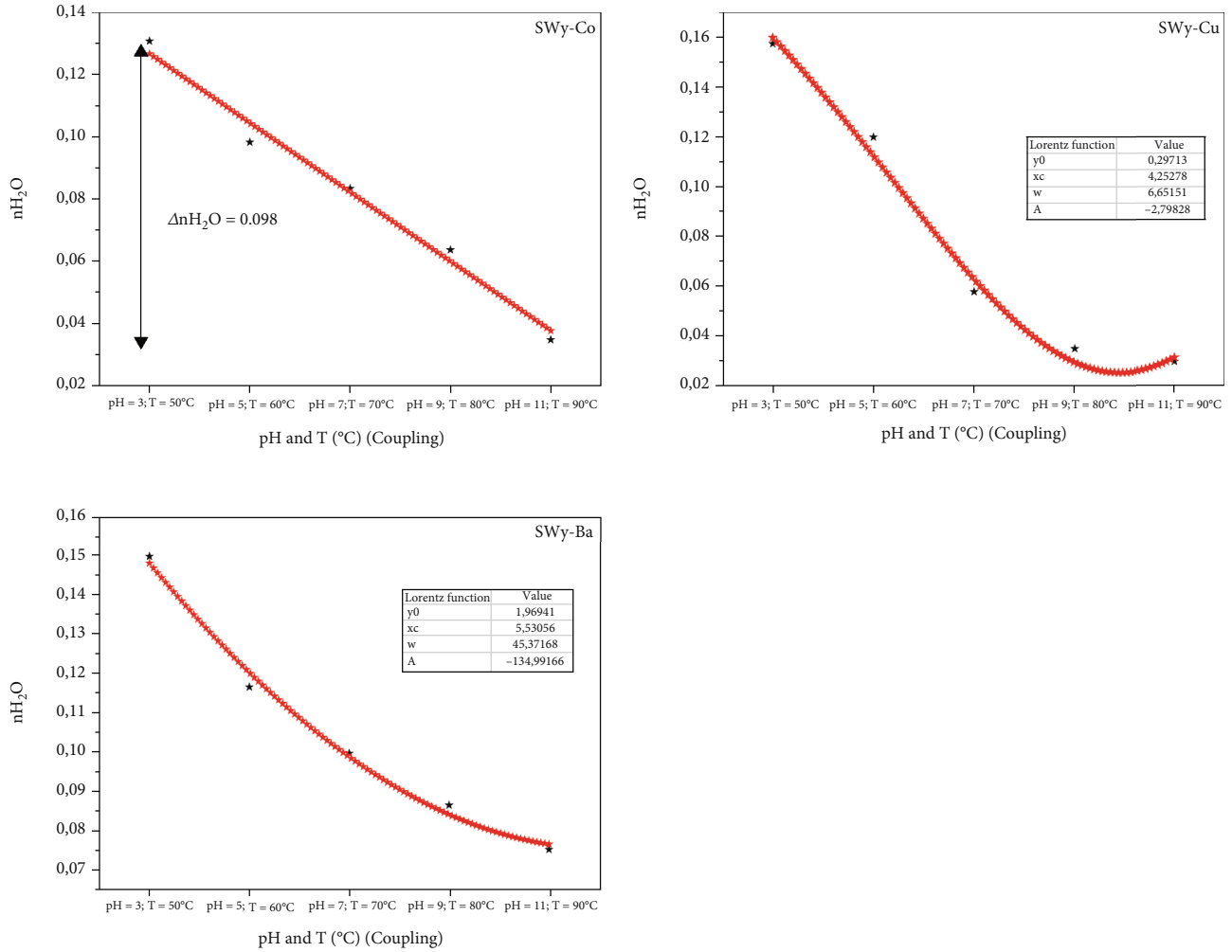

FIGURE 9: nH_2O abundance fluctuation as a function of stress strength for SWy-Co, SWy-Cu, and SWy-Ba samples (black scatter). Red scatter: the used linear and Lorentz fit function, respectively.

1 W layer hydration phase is interpreted by the existence of a fraction (quite large) regardless of the applied constraints applied. This contribution is attributed to the sodium residues from the starting sample (SWy-Na).

The agreements obtained between the experimental and theoretical profiles (R_{WP} ~ 3% to 8%) are generally acceptable (< 10%), despite the misfit observed after widening the peaks around 14° and 28° (2θ). In fact, this disagreement can be broken down into a good reflection position agreement and a disagreement of diffracted intensity related to the input fluctuation of the distribution and abundance of water molecules in the IS. This disagreement led us to explore wide-angle areas, later to establish a possible link between CEC saturation and the degree of hydration heterogeneity.

The logical increase of the R_{WP} factor in the case of SWy-Cu sample reflects the increase in the heterogeneity's degree defined, respectively, by an asymmetry of the first 001 reflections, the high FWHM value, and the ξ rationality parameter. Theoretically, this result is related to the variability of possible MLS configurations allowing a good fit of the 001 reflection. The exploitation of the W_A, P_{AA}, M, and R_{WP} values allowed us to characterize a specific distribution of the n normalized layers within the crystallites according to the generated stacking modes and the contribution of each phase. This statistical representation of the layer can help to understand the CEC sensitivity fluctuation (of the starting sample) following the variation in the temperature T and pH during the cation exchange process.

3.4.3. Case of the SWy-Ba Samples. For SWy-Ba samples, the best agreements between theoretical and experimental models are shown in Figure 8. The main structural parameters used to achieve a good fit are summarized in Table 7. For each model, several types of layers with variable stacking mode are used to improve the agreement obtained between the experimental and calculated models. This MLS is composed by several layers of type populations depending on the hydration state (0 W, 1 W, and 2 W) whose basal distance d_{001} is equal to 10.2 Å, 12.2 Å, and 15.2 Å, respectively. This variability confirms the heterogeneous hydration character observed by qualitative XRD analysis for the entire

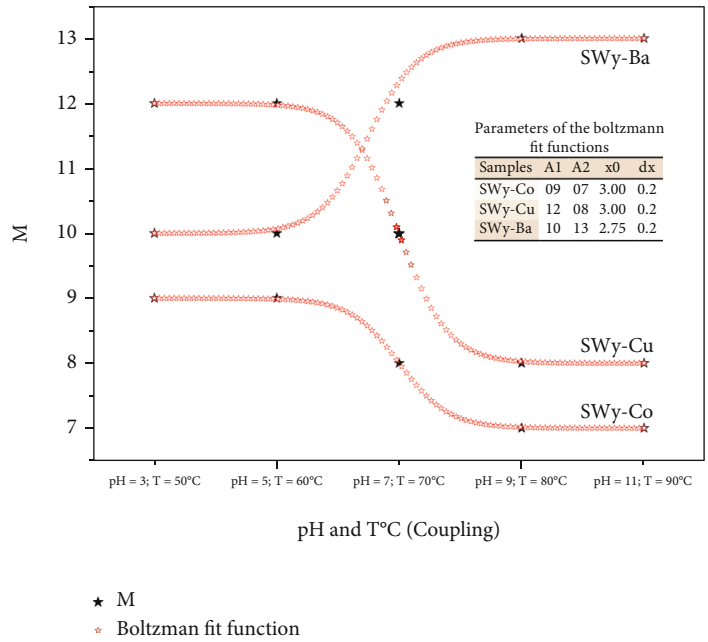

FIGURE 10: Average number of layers M evolution versus constraint strength in the case of SWy-Co, SWy-Cu, and SWy-Ba samples (black scatter). Red scatter: the used Boltzmann fit.

SWy-Ba series (pH = 3; $T = 50°C \longrightarrow$ pH = 11; $T = 90°C$) with a major dominance for the 1 W hydration phase saturated by Na^+ cation assigned to the starting sample. In addition, the 2 W phases are assigned to the fraction whose CEC is saturated by Ba^{2+} cation [41]. More specifically, for the first four samples from pH = 3/$T = 50°C$ towards pH = 9 /$T = 80°C$, an omnipresent minor contribution of the 2 W phase which does not exceed 16% is noted and which is evidence of the incomplete cation exchange process. In addition, the quite important dominance of the 1 W hydration phase (about 90%) is noted. The last sample (pH = 11; $T = 90°C$) has another intermediate phase 0 W/1 W which explain the observed decrease in basal distance probably resulting in the shrinkage of IS as a result of the temperature increase. The quality agreements obtained between the theoretical and experimental profiles are in average of ~5% which is generally acceptable.

3.5. Evolution of the Water Molecule Abundances versus Coupling Constraint Strength

3.5.1. Evolution of the nH_2O Amounts versus Constraint Strength. The delicate theoretical determination of nH_2O amounts for each studied sample is deduced from the results of thermogravimetry/differential thermal analysis (TG/DTA) (Figure S1) and summarized in Table 8.

Regardless of the sample type, the hydration state is governed by the cationic nature, the layer charge value, and the layer charge location [5–7, 107, 108, 120–122]. All samples studied belongs to the Wyoming montmorillonite specimen characterized by the same layer charge and the charge location value. The nature of the exchangeable cations and the external stresses applied to the cation exchange process (first-order coupling constraint) is at the origin of these specific water molecule amounts fluctuations. The water affinity of the exchangeable cation is related to the ionic potential which is defined by the ratio of the valence of the cation to its ionic radius [110] (Table 9). As this potential increases, the cation's affinity for water also increases. Indeed, bivalent cations such as cobalt (Co^{2+}), copper (Cu^{2+}), and barium (Ba^{2+}) have a high affinity of water translated by a 2 W hydration state [6, 7]. Unlike monovalent cations like sodium (Na^+), having a low affinity for water mainly generates monohydrated states 1 W.

Based on the quantitative XRD analysis, a discretization of the content of the IS is carried out. Indeed, the evolution of nH_2O molecules per half-cell, relative to the constraint strength, is described by Table 10 and represented in Figure 9. For all series, a decrease in the water molecules amounts as a function of the increase in temperature and soil solution pH.

In the case of SWy-Co sample (Figure 9), there is an overall linear decrease in the number of water molecules as a function of the increase applied stresses intensity (pH = 3 ; $T = 50°C \longrightarrow$ pH = 11; $T = 90°C$). Using a linear regression approach, a mathematical equation was developed. The behavior and evolution of the nH_2O abundance fluctuation re described by the following function:

$$y = 0.14888 - 0.02226.x, \tag{4}$$

where y is the nH_2O abundance fluctuation, and x is the applied stress intensity.

In the case of SWy-Cu and SWy-Ba samples (Figure 9), there is a nonlinear water molecule amount decrease unlike SWy-Co as a function of the increase in external stresses

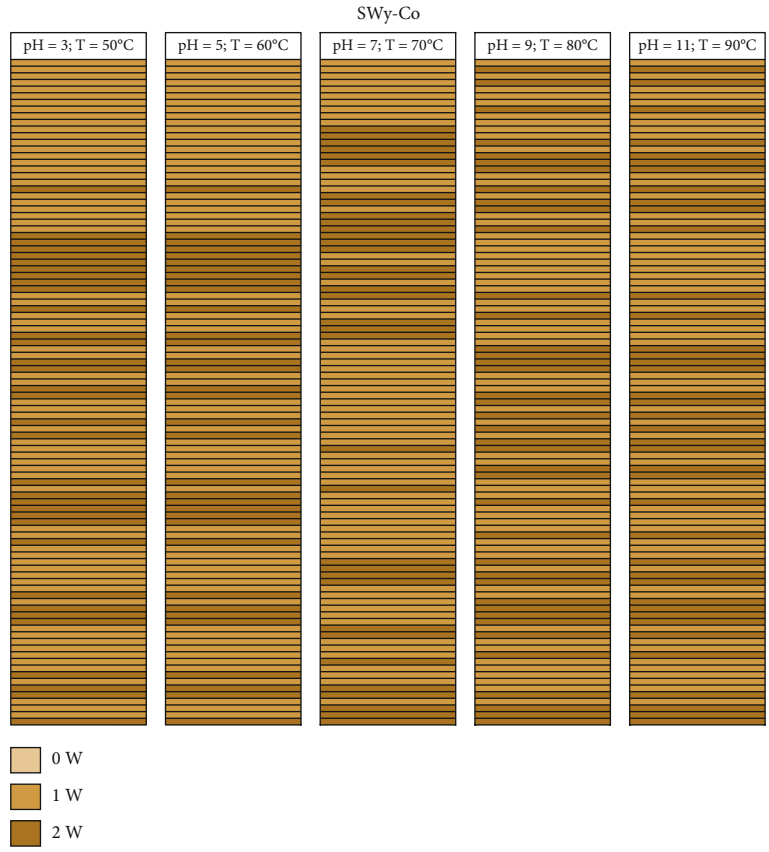

(a)

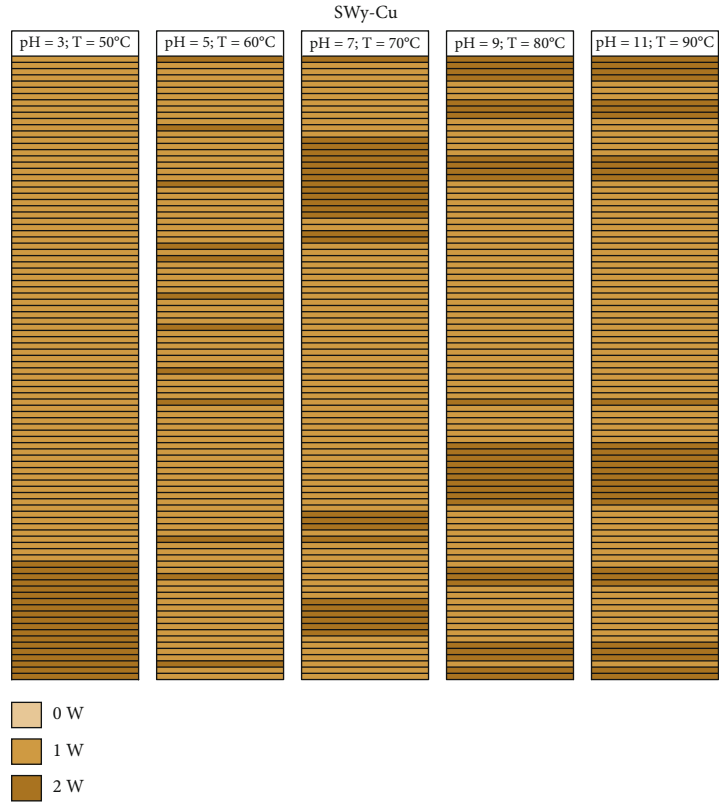

(b)

Figure 11: Continued.

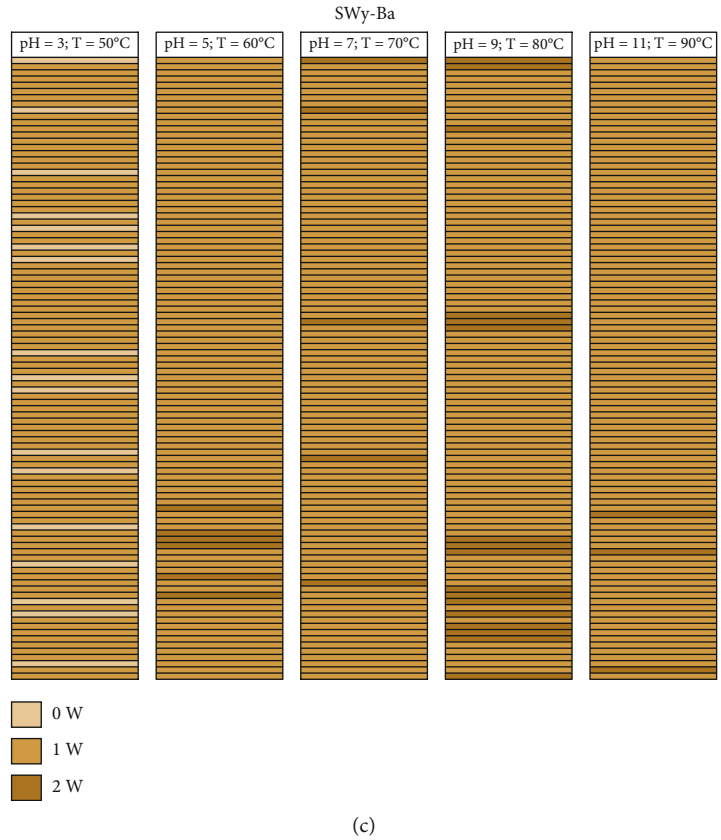

(c)

Figure 11: Mapping representation of the hydration state in the case of SWy-Co (a), SWy-Cu (b), and SWy-Ba (c) samples via XRD modeling approach.

applied. So, a regression approach based on the Lorentz equation was adopted to fit this evolution. This variation is described by function below:

$$y = y_0 + \left\{ \left(\frac{2A}{n} \right) \times \left(\frac{w}{4(x - x_c)^2 w^2} \right) \right\}, \quad (5)$$

where y_0 is the baseline offset, x_c is the center of the peak, w equals the width of the peak at half height, and A is the area under the peak. The parameters of the used Lorentz function are presented in Figure 9.

This decrease trends on the water molecule amount (nH_2O) versus constraint strength are predictable when increasing temperature which automatically affects the IS closing and subsequently, it affects the cation exchange capacity of the mineral.

3.5.2. Individual Evolution of the 0 W, 1 W, and 2 W Abundances versus Constraint Strength. The "water footprint" schematized on Figure S2 shows the coexistence within the particle of several phases with different weights. The variation of the cation exchange process makes it possible to better understand the structural response of the starting material (such as fluctuations in basal distance d_{001} , FWHM, crystalline size, rationality ξ, average number of layers M, and mode of stacking layers). Understanding the CEC functioning mode is closely related to the discretization of hydration states [48].

For SWy-Co samples, a decrease in the 1 W monohydrate state, accompanied by an increase in fluctuation for the 2 W hydration state, represents the main hydration behavior. This can be interpreted by an easy intercalation of the compensating cations (Co^{2+}) in IS more and more, replacing the sodium cations (Na^+) that will leave the structure partially according to the applied stress variation. This hypothesis is confirmed by the global incomplete exchange process despite the exchange equilibrium time provided and remains to be noted that abundances in the aqueous phase are normalized to 100%. For SWy-Cu samples, the same behavior of the previous sample (SWy-Co) is observed. A slight fluctuation for the 1 W hydration state followed by a slow increase of 2 W is noted. For the latest SWy-Ba samples, the water behavior is almost different. There is a slow decrease in the 1 W state. This fluctuation is accompanied by a slight increase of 2 W phases. This is not valid for the complex pH = 11 and $T = 90°C$ (extreme case) which has a minority anhydrate state of 0 W (15%) and a majority hydration state of 1 W (85%). The abundance of individual layer type deduced from the optimized theoretical MLS used to reproduce experimental XRD profiles was shown in Figure S3. Indeed, the 2 W hydration state is the most dominant phase in the entire SWy-Co series. Unlike the two complexes SWy-Cu and SWy-Ba, the 1 W hydration state is the most dominant phases.

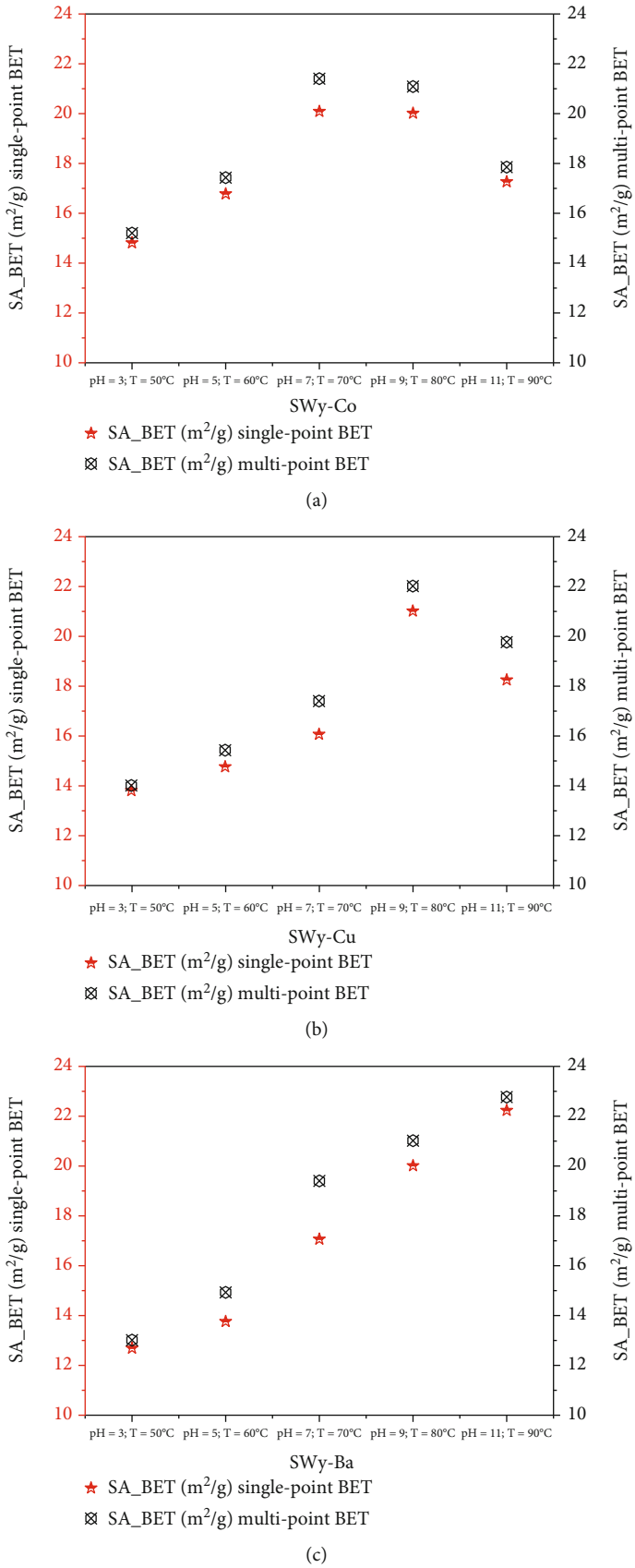

Figure 12: SA_{BET} single and multipoint BET evolution versus constraint strength for (a) SWy-Co, (b) SWy-Cu, and (c) SWy-Ba samples.

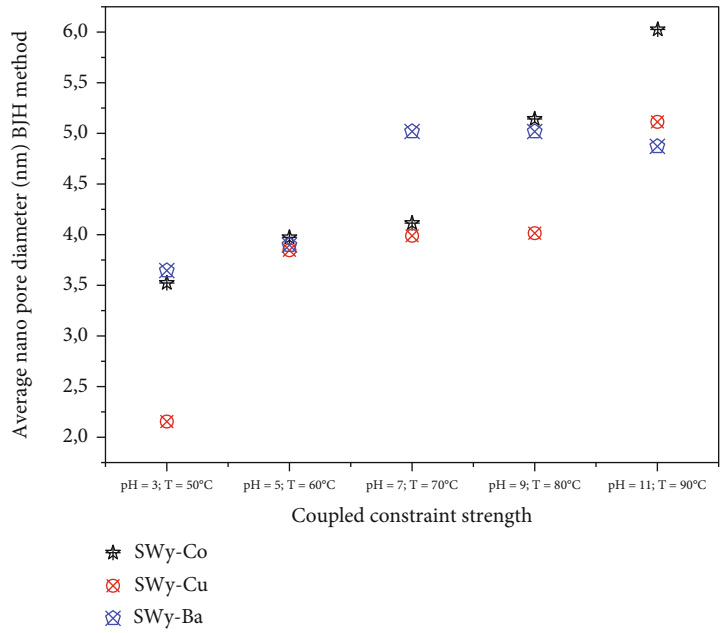

Figure 13: BJH method average pore diameter evolution versus constraint strength.

3.6. Evolution of the Average Number of Layers versus Constraint Strength. The average number of layers (M) is a very important parameter in the crystal structure clay response when studied by XRD analysis. It has a direct influence on the 001 reflections of the theoretical and experimental models. For the low M value, the reflections 001 will be very wide with elevated value of FMWH and vice versa. The evolution of M parameter for all SWy-Co, SWy-Cu, and SWy-Ba samples is shown in Figure 10.

The SWy-Ba sample is the exception and exhibits growth of M when increasing intensity constraint. The M evolution as a function of the applied stress applied is fitted for each sample and shown in Figure 10.

The evolution of M for all complexes following a Boltzmann function is shown below:

$$y = A_2 + \left\{\frac{(A_1 - A_2)}{1 + e^{(x - x_0/\mathrm{dx})}}\right\}, \quad (6)$$

where A_1 is the initial value, A_2 is the final value, x_0 is the center, and dx is a time constant.

All functions parameters are summarized in Figure 10.

3.7. Evolution of the Layer Stacking Modes. A mapping representation of the hydration state in the case of SWy-Co, SWy-Cu, and SWy-Ba samples via XRD modeling profile approach is summarized in Figure 11. The light brown, caramel, and dark brown colors represent the 0 W, 1 W, and 2 W layer type, respectively. Each line thus represents a layer with its intrinsic hydration state. The configuration considered here is an optimal configuration (best agreement obtained) extracted from the best agreements obtained between theoretical and experimental XRD profile. For SWy-Co complexes, the correlation between partial and total segregation stacking is observed. Thus, for SWy-Cu samples, we notice that the total segregation aspect is present regardless of the applied constraint applied. On the other hand, the SWy-Ba series shows the existence of two modes of stacking, segregation accompanied by partial order, with blatant dominance for segregated stacking.

3.8. BET and BJH Pore Size Distribution Analysis. The exploitation of the results obtained from the structural analysis by XRD modeling approach demonstrates a variability, in term of population, within the same crystallite. This directly influences the internal and external layers surfaces, which subsequently affects the adsorption properties and the sample porosity. Our objective is to evaluate the effect of the applied coupling disturbance (pH and T°C) on these properties. Indeed, we are looking for a link between structural damage, the intrinsic properties of the sample, and the saturation of the CEC. For that, a study based on BET adsorption measurement and BJH pore size distribution analysis is directed. Both the single-point and multipoint BET methods based on the surface area (SA) purpose from nitrogen isotherms were approved to evaluate external layer surface perturbation [41, 123–131] (Figure 12). Average pore diameter is determined using the BJH method (Figure 13). Whatever the nature of the exchangeable cation, an increase in the SA values is shown as a function of the constraint intensity up to a pH = 9 and a T = 80°C. After this limit value, a behavior divergence is shown. In fact, for the two samples saturated, respectively, by Co and Cu cations, a decrease in the SA values is observed against the continuous growth in the case of the Ba cation.

The average pore diameter evolution versus constraint strength (Figure 13) can provide a preliminary explanation for the observed SA fluctuations.

For all samples, the limit of mesoporosity domain is respected (where pores whose maximum diameter is

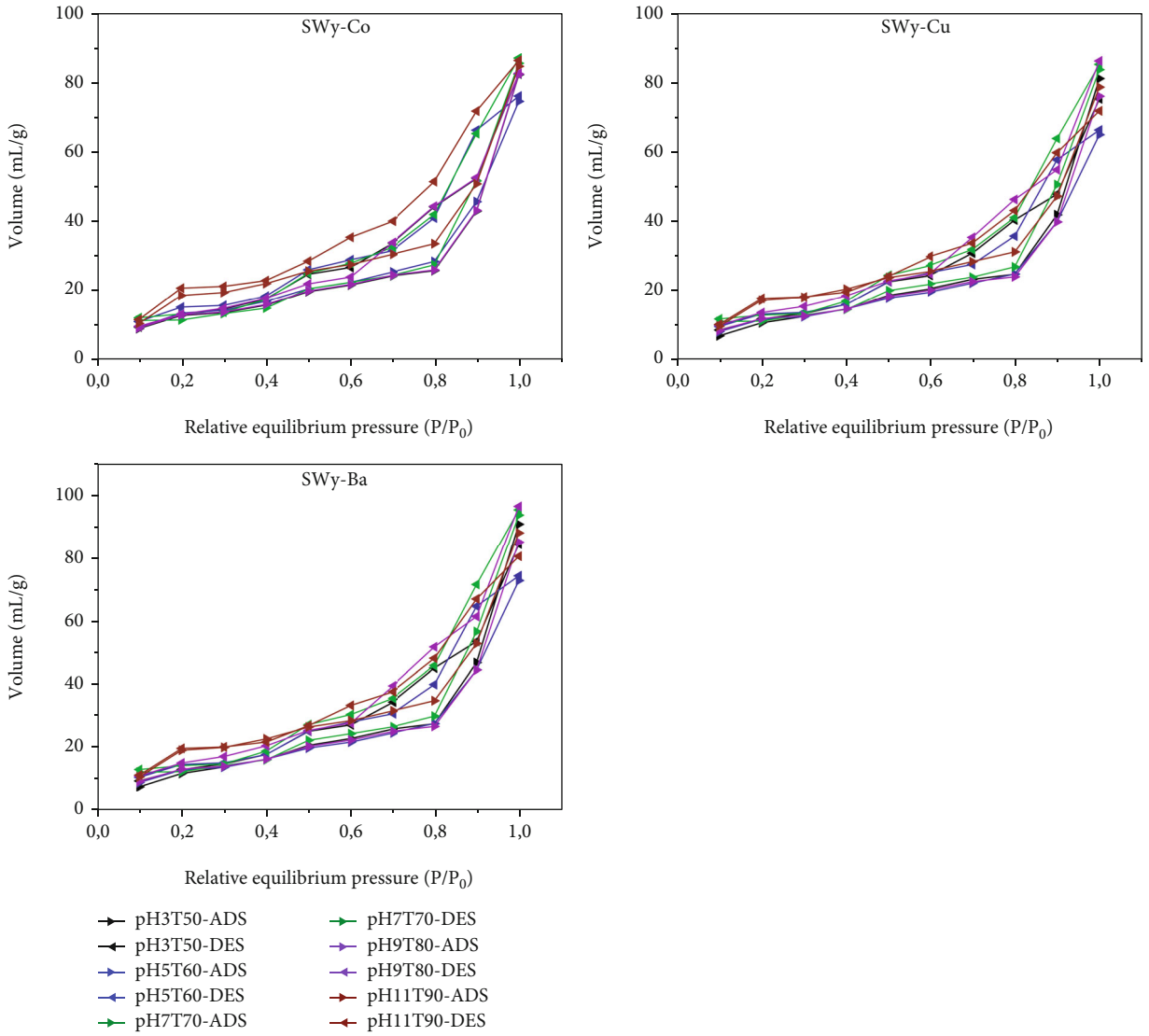

Figure 14: Nitrogen adsorption (ads)-desorption (des)-isotherms in the case of SWy-Co, SWy-Cu, and SWy-Ba.

between 2 and 50 nm). Indeed, the SWy-Ba sample practically keeps the same average pore diameters values up to pH = 11 and $T = 90°C$. However, the other two samples are marked by a considerable increase in the average pore diameter, which probably indicates a transformation that affected the internal configuration of the clay particle. This agrees with the results obtained from XRD analysis focusing the evolution of the average number of layers versus constraint strength.

Obtained nitrogen adsorption (ADS)-desorption (DES) isotherms curves shape (Figure 14) shows a very closer type II isotherm classification [127–131]. This allocation confirms the supremacy of the mesoporous texture despite the fluctuations observed and the nature of the exchangeable cation. The relative large pore size obtained in the case of stressed SWy-Ba sample is explained by the coupling of three essential parameters, respectively, the acidic or basic nature of the soil solution, the intrinsic hydration property, and the nature of the exchangeable cation. The Ba^{2+} ions exchange promotes the exfoliation process and thereafter increases the porosity degree.

To overcome the limits of SA analysis (i.e., nitrogen can only cover external surfaces and does not interact with internal surfaces), since it cannot access the information in the volume of the sample and subsequently, it does not provide information on the IS configurations/changes, a pore size distribution (PSD) analysis imposes itself. The application of PSD analysis requires technical approaches such as (i) the volumes of micropores, mesopores, and macropores including nanopores in one gram solid labeled, respectively, V_{Mi}, V_{Me}, and V_{Ma} (all in mL/g) and (ii) the effects related to macroporosity are neglected assuming that they do not affect the properties of adsorption and the specific micromesopore volumes ($V = V_{Mi} + V_{Me}$) that is determined using the desorption data (at the relative equilibrium pressure P/P_0). Fundamental approximations used for the PSD analysis target the shape and characteristics of the pores. Indeed, cylindrical shape (with radius (r) approximately half of its

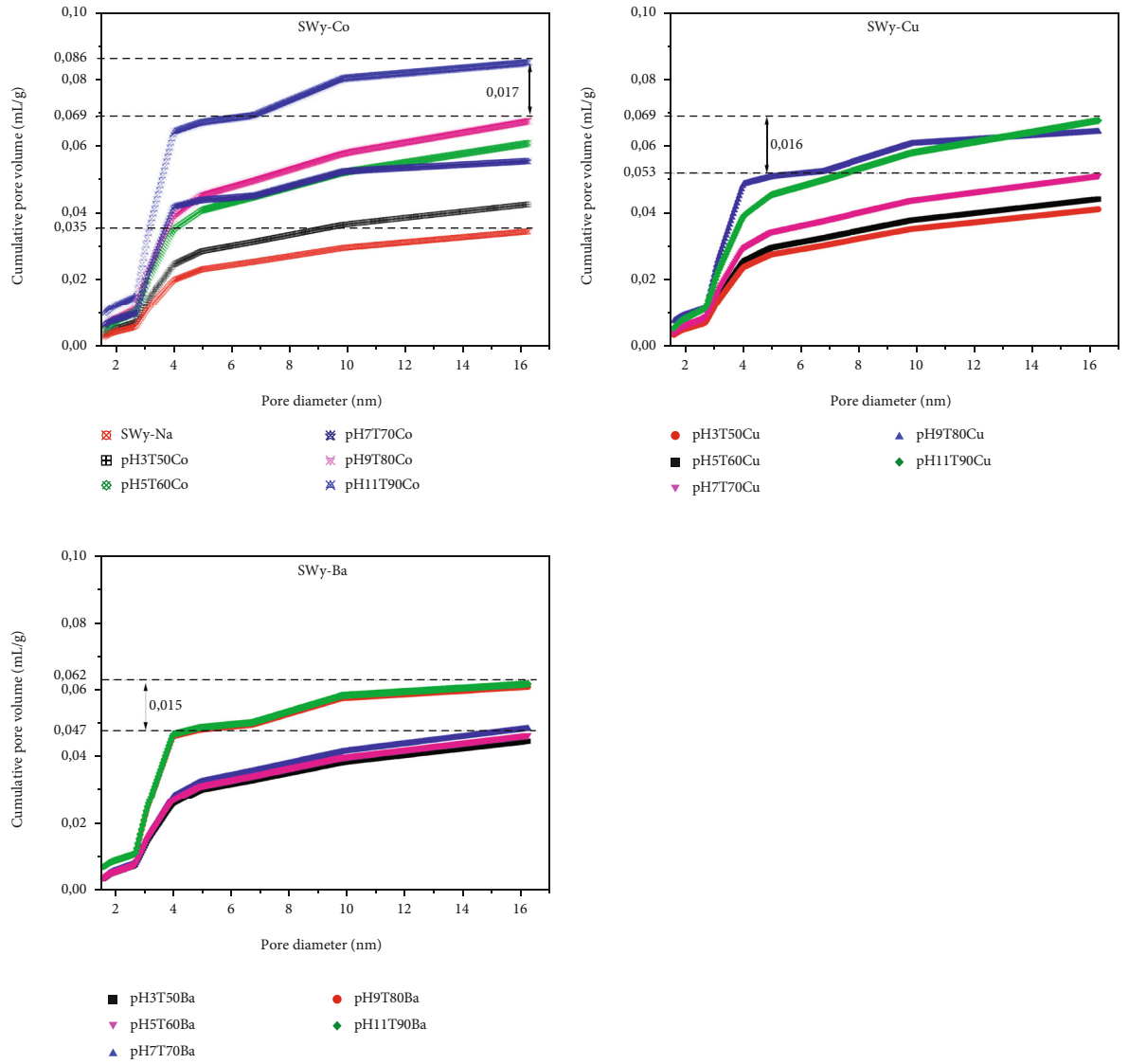

Figure 15: The pore size distribution (PSD) curve for the different studied samples (V-r) in the case of SWy-Co, SWy-Cu, and SWy-Ba.

width) is adopted. Also, cylindrical mesopores are characterized by r radii which correspond to V values (calculated from the corrected Kelvin equation using P/P_0 values).

The PSD plots provide information on the variation of the cumulative pore volume versus pore radius (V-r) (Figure 15). Although they have the same trend, the V-r curves relating to each sample present specificities showing the effect of the applied stress on the evolution of the porosity. In the case of SWy-Co sample and from a diameter of 4 nm, an evolution divergence appears with a "gap" in favor of high pH and T°C value which reaches 0.086 mL/g (Figure 15). The V-r variation divergence proves, initially, the achievement of the cation exchange process which is confirmed by an individual comportment of the V-r curves despite having the same appearance. In addition, a direct effect of the increase of the applied stresses appears as an increase in the V-r "gap." For SWy-Ba, the maximum cumulative pore volume is 0.062 mL/g attained at pH = 9 and T = 80°C. The major remark concerns the last two values of pH and T. Indeed, although they present a very similar appearance to the other V-r characteristic curves, there is a jump ("gap") of 0.015 mL/g attributed to the acid-base transformation. In the case of SWy-Cu, the V-r curves have respected the same shape as for the other samples, but the maximum value did not exceed 0.069 mL/g. The common behavior for the three samples lies in the existence of a cumulative pore volume "gap" observed during the acid-base transformation. The value of this gap is practically very similar and close for all samples, and it averages around 0.016 mL/g. This variation is consistent with the XRD modeling profile which predicts layer exfoliation and presence of highly hydrated rate.

The derivative pore size distribution curve (Figure 16) confirms the prevailing mesoporosity with a pore diameter concentration varying between 2.20 and 9.89 nm. A concentration of large pore populations related to the saturated

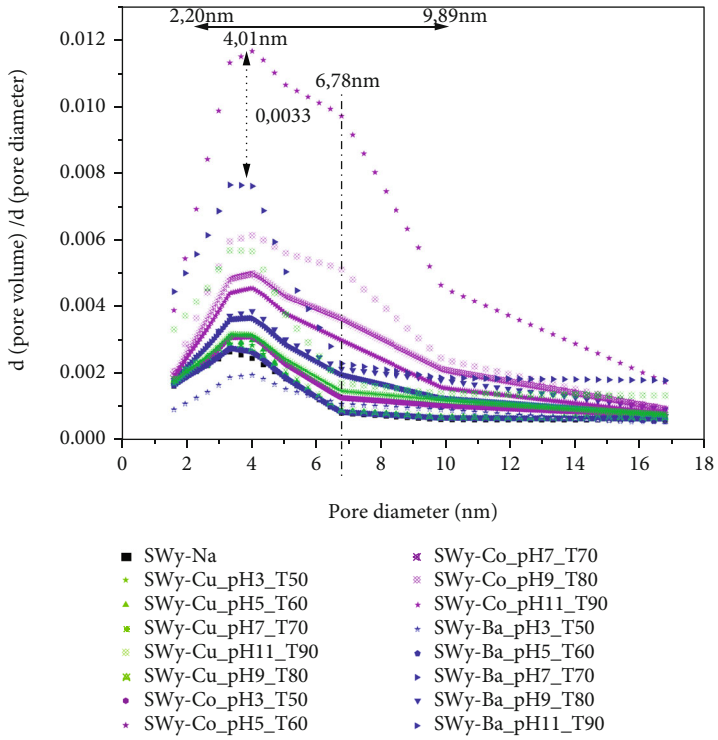

Figure 16: The derivative pore size distribution curve.

Co^{2+} sample (at pH = 11 and $T = 90°C$) is observed. This agrees with the obtained SA results and XRD analysis. The V-r curve radius derivative for all samples is given in Figure 16. For the rest of the studied samples, an almost similar variation is observed except for SWy-Ba (pH = 11/T = 90) which presents an extremum around 4.01 nm with a small extent.

4. Conclusion

This work studied the Wyoming montmorillonite response to a first-order coupling constraint obtained at the laboratory scale by combining soil solution pH variation with temperature gradient. The eventual mineral response to such disturbance was approached from a structural, hydrological (IS perturbation), cation exchange (CEC), and porosity point of view.

The quantitative investigation of the 001 reflections obtained from the XRD patterns via the modeling approach makes it possible to develop a deep theoretical calculation which allows us to build a global idea about the mechanisms accompanying these changes. Indeed, IS configuration and evolution are decrypted according to the applied constraint. Several parameters like nature, abundance, relative probability, size, position, arrangement of atoms/ions in the IS, the quantity of nH_2O, the average number of sheets, and the stacking modes in crystallites are precisely identified.

These goals are achieved by combining results from XRD profile modeling approach, TG/DTA analysis, and the adsorption measurement outcomes.

The starting SWy-Na complexes studied at room condition exhibit a heterogeneous hydration state characterized by a mixture between 0 W and 1 W phases contrary to the qualitative analysis which shows a homogeneous character. A correlation between XRD profile modeling approach consolidated by TG/DTA analysis and the adsorption measurement outcomes shows the following:

The case of the Co^{2+} cation is as follows:

(i) Heterogeneous hydration behavior induced by the coexistence of two type of layer populations (i.e., 1 W and 2 W phases within the crystallite), whatever the stress force

(ii) The theoretical decomposition of the experimental XRD profiles allowed us to identify all the different populations of existing layers and their stacking mode

(iii) A dominance of the segregated layer stacking mode

(iv) The CEC increases simultaneously with the applied stress intensity increases

(v) A linear regression approach describes the water molecule amount decrease, determined from TG/DTA analysis, as the temperature increases

(vi) The total structure change may appear ($2:1 \longrightarrow 1:1$) by exceeding the limit of the applied stress (pH 11 and $T > 150°C$)

(vii) The BJH method shows an increase on the porosity rate traduced by an evolution divergence appearing with a "gap" in favor of high pH and T°C value. The

pore diameter concentration is varying between 2.20 and 9.89 nm

The case of the Cu^{2+} cation is as follows:

(i) An interstratification explains the coexistence of two hydration states (1 W and 2 W) regardless of the stress strength

(ii) The coexistence within the crystallite of different types of layer populations stacked according to a specific set of junction probabilities

(iii) "Total segregation" stacking mode dominated the entire series

(iv) CEC growth by increasing the applied stress

(v) A nonlinear water molecules amount decrease unlike SWy-Co sample as a function of the increase in external applied stresses (from TG/DTA analysis) is fitted with a regression approach based on the Lorentz model

(vi) Adsorption outcomes demonstrate that the sample seems undamaged by the applied stress intensity fluctuations

The case of the Ba^{2+} cation is as follows:

(i) A heterogeneous hydration state proven by the presence of several layers 0 W, 1 W, and 2 W, regardless of the applied stress

(ii) The coexistence of several types of compensating cation (Ba^{2+} and Na^{+}) indicating the formation of a real physical mixture between populations of different layer types

(iii) Partial CEC saturation and domination of segregated layer stacking aspect

(iv) Results from TG/DTA analysis show a nonlinear evolution governed by a Lorentz function which lies between the observed evolution in the case of Co^{2+} and Cu^{2+} cations

(v) The intrinsic sample porosity is affected by the acid-base transformation with a 0.015 mL/g "gap." The maximum cumulative pore volume is 0.062 mL/g attained at pH = 9 and $T = 80°C$

In addition, the XRD modeling approach allowed us to assign a structural response of the water footprint of the samples and to map the interstratification of the different layer type populations.

The presence of each cation induces specific structural characteristics and a variable exchanged sample response to external excitation. The observed structural transition, for the Co^{2+} cation from a pH = 8 and $T = 80°$, accompanied by a concentration of large pore populations (at pH = 11 and $T = 90°C$) indicates the strong exfoliation phenomena affecting even the elementary tetrahedral or octahedral sheets and subsequently reducing the metal removal efficiency.

The evolution of the average number of layers (M) confirms the consolidation of the crystallite thickness in the case of Ba^{2+} cation despite the acid-base transition and the strong thermal gradient. This is in favor of an irreversible cation exchange process supporting the Barium removal efficiency.

Data Availability

No data were used to support this study.

Disclosure

The results presented are a part of the Ph.D. thesis of Chadha MEJRI (CM) realized at LR19ES20: Resources, Materials, and Ecosystems (RME), Faculty of Sciences of Bizerte, University of Carthage, 7021 Zarzouna, Tunisia, and supervised by Dr. Walid Oueslati (WO).

Conflicts of Interest

The authors declare no conflict of interest.

Authors' Contributions

Ph.D. Chadha MEJRI (CM) realized the experimental part, XRD profile modeling approach, and the draft paper writing. Dr. Walid Oueslati (WO) supervised the study, contributed to the experimental result acquisition and XRD profile modeling approach, realized the adsorption measurement, directed the (BJH) pore size distribution analyses, and contributed on the writing of the paper draft and the proof reading/revision of the manuscript.

Acknowledgments

CM acknowledges WO for the original idea of the work, the fruitful discussions about the XRD modeling approach, and the montmorillonite hydration behavior.

Supplementary Materials

Figure S1: results of thermogravimetry/differential thermal analysis (TG/DTA) for the samples SWy-Co, SWy-Cu, and SWy-Ba. Figure S2: scheme of the "Water Footprint" of SWy-Co, SWy-Cu, and SWy-Ba samples via X-ray diffraction modeling. The light brown, caramel, and dark brown colors represent the hydration states of the layers of type 0 W, 1 W, and 2 W, respectively, related to each phase. Figure S3: evolutions in the percentage of hydration layer types for samples SWy-Co, SWy-Cu, and SWy-Ba. *(Supplementary Materials)*

References

[1] G. Brown, "Crystal structures of clay minerals and their X-ray identification," *The Mineralogical Society of Great Britain and Ireland*, vol. 5, pp. 1–494, 1982.

[2] A. C. D. Newman, "Chemistry of clays and clay minerals," *Mineral Society Monograph, London*, vol. 6, pp. 1–480, 1987.

[3] N. Güven, "Hydrous phyllosilicates (exclusive of micas)," in *Reviews in Mineralogy*, S. W. Bailey, Ed., vol. 19, pp. 1–497, Walter de Gruyter GmbH & Co KG, 1988.

[4] W. F. Moll, "Baseline studies of the clay minerals society source clays: geological origin," *Clays and Clay Minerals*, vol. 49, no. 5, pp. 374–380, 2001.

[5] T. Sato, T. Watanabe, and R. Otsuka, "Effects of layer charge, charge location, and energy change on expansion properties of dioctahedral smectites," *Clays and Clay Minerals*, vol. 40, no. 1, pp. 103–113, 1992.

[6] I. Bérend, J. M. Cases, M. François et al., "Mechanism of adsorption and desorption of water vapor by homoionic montmorillonites: 2. The Li^+, Na^+, K^+, Rb^+, and Cs^+-exchanged forms," *Clays and Clay Minerals*, vol. 43, no. 3, pp. 324–336, 1995.

[7] J. M. Cases, I. Bérend, M. François, J. P. Uriot, L. J. Michot, and F. Thomas, "Mechanism of adsorption and desorption of water vapor by homoionic montmorillonite: 3. The Mg^{2+}, Ca2+, Sr^{2+} and Ba^{2+} exchanged forms," *Clays and Clay Minerals*, vol. 45, no. 1, pp. 8–22, 1997.

[8] I. Nistor and N. Miron, "Depollution of uranyl polluted waters using pillared clays," *Journal of Thermal Analysis and Calorimetry*, vol. 89, no. 3, pp. 977–981, 2007.

[9] I. Chaari, M. Medhioub, and F. Jamoussi, "Use of clay to remove heavy metals from Jebel Chakir landfill leachate," *Journal of Applied Sciences in Environmental Sanitation*, vol. 6, no. 2, pp. 143–148, 2011.

[10] L. N. F. de Queiroga, D. B. França, F. Rodrigues, I. M. G. Santos, M. G. Fonseca, and M. Jaber, "Functionalized bentonites for dye adsorption: Depollution and production of new pigments," *Journal of Environmental Chemical Engineering*, vol. 7, no. 5, article 103333, 2019.

[11] J. G. Mahy, M. H. Tsaffo Mbognou, C. Léonard, N. Fagel, E. D. Woumfo, and S. D. Lambert, "Natural clay modified with ZnO/TiO_2 to enhance pollutant removal from water," *Catalysts*, vol. 12, no. 2, pp. 148–148, 2022.

[12] M. L. Whittaker, L. N. Lammers, S. Carrero, B. Gilbert, and J. F. Banfield, "Ion exchange selectivity in clay is controlled by nanoscale chemical–mechanical coupling," *Proceedings of the National Academy of Sciences*, vol. 116, no. 44, pp. 22052–22057, 2019.

[13] G. Moldoveanu and V. Papangelakis, "Chelation-assisted ion-exchange leaching of rare earths from clay minerals," *Metals*, vol. 11, no. 8, pp. 1265–1279, 2021.

[14] S. T. Hussain and S. A. K. Ali, "Removal of heavy metal by ion exchange using bentonite clay," *Journal of Ecological Engineering*, vol. 22, no. 1, pp. 104–111, 2021.

[15] N. Subramanian and L. N. Lammers, "Thermodynamics of ion exchange coupled with swelling reactions in hydrated clay minerals," *Journal of Colloid and Interface Science*, vol. 608, pp. 692–701, 2022.

[16] H. S. D. C. Neves, T. L. da Silva, M. G. C. da Silva, R. Guirardello, and M. G. A. Vieira, "Ion exchange and adsorption of cadmium from aqueous media in sodium-modified expanded vermiculite," *Environmental Science and Pollution Research*, vol. 2022, pp. 1–17, 2022.

[17] J. L. Bobin, E. Huffer, and H. Nifenecker, "Le stockage des déchets nucléaires en site profond," in *L'énergie de demain: Techniques, environnement, économie*, pp. 429–448, Les Ulis: EDP Sciences, 2021.

[18] A. Usuki, N. Hasegawa, M. Kato, and S. Kobayashi, "Polymer-clay nanocomposites," *Inorganic Polymeric Nanocomposites and Membranes*, vol. 179, pp. 135–195, 2005.

[19] G. Choudalakis and A. D. Gotsis, "Permeability of polymer/clay nanocomposites: a review," *European Polymer Journal*, vol. 45, no. 4, pp. 967–984, 2009.

[20] M. Raji, M. E. M. Mekhzoum, D. Rodrigue, and R. Bouhfid, "Effect of silane functionalization on properties of polypropylene/clay nanocomposites," *Composites Part B: Engineering*, vol. 146, pp. 106–115, 2018.

[21] S. Murugesan and T. Scheibel, "Copolymer/clay nanocomposites for biomedical applications," *Advanced Functional Materials*, vol. 30, no. 17, pp. 1908101–1908129, 2020.

[22] B. Qu and Y. Luo, "A review on the preparation and characterization of chitosan-clay nanocomposite films and coatings for food packaging applications," *Carbohydrate Polymer Technologies and Applications*, vol. 2, pp. 100102–100112, 2021.

[23] Z. Ghorbani, N. Zamindar, S. Baghersad, S. Paidari, S. M. Jafari, and L. Khazdooz, "Evaluation of quality attributes of grated carrot packaged within polypropylene-clay nanocomposites," *Journal of Food Measurement and Characterization*, vol. 15, no. 4, pp. 3770–3781, 2021.

[24] M. R. Abass, E. H. El-Masry, and A. B. Ibrahim, "Preparation, characterization, and applications of polyacrylonitrile/ball clay nanocomposite synthesized by gamma radiation," *Environmental Geochemistry and Health*, vol. 43, no. 8, pp. 3169–3188, 2021.

[25] Y. Zhu, J. O. Iroh, R. Rajagopolan, A. Aykanat, and R. Vaia, "Optimizing the synthesis and thermal properties of conducting polymer–montmorillonite clay nanocomposites," *Energies*, vol. 15, no. 4, pp. 1218–1291, 2022.

[26] M. Razavi, N. Sadeghi, S. H. Jafari, H. A. Khonakdar, U. Wagenknecht, and A. Leuteritz, "Thermo-rheological probe of microstructural evolution and degradation pathway in the flame-retarded PP/EVA/NOR/clay nanocomposites," *Rheologica Acta*, vol. 61, no. 1, pp. 25–47, 2022.

[27] A. Teepakakorn, T. Hayakawa, and M. Ogawa, "Remarkable stability of dye in polymer-clay nanocomposite film," *Applied Clay Science*, vol. 218, article 106405, 2022.

[28] M. I. Carretero and M. Pozo, "Clay and non-clay minerals in the pharmaceutical and cosmetic industries part II. Active ingredients," *Applied Clay Science*, vol. 47, no. 3-4, pp. 171–181, 2010.

[29] A. Papadopoulos, K. Giouri, E. Tzamos, A. Filippidis, and S. Stoulos, "Natural radioactivity and trace element composition of natural clays used as cosmetic products in the Greek market," *Clay Minerals*, vol. 49, no. 1, pp. 53–62, 2014.

[30] A. Panchal, G. Fakhrullina, R. Fakhrullin, and Y. Lvov, "Self-assembly of clay nanotubes on hair surface for medical and cosmetic formulations," *Nanoscale*, vol. 10, no. 38, pp. 18205–18216, 2018.

[31] J. Gubitosa, V. Rizzi, P. Fini, and P. Cosma, "Hair care cosmetics: from traditional shampoo to solid clay and herbal shampoo, a review," *Cosmetics*, vol. 6, no. 1, pp. 13–29, 2019.

[32] C. D. S. F. Gomes and J. B. P. Silva, "Minerals and clay minerals in medical geology," *Applied Clay Science*, vol. 36, no. 1-3, pp. 4–21, 2007.

[33] M. I. Carretero and M. Pozo, "Clay and non-clay minerals in the pharmaceutical industry: part I. excipients and medical applications," *Applied Clay Science*, vol. 46, no. 1, pp. 73–80, 2009.

[34] M. Massaro, G. Lazzara, S. Milioto, R. Noto, and S. Riela, "Covalently modified halloysite clay nanotubes: synthesis, properties, biological and medical applications," *Journal of Materials Chemistry B*, vol. 5, no. 16, pp. 2867–2882, 2017.

[35] S. M. Mousavi, S. A. Hashemi, S. Salahi, M. Hosseini, A. M. Amani, and A. Babapoor, "Development of clay nanoparticles toward bio and medical applications," in *In Current Topics in the Utilization of Clay in Industrial and Medical Applications*, pp. 167–191, Intech Open, London, UK, 2018.

[36] L. B. Williams and S. E. Haydel, "Evaluation of the medicinal use of clay minerals as antibacterial agents," *International Geology Review*, vol. 52, no. 7-8, pp. 745–770, 2010.

[37] L. B. Williams, D. W. Metge, D. D. Eberl et al., "What makes a natural clay antibacterial?," *Environmental Science & Technology*, vol. 45, no. 8, pp. 3768–3773, 2011.

[38] K. D. Morrison, J. C. Underwood, D. W. Metge, D. D. Eberl, and L. B. Williams, "Mineralogical variables that control the antibacterial effectiveness of a natural clay deposit," *Environmental Geochemistry and Health*, vol. 36, no. 4, pp. 613–631, 2014.

[39] L. Zarate-Reyes, C. Lopez-Pacheco, A. Nieto-Camacho et al., "Antibacterial clay against gram-negative antibiotic resistant bacteria," *Journal of Hazardous Materials*, vol. 342, pp. 625–632, 2018.

[40] B. Dazas, E. Ferrage, A. Delville, and B. Lanson, "Interlayer structure model of tri-hydrated low-charge smectite by X-ray diffraction and Monte Carlo modeling in the grand canonical ensemble," *American Mineralogist*, vol. 99, no. 8-9, pp. 1724–1735, 2014.

[41] C. Mejri, W. Oueslati, and A. B. H. Amara, "How the solid/liquid ratio affects the cation exchange process and porosity in the case of dioctahedral smectite: structural analysis?," *Adsorption Science and Technology*, vol. 2021, pp. 1–24, 2021.

[42] V. A. Drits, C. Tchoubar, V. A. Drits, and C. Tchoubar, "Experimental Techniques Adapted to the Study of Microdivided Lamellar Systems," in *In X-Ray Diffraction by Disordered Lamellar Structures*, pp. 165–198, Springer, Berlin, Heidelberg, 1990.

[43] A. R. Mermut and A. F. Cano, "Baseline studies of the clay minerals society source clays: chemical analyses of major elements," *Clays and Clay Minerals*, vol. 49, no. 5, pp. 381–386, 2001.

[44] M. Segad, B. Jonsson, T. Åkesson, and B. Cabane, "Ca/Na montmorillonite: structure, forces and swelling properties," *Langmuir*, vol. 26, no. 8, pp. 5782–5790, 2010.

[45] K. Yotsuji, Y. Tachi, H. Sakuma, and K. Kawamura, "Effect of interlayer cations on montmorillonite swelling: comparison between molecular dynamic simulations and experiments," *Applied Clay Science*, vol. 204, article 106034, 2021.

[46] H. Yan and Z. Zhang, "Effect and mechanism of cation species on the gel properties of montmorillonite," *Colloids and Surfaces A: Physicochemical and Engineering Aspects*, vol. 611, article 125824, 2021.

[47] W. Oueslati, H. B. Rhaiem, and A. B. H. Amara, "XRD investigations of hydrated homoionic montmorillonite saturated by several heavy metal cations," *Desalination*, vol. 271, no. 1-3, pp. 139–149, 2011.

[48] W. Oueslati and M. Meftah, "Discretization of the water uptake process of Na-montmorillonite undergoing atmospheric stress: XRD modeling approach," *Advances in Materials Science and Engineering*, vol. 2018, 17 pages, 2018.

[49] B. Dazas, B. Lanson, J. Breu, J. L. Robert, M. Pelletier, and E. Ferrage, "Smectite fluorination and its impact on interlayer water content and structure: a way to fine tune the hydrophilicity of clay surfaces?," *Microporous and Mesoporous Materials*, vol. 181, pp. 233–247, 2013.

[50] S. Gu, X. Kang, L. Wang, E. Lichtfouse, and C. Wang, "Clay mineral adsorbents for heavy metal removal from wastewater: a review," *Environmental Chemistry Letters*, vol. 17, no. 2, pp. 629–654, 2019.

[51] B. O. Otunola and O. O. Ololade, "A review on the application of clay minerals as heavy metal adsorbents for remediation purposes," *Environmental Technology and Innovation*, vol. 18, article 100692, 2020.

[52] S. Yingying, Z. Baoqiang, and W. Yang, "Application of clay minerals in remediation of heavy metal pollution in soil," *EDP Sciences*, vol. 204, p. 01011, 2020.

[53] A. R. A. Usman, Y. Kuzyakov, and K. Stahr, "Effect of clay minerals on extractability of heavy metals and sewage sludge mineralization in soil," *Chemistry and Ecology*, vol. 20, no. 2, pp. 123–135, 2004.

[54] Y. Zhang, Y. Li, J. Li, L. Hu, and X. Zheng, "Enhanced removal of nitrate by a novel composite: nanoscale zero valent iron supported on pillared clay," *Chemical Engineering Journal*, vol. 171, no. 2, pp. 526–531, 2011.

[55] M. M. Wahba, B. F. Labib, K. H. M. Darwish, and M. A. Zaghloul, "Application of some clay minerals to eliminate the hazards of heavy metals in contaminated soils," in *15th International Conference on EnvironmentalScience And Technology*, Rhodes, Greece, 2017.

[56] G. D. Yuan, B. K. G. Theng, G. J. Churchman, and W. P. Gates, "Clays and clay minerals for pollution control," *In Developments in Clay Science, Elsevier*, vol. 5, pp. 587–644, 2013.

[57] P. Antoine, A. Marchiol, M. Brocandel, and Y. Gros, "Discovery of periglacial features (sand and composite-wedges) in the nuclear waste storage site of the Aube department (France)," *Comptes Rendus Geoscience*, vol. 337, no. 16, pp. 1462–1473, 2005.

[58] A. Dizier, *Caractérisation des effets de température dans la zone endommagée autour de tunnels de stockage de déchets nucléaires dans des roches argileuses[Doctoral dissertation]*, Université de Liège, Belgique, 2011.

[59] P. Landrein, G. Vigneron, J. Delay, P. Lebon, and M. Pagel, "Lithologie, hydrodynamisme et thermicité dans le système sédimentaire multicouche recoupé par les forages Andra de Montiers-sur-Saulx (Meuse)," *Bulletin de la Société géologique de France*, vol. 184, no. 6, pp. 519–543, 2013.

[60] P. M. Abadie, "La gestion des déchets radioactifs en France et dans le monde," *In Annales des Mines-Responsabilite et environnement, FFE*, vol. 97, no. 1, pp. 48–52, 2020.

[61] A. S. Anastácio, A. Aouad, P. Sellin, J. D. Fabris, F. Bergaya, and J. W. Stucki, "Characterization of a redox-modified clay mineral with respect to its suitability as a barrier in radioactive waste confinement," *Applied Clay Science*, vol. 39, no. 3-4, pp. 172–179, 2008.

[62] R. A. Schoonheydt, C. T. Johnston, M. F. Brigatti, and A. Mottana, "The surface properties of clay minerals," *EMU Notes Mineral*, vol. 11, no. 10, pp. 337–373, 2011.

[63] R. Pusch, S. Knutsson, L. Al-Taie, and M. Hatem, "Optimal ways of disposal of highly radioactive waste," *Natural Science*, vol. 4, no. 11, pp. 906–918, 2012.

[64] P. Sellin and O. X. Leupin, "The use of clay as an engineered barrier in radioactive-waste management–a review," *Clays and Clay Minerals*, vol. 61, no. 6, pp. 477–498, 2013.

[65] F. M. Huber, S. Heck, L. Truche et al., "Radionuclide desorption kinetics on synthetic Zn/Ni-labeled montmorillonite nanoparticles," *Geochimica et Cosmochimica Acta*, vol. 148, pp. 426–441, 2015.

[66] N. P. Laverov, S. V. Yudintsev, B. T. Kochkin, and V. I. Malkovsky, "The Russian strategy of using crystalline rock as a repository for nuclear waste," *Elements*, vol. 12, no. 4, pp. 253–256, 2016.

[67] C. A. Coles and R. N. Yong, "Aspects of kaolinite characterization and retention of Pb and cd," *Applied Clay Science*, vol. 22, no. 1-2, pp. 39–45, 2002.

[68] J. H. Potgieter, S. S. Potgieter-Vermaak, and P. D. Kalibantonga, "Heavy metals removal from solution by palygorskite clay," *Minerals Engineering*, vol. 19, no. 5, pp. 463–470, 2006.

[69] G. J. Churchman, W. P. Gates, B. K. G. Theng, and G. Yuan, "Chapter 11.1 clays and clay minerals for pollution control," *Developments in Clay Science*, vol. 1, pp. 625–675, 2006.

[70] D. Mohapatra, D. Mishra, G. R. Chaudhury, and R. P. Das, "Arsenic adsorption mechanism on clay minerals and its dependence on temperature," *Korean Journal of Chemical Engineering*, vol. 24, no. 3, pp. 426–430, 2007.

[71] R. Chalghaf, W. Oueslati, M. Ammar, H. B. Rhaiem, and A. B. H. Amara, "Effect of temperature and pH value on cation exchange performance of a natural clay for selective (Cu^{2+}, Co^{2+}) removal: equilibrium, sorption and kinetics," *Progress in Natural Science: Materials International*, vol. 23, no. 1, pp. 23–35, 2013.

[72] H. Es-Sahbany, M. Berradi, S. Nkhili et al., "Removal of heavy metals (nickel) contained in wastewater-models by the adsorption technique on natural clay," *Materials Today: Proceedings*, vol. 13, pp. 866–875, 2019.

[73] O. Vidal, A. Baldeyrou, D. Beaufort, B. Fritz, N. Geoffroy, and B. Lanson, "Experimental study of the stability and phase relations of clays at high temperature in a thermal gradient," *Clays and Clay Minerals*, vol. 60, no. 2, pp. 200–225, 2012.

[74] H. Yin and J. Zhu, "In situ remediation of metal contaminated lake sediment using naturally occurring, calcium-rich clay mineral-based low-cost amendment," *Chemical Engineering Journal*, vol. 285, pp. 112–120, 2016.

[75] D. E. Pufahl, D. G. Fredlund, and H. Rahardjo, "Lateral earth pressures in expansive clay soils," *Canadian Geotechnical Journal*, vol. 20, no. 2, pp. 228–241, 1983.

[76] I. Berend, "Les mécanismes d'hydratation de montmorillonites homoioniques pour des pressions relatives inferieures à 0.95, [Doctoral dissertation]," Institut National Polytechnique de Lorraine, 1991.

[77] W. Oueslati, M. S. Karmous, H. B. Rhaiem, B. Lanson, and A. B. H. Amara, "Effect of interlayer cation and relative humidity on the hydration properties of a dioctahedral smectite," *Zeitschrift für Kristallographie Supplements*, vol. 2007, supplement 26, pp. 417–422, 2007.

[78] W. Oueslati, H. B. Rhaiem, and A. B. H. Amara, "Effect of relative humidity constraint on the metal exchanged montmorillonite performance: an XRD profile modeling approach," *Applied Surface Science*, vol. 261, pp. 396–404, 2012.

[79] M. Ammar, W. Oueslati, N. Chorfi, and H. Ben Rhaiem, "Interlamellar space configuration under variable environmental conditions in the case of Ni-exchanged montmorillonite: quantitative XRD analysis," *Journal of Nanomaterials*, vol. 2014, 13 pages, 2014.

[80] W. Oueslati, N. Chorfi, and M. Abdelwahed, "Effect of mechanical constraint on the hydration properties of Na-montmorillonite: study under extreme relative humidity conditions," *Powder Diffraction*, vol. 32, no. S1, pp. S160–S167, 2017.

[81] W. Oueslati, "Effect of soil solution pH during the tetracycline intercalation on the structural properties of a dioctahedral smectite: microstructural analysis," *Journal of Nanomaterials*, vol. 2019, 17 pages, 2019.

[82] W. Oueslati, H. Ben Rhaiem, M. S. Karmous, S. Naaman, and A. B. H. Amara, "Study of the structural evolution and selectivity of Wyoming montmorillonite in relation with the concentration of Cu^{2+} and Ni^{2+}," *Zeitschrift für Kristallographie Supplement*, vol. 2006, supplement_23, pp. 425–429, 2006.

[83] M. S. Karmous, H. B. Rhaiem, J. L. Robert, B. Lanson, and A. B. H. Amara, "Charge location effect on the hydration properties of synthetic saponite and hectorite saturated by Na^{+}, Ca^{2+} cations: XRD investigation," *Applied Clay Science*, vol. 46, no. 1, pp. 43–50, 2009.

[84] M. Meftah, W. Oueslati, and A. B. H. Amara, "Synthesis of zeolites A and P from 1: 1 and HS from 2: 1 clays," *2nd International Conference on Materials Physics and Applications (JIPMA 2009/MATERIAUX 2009)*, vol. 13, 2010no. 1, Article ID 12019, 2010IOP Publishing, Gafsa, Tunisia, 2010.

[85] N. C. Marty, S. Grangeon, A. Lassin, B. Madé, P. Blanc, and B. Lanson, "A quantitative and mechanistic model for the coupling between chemistry and clay hydration," *Geochimica et Cosmochimica Acta*, vol. 283, pp. 124–135, 2020.

[86] V. Chantawong, N. W. Harvey, and V. N. Bashkin, "Comparison of heavy metal adsorptions by Thai kaolin and ballclay," *Water, Air, and Soil Pollution*, vol. 148, no. 1/4, pp. 111–125, 2003.

[87] A. Alshameri, H. He, C. Xin et al., "Understanding the role of natural clay minerals as effective adsorbents and alternative source of rare earth elements: adsorption operative parameters," *Hydrometallurgy*, vol. 185, pp. 149–161, 2019.

[88] D. M. K. Manohar, A. Krishnan, and T. S. Anirudhan, "Removal of mercury (II) from aqueous solutions and chlor-alkali industry wastewater using 2-mercaptobenzimidazole-clay," *Water Research*, vol. 36, no. 6, pp. 1609–1619, 2002.

[89] W. Zhang, Y. An, S. Li et al., "Enhanced heavy metal removal from an aqueous environment using an eco- friendly and sustainable adsorbent," *Scientific Reports*, vol. 10, no. 1, pp. 1–19, 2020.

[90] C. Zhang, L. Liu, Y. Dai, K. Zhu, Z. Liu, and H. Jia, "Molecular dynamics simulations of exchange behavior of radionuclides into montmorillonite: unraveling the dynamic processes and microscopic structures," *Applied Clay Science*, vol. 226, article 106579, 2022.

[91] L. Liu, C. Zhang, W. Jiang, X. Li, Y. Dai, and H. Jia, "Understanding the sorption behaviors of heavy metal ions in the interlayer and nanopore of montmorillonite: a molecular dynamics study," *Journal of Hazardous Materials*, vol. 416, article 125976, 2021.

[92] C. Zhang, X. Liu, R. M. Tinnacher, and C. Tournassat, "Mechanistic understanding of uranyl ion complexation on

montmorillonite edges: a combined first-principles molecular dynamics–surface complexation modeling approach," *Environmental Science and Technology*, vol. 52, no. 15, pp. 8501–8509, 2018.

[93] R. Hånde, V. Ramothe, S. Tesson et al., "Classical polarizable force field to study hydrated hectorite: optimization on DFT calculations and validation against XRD data," *Minerals*, vol. 8, no. 5, pp. 205–2021, 2018.

[94] E. Scholtzová and D. Tunega, "Density functional theory study of the stability of the tetrabutylphosphonium and tetrabutylammonium montmorillonites," *Clay Minerals*, vol. 54, no. 1, pp. 41–48, 2019.

[95] T. Ohkubo, T. Okamoto, K. Kawamura et al., "New insights into the Cs adsorption on montmorillonite clay from133Cs solid-state NMR and density functional theory calculations," *The Journal of Physical Chemistry A*, vol. 122, no. 48, pp. 9326–9337, 2018.

[96] C. Bataillon, C. Musy, and M. Roy, "Corrosion des surconteneurs de déchets, cas d'un surconteneur en acier faiblement allié," *Le Journal de Physique IV*, vol. 11, no. 1, pp. Pr1-267–Pr1-274, 2001.

[97] W. Oueslati, M. Ammar, and N. Chorfi, "Quantitative XRD analysis of the structural changes of Ba-exchanged montmorillonite: effect of an in situ hydrous perturbation," *Minerals*, vol. 5, no. 3, pp. 507–526, 2015.

[98] S. W. Bailey, "Structures of layer silicates," *Crystal Structures of Clay Minerals and their X-Ray Identification*, vol. 5, 1980.

[99] J. Ben Brahim, G. Besson, and C. Tchoubar, "Etude des profils des bandes de diffraction X d'une beidellite-Na hydratée à deux couches d'eau. Détermination du mode d'empilement des feuillets et des sites occupés par l'eau," *Journal of Applied Crystallography*, vol. 17, no. 3, pp. 179–188, 1984.

[100] B. A. Sakharov and B. Lanson, "X-ray identification of mixed-layer structures: modelling of diffraction effects," *In Developments in Clay Science, Elsevier*, vol. 5, pp. 51–135, 2013.

[101] E. Ferrage, B. Lanson, B. A. Sakharov, and V. A. Drits, "Investigation of smectite hydration properties by modeling experimental X-ray diffraction patterns: part I. Montmorillonite hydration properties," *American Mineralogist*, vol. 90, no. 8-9, pp. 1358–1374, 2005.

[102] B. Lanson, "Modelling of X-ray diffraction profiles," *EMU Notes in Mineralogy*, vol. 11, no. 4, pp. 151–202, 2011.

[103] B. A. Sakharov and V. A. Drits, "Mixed-layer kaolinite-montmorillonite: a comparison of observed and calculated diffraction patterns," *Clays and Clay Minerals*, vol. 21, no. 1, pp. 15–17, 1973.

[104] A. B. H. Amara, "X-ray diffraction, infrared and TGA/DTG analysis of hydrated nacrite," *Clay Minerals*, vol. 32, no. 3, pp. 463–470, 1997.

[105] A. U. Dogan, M. Dogan, M. Onal, Y. Sarikaya, A. Aburub, and D. E. Wurster, "Baseline studies of the clay minerals society source clays: specific surface area by the Brunauer Emmett Teller (BET) method," *Clays and Clay Minerals*, vol. 54, no. 1, pp. 62–66, 2006.

[106] C. D. Hatch, J. S. Wiese, C. C. Crane, K. J. Harris, H. G. Kloss, and J. Baltrusaitis, "Water adsorption on clay minerals as a function of relative humidity: application of BET and Freundlich adsorption models," *Langmuir*, vol. 28, no. 3, pp. 1790–1803, 2012.

[107] T. Kozaki, T. Sawaguchi, A. Fujishima, and S. Sato, "Effect of exchangeable cations on apparent diffusion of Ca^{2+} ions in Na- and Ca-montmorillonite mixtures," *Physics and Chemistry of the Earth, Parts A/B/C*, vol. 35, no. 6-8, pp. 254–258, 2010.

[108] S. Babel and T. A. Kurniawan, "Low-cost adsorbents for heavy metals uptake from contaminated water: a review," *Journal of Hazardous Materials*, vol. 97, no. 1-3, pp. 219–243, 2003.

[109] F. Bergaya and G. Lagaly, "Chapter 1 general introduction: clays, clay minerals, and clay science," *Developments in Clay Science*, vol. 1, pp. 1–18, 2006.

[110] R. D. Shannon, "Revised effective ionic radii and systematic studies of interatomic distances in halides and chalcogenides," *Acta Cryst*, vol. 32, no. 5, pp. 751–767, 1976.

[111] E. Ferrage, C. A. Kirk, G. Cressey, and J. Cuadros, "Dehydration of ca-montmorillonite at the crystal scale. Part I: structure evolution," *American Mineralogist*, vol. 92, no. 7, pp. 994–1006, 2007.

[112] E. Ferrage, C. A. Kirk, G. Cressey, and J. Cuadros, "Dehydration of ca-montmorillonite at the crystal scale. Part 2. Mechanisms and kinetics," *American Mineralogist*, vol. 92, no. 7, pp. 1007–1017, 2007.

[113] R. Chalghaf, W. Oueslati, M. Ammar, H. B. Rhaiem, and A. B. H. Amara, "Effect of an "in situ" hydrous strain on the ionic exchange process of dioctahedral smectite: case of solution containing (Cu^{2+}, Co^{2+}) cations," *Applied Surface Science*, vol. 258, no. 22, pp. 9032–9040, 2012.

[114] M. Meftah, W. Oueslati, N. Chorfi, and A. B. H. Amara, "Intrinsic parameters involved in the synthesis of metakaolin based geopolymer: microstructure analysis," *Journal of Alloys and Compounds*, vol. 688, pp. 946–956, 2016.

[115] M. Meftah, W. Oueslati, N. Chorfi, and A. B. H. Amara, "Effect of the raw material type and the reaction time on the synthesis of halloysite based zeolite Na-P1," *Results in Physics*, vol. 7, pp. 1475–1484, 2017.

[116] S. Caillère, S. Hénin, and M. Rautureau, "Minéralogie des argiles," *Classification et Nomenclature*, vol. 1982, no. 8, p. 184, 1982.

[117] G. W. Brindley, "Ethylene glycol and glycerol complexes of smectites and vermiculites," *Clay Minerals*, vol. 6, no. 4, pp. 237–259, 1966.

[118] R. C. Mackenzie, "The classification of soil silicates and oxides," *In Soil Components. Springer*, vol. 2, pp. 1–25, 1975.

[119] G. Pédro, *Les minéraux argileux dans Pédologie (2-Constituants et propriétés du sol)*, Eds. Duchaufour Ph. et Southier B, 1994.

[120] P. Komadel, J. Bujdák, J. Madejová, V. Šucha, and F. Elsass, "Effect of non-swelling layers on the dissolution of reduced-charge montmorillonite in hydrochloric acid," *Clay Minerals*, vol. 31, no. 3, pp. 333–345, 1996.

[121] F. B. K. G. Bergaya and G. Lagaly, "General introduction: clays, clay minerals, and clay science," *In Developments in Clay Science, Elsevier*, vol. 5, pp. 1–19, 2013.

[122] L. Sun, J. T. Hirvi, T. Schatz, S. Kasa, and T. A. Pakkanen, "Estimation of montmorillonite swelling pressure: A molecular dynamics approach," *The Journal of Physical Chemistry C*, vol. 119, no. 34, pp. 19863–19868, 2015.

[123] S. J. Gregg, K. S. W. Sing, and H. W. Salzberg, "Adsorption surface area and porosity," *Journal of the Electrochemical Society*, vol. 114, no. 11, p. 279C, 1967.

[124] L. Yu, W. L. Hsu, J. A. Shamim, and H. Daiguji, "Pore network modeling of a solid desiccant for dehumidification

applications," *International Journal of Heat and Mass Transfer*, vol. 186, article 122456, 2022.

[125] P. Pang, H. Han, L. Hu, C. Guo, Y. Gao, and Y. Xie, "The calculations of pore structure parameters from gas adsorption experiments of shales: which models are better?," *Journal of Natural Gas Science and Engineering*, vol. 94, article 104060, 2021.

[126] J. C. Groen, L. A. Peffer, and J. A. Moulijn, "Pore size determination in modified micro- and mesoporous materials. Pitfalls and limitations in gas adsorption data analysis," *Microporous and Mesoporous Materials*, vol. 60, no. 1-3, pp. 1–17, 2003.

[127] E. P. Barrett, L. G. Joyner, and P. P. Halenda, "The determination of pore volume and area distributions in porous substances. I. Computations from nitrogen isotherms," *Journal of the American Chemical Society*, vol. 73, no. 1, pp. 373–380, 1951.

[128] T. Liu, L. Ju, Y. Zhou et al., "Effect of pore size distribution (PSD) of Ni- Mo/Al_2O_3 catalysts on the Saudi Arabia vacuum residuum hydrodemetallization (HDM)," *Catalysis Today*, vol. 271, pp. 179–187, 2016.

[129] K. Sing, "The use of nitrogen adsorption for the characterisation of porous materials," *Colloids and Surfaces A: Physicochemical and Engineering Aspects*, vol. 187, pp. 3–9, 2001.

[130] P. Kumar, R. V. Jasra, and T. S. Bhat, "Evolution of porosity and surface acidity in montmorillonite clay on acid activation," *Industrial and Engineering Chemistry Research*, vol. 34, no. 4, pp. 1440–1448, 1995.

[131] J. M. Zielinski and L. Kettle, "Physical characterization: surface area and porosity," *London: Intertek*, vol. 23, p. 724, 2013.

Hindawi
Adsorption Science & Technology
Volume 2022, Article ID 7747152, 11 pages
https://doi.org/10.1155/2022/7747152

Research Article

Iminodisuccinic Acid Relieved Cadmium Stress in Rapeseed Leaf by Affecting Cadmium Distribution and Cadmium Chelation with Pectin

Hui Tian,[1,2] Zihan Zhu,[1] Haixing Song,[2] and Xiuwen Wu[1]

[1]*College of Resources and Environmental Sciences, Qingdao Agricultural University, Qingdao, China*
[2]*College of Resources and Environmental Sciences, Hunan Agricultural University, Changsha, China*

Correspondence should be addressed to Xiuwen Wu; wuxiuwen0605@163.com

Received 16 March 2022; Revised 22 April 2022; Accepted 8 May 2022; Published 13 June 2022

Academic Editor: Qiaohui Fan

Rapeseed (*Brassica napus* L.) is a nutritious vegetable, while cadmium (Cd) pollution threatens the growth, productivity, and food security of rapeseed. By studying the effects of iminodisuccinic acid (IDS), an easily biodegradable and environmental friendly chelating agent, on Cd distribution at the organ and cellular level, we found IDS promoted dry matter accumulation of rapeseed and increased the contents of photosynthetic pigment in leaves. Inhibited root-shoot Cd transport resulted in higher activity of antioxidant enzymes and decreased hydrogen peroxide (H_2O_2) and malondialdehyde (MDA) accumulation in leaves, which indicated that IDS contributed to alleviating Cd-caused oxidative damage in leaf cells. Additionally, IDS increased Cd subcellular distribution in cell wall (CW), especially in covalently bound pectin (CSP), and relieved Cd toxicity in organelle of leaves. IDS also enhanced demethylation of CSP. The Cd content in CSP, demethylation degree, and pectin methylesterase activity of CSP increased by 37.95%, 13.34%, and 13.16%, respectively, while IDS did not change the contents of different CW components. The improved Cd fixation in leaf CW was mainly attributed to enhance demethylation of covalently bound pectin (CSP) and Cd chelation with CSP.

1. Introduction

Excessive cadmium (Cd) in soil has remarkably affected the annual output of agricultural products due to reducing the production and quality of crops and vegetables [1, 2] which ultimately threatens food security [3, 4]. There are various methods of Cd-contaminated soil remediation, such as inoculation of soil with cadmium-resistant bacterium or biochar-supported microbial cell composite ([5, 6]), combined application of lime and organic matter [7], and phytoremediation of hyperaccumulation [8–10]. Cd absorbed by roots is easily transported to shoots due to its high mobility in plants [11, 12]. Rapeseed (*Brassica napus*) is not only a widespread oil crop [13], but also a popular nutritious vegetable. It is essential to reduce Cd content in the edible part of rapeseed to ensure food safety and enhance plant Cd resistance, which is also an effective strategy to improve rapeseed growth and production [14].

It has been verified extensively in many studies that the subcellular distribution of Cd is critical to Cd resistance in plants [15, 16], and cell wall (CW) as the first barrier can efficiently prevent Cd from entering cells [17–19]. In plants, most of the Cd^{2+} exists in CW [20, 21] by chelating with different CW components (pectin, cellulose, and hemicellulose) [22]. The CW immobilization of Cd, mainly due to chelating with pectin and carboxyl groups (COO-), arises from the demethylation of pectin by the catalysis of pectin methylesterase (PME) [9, 22].

Iminodisuccinic acid (IDS) is synthesized from maleic anhydride, ammonia, and sodium hydroxide. It is regarded as a kind of "green" chelating agent with low toxicity and fast degradation [23]. Previous researches have indicated the effects of some chelating agents, such as ethylenediamine tetraacetic acid (EDTA) [24, 25] and polyaspartic acid (PASP) on plant resistance to Cd [26]. Jing and Wang [27] also reported the stabilizing effect of IDS on metal ions.

Although there is ample evidence that IDS increases the aboveground biomass and decreases Cd accumulation in leaves of plants [28], however, few researchers studied the physiological responses of plants to Cd by IDS application, especially the effects on subcellular Cd distribution and CW components. Therefore, our experiment was set up to (a) study the Cd uptake and transportation in rapeseed by IDS application; (b) investigate how IDS affects the Cd resistance, subcellular Cd reallocation, and Cd chelation with different CW components; and (c) ultimately reveal the internal regulation mechanism underlying IDS improving Cd resistance in leaves of rapeseed.

2. Material and Methods

2.1. Experimental Arrangement and Growth Condition. A pot cultural experiment was set up in a glass greenhouse at Qingdao Agricultural University. The lightly Cd-contaminated soil with pH = 5.58 and total Cd content = 1.24 mg/kg was used in this experiment. The content of organic matter, total nitrogen (N), total phosphorus (P), and total potassium (K) in soil was 34.68, 1.90, 1.29, and 243.42 g/kg soil, respectively. To begin, 0.50 g urea, 0.82 g $Ca(H_2PO_4)2H_2O$, 0.26 g KCl, and 0.10 g H_3BO_3 were mixed thoroughly with 2 kg of soil before being filled into the pot. We set up two different treatments: conventional fertilizer treatment (CK) and conventional fertilizer +0.3% IDS (IDS). Each treatment contained five replicates (five pots), and each pot cultured two rapeseed seedlings. IDS is purchased from Hebei Wozi Environmental Protection Technology Co., Ltd, and the purity of IDS was more than 60%, and the molar mass was 337.1 Da. Fifteen days after *Brassica napus* L. seed germination, uniform seedlings were chosen and transplanted to pots of different treatments and then were cultured in a solar greenhouse for 45 days. All seedlings were randomly arranged to guarantee the condition's uniformity. During the experiment, the field capacity of about 80% was maintained by daily weighing each pot and evaluating water loss.

2.2. Analysis of Plant Dry Matter and Cd Concentration in Plants. After the rapeseed roots and leaves were separated and dried in an oven to constant weight at 75°C, their dry weights were measured and noted. Dried samples were ground to fine powder with a mortar and weighed, and then, all root powder and 0.10 g leaf powder were, respectively, digested in 5 ml concentrated nitric acid (HNO_3) in water bath kettle at 100°C for 2 h. The Cd concentration in the leaves and roots was then measured using inductively coupled plasma mass spectrometry (ICP-MS; PerkinElmer, MA, USA).

2.3. Quantification of Leaf Photosynthetic Pigment. The photosynthetic pigments (including chlorophyll a, b, and carotenoid) of fresh leaves were extracted with 95% ethanol and quantified based on the method of Wu et al. [2]. After extracting for 24 h under the condition of darkness at 25°C, the absorbance was determined by a spectrophotometer (HitachiUV-3100 UV/VIS; TECHCOMP, Shanghai, China) at the wavelengths of 665, 649, and 470 nm. The contents of chlorophyll a, chlorophyll b, and carotenoids were calculated according to corresponding absorbance values and following formulae:

$$\begin{aligned}
\text{chlorophyll a}\,(\text{mg/L}) &= 13.95A_{665} - 6.88A_{649};\\
\text{chlorophyll b}\,(\text{mg/L}) &= 24.96A_{649} - 7.32A_{665};\\
\text{carotenoid}\,(\text{mg/L}) &= (1000A_{470} - 2.05\text{Ca} - 114.8\text{Cb})/245.
\end{aligned} \tag{1}$$

2.4. Measurement of Reactive Oxygen Species (ROS), Antioxidant Enzymes, and Malondialdehyde (MDA) Contents. The superoxide anion ($O_2^{\cdot-}$) and hydrogen peroxide (H_2O_2) were extracted from fresh leaves and determined by spectrophotometry (HitachiUV-3100 UV/VIS; TECHCOMP, Shanghai, China) according to Liu and Liu [29]. The activity of superoxide dismutase (SOD), peroxidase (POD), catalase (CAT), and MDA content in leaves was quantified using the methods of Giannopolitis and Ries [30], Reff [31], De Azevedo Neto et al. [32], and Buege and Aust [33], respectively.

2.5. Determination of Cd Contents in Subcellular Components and Different CW Fraction. First, the leaf was processed into three subcellular components (CWs, organelles, and soluble fractions) according to Rathore [34] and Weigel and Jager [35], and then, CWs were further separated into several components: covalently bound pectin (CSP), ion-bound pectin (ISP), cellulose, and hemicellulose based on the method of Hu and Brown [36]. Then, the content of different CW component was measured by corresponding kits (Komin Biotechnology Co., Ltd., Suzhou, China). The Cd contents in the leaf subcellular components and different CW component were quantified by the ICP-MS (PerkinElmer, MA, USA).

2.6. Determination of the Pectin Methylation Degree (DM) and Pectin Methylesterase (PME) Activity. The degree of methylation of the ISP and CSP was determined based on the method of Anthon and Barrett [37]. Briefly, after the solution of pectin extract and NaOH was incubated at 25°C for 0.5 h, the H_2SO_4, Tris-HCl, MBTH, and alcohol oxidase (AO) were added in order. Then, the mixture was incubated at 30°C for 20 min, and ammonium ferric sulfate and sulfaminic acid solution were immediately added to terminate the reaction. Finally, the absorbance of the solution was measured by a spectrophotometer (HitachiUV-3100 UV/VIS; TECHCOMP, Shanghai, China) at the wavelength of 620 nm. The DM was calculated as the demethylation degree = 100 − DM.

The PME activity of fresh leaves was measured using the available commercial kit (PME-2-G, Suzhou Comin Biotechnology Co., Ltd.).

2.7. Data Statistical Analysis. The Student *t* test was applied to data with the Statistical Package for Social Sciences (SPSS ver. 19.0, SPSS Inc.). Different lowercase letters (a, b) indicated significant difference between CK and IDS treatments at the $P < 0.05$ level.

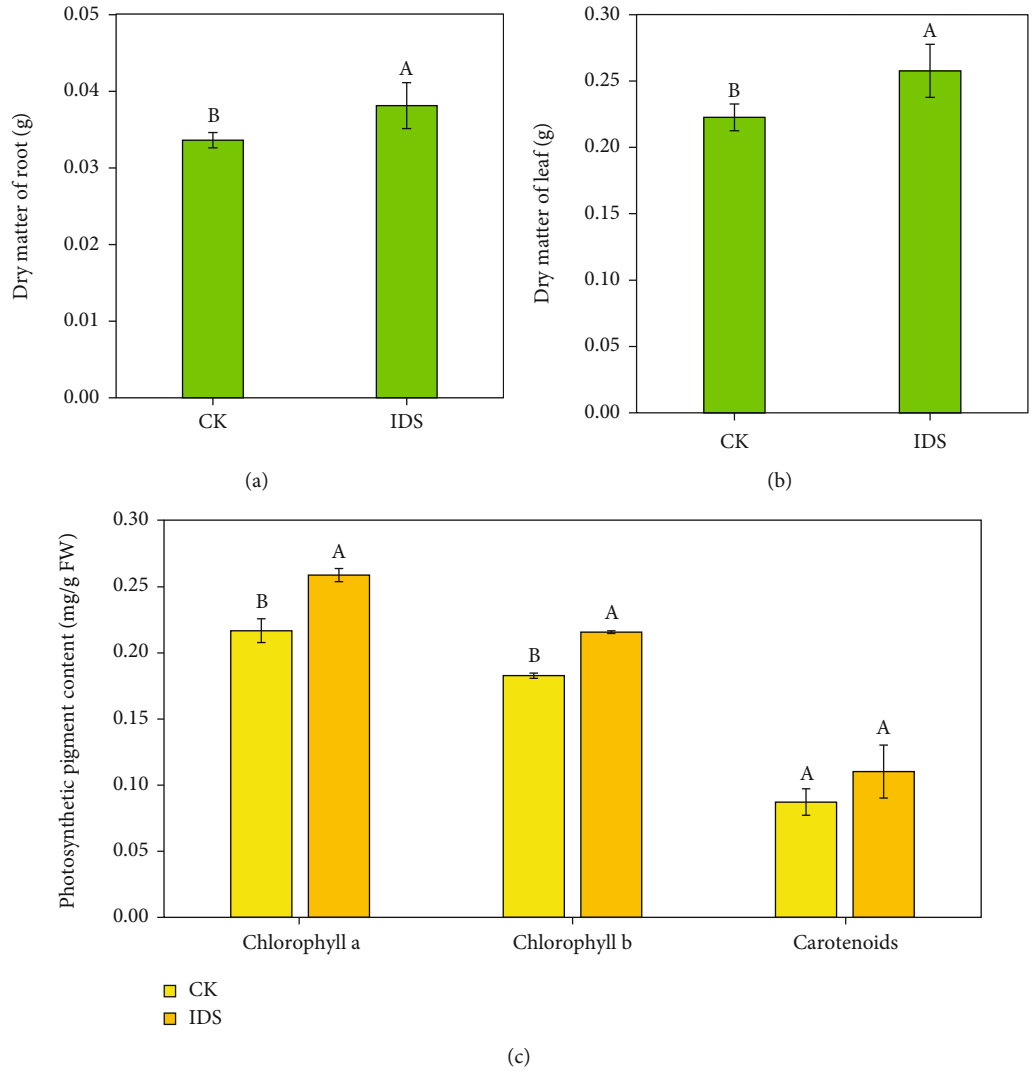

Figure 1: The effects of IDS on dry mass and pigment content in rapeseed under Cd stress. Mean ± SD ($n = 5$). Different uppercase letters (A, B) indicate significant difference between CK and IDS treatment at $P < 0.05$.

Table 1: The effects of IDS on Cd concentration and distribution in rapeseed seedlings. Mean ± SD ($n = 5$). Different capital letter indicates significant difference between these two treatments at $P < 0.05$ level.

Treatment	Cd concentration (μg/g)		Cd accumulation (μg/plant)		Cd distribution (%)		Cd transfer coefficient (%)
	Leaf	Root	Leaf	Root	Leaf	Root	
CK	4.5 ± 0.2A	13.6 ± 0.8A	1.0 ± 0.1A	0.5 ± 0.0A	68.3 ± 2.3A	31.7 ± 1.2B	33.5 ± 2.0A
IDS	3.1 ± 0.1B	14.3 ± 0.4A	0.8 ± 0.1B	0.5 ± 0.0A	59.8 ± 1.9B	40.2 ± 3.1A	21.9 ± 0.9B

Note: Cd transfer coefficient% = Cd concentration in leaves/Cd concentration in roots × 100.

3. Results

3.1. IDS Increased Plant Dry Mass and Photosynthetic Pigment Contents. The results shown in Figure 1(a) and Figure 1(b) suggest that IDS application significantly increased the dry mass of rapeseed roots and leaves, indicating that IDS promoted the growth of rapeseed under Cd stress. In the meantime, our study found increased photosynthetic pigment contents, especially chlorophyll a and chlorophyll b ($P < 0.05$) in rapeseed leaves of IDS treatment (Figure 1(c)).

3.2. IDS Decreased Cd Accumulation and Transportation in Rapeseed Leaves. To identify the effects of IDS on Cd in rapeseed seedlings, we quantified Cd concentration and calculated Cd accumulation in roots and leaves, Cd distribution, and Cd transfer coefficient. Table 1 suggests that IDS application did not affect Cd concentration and

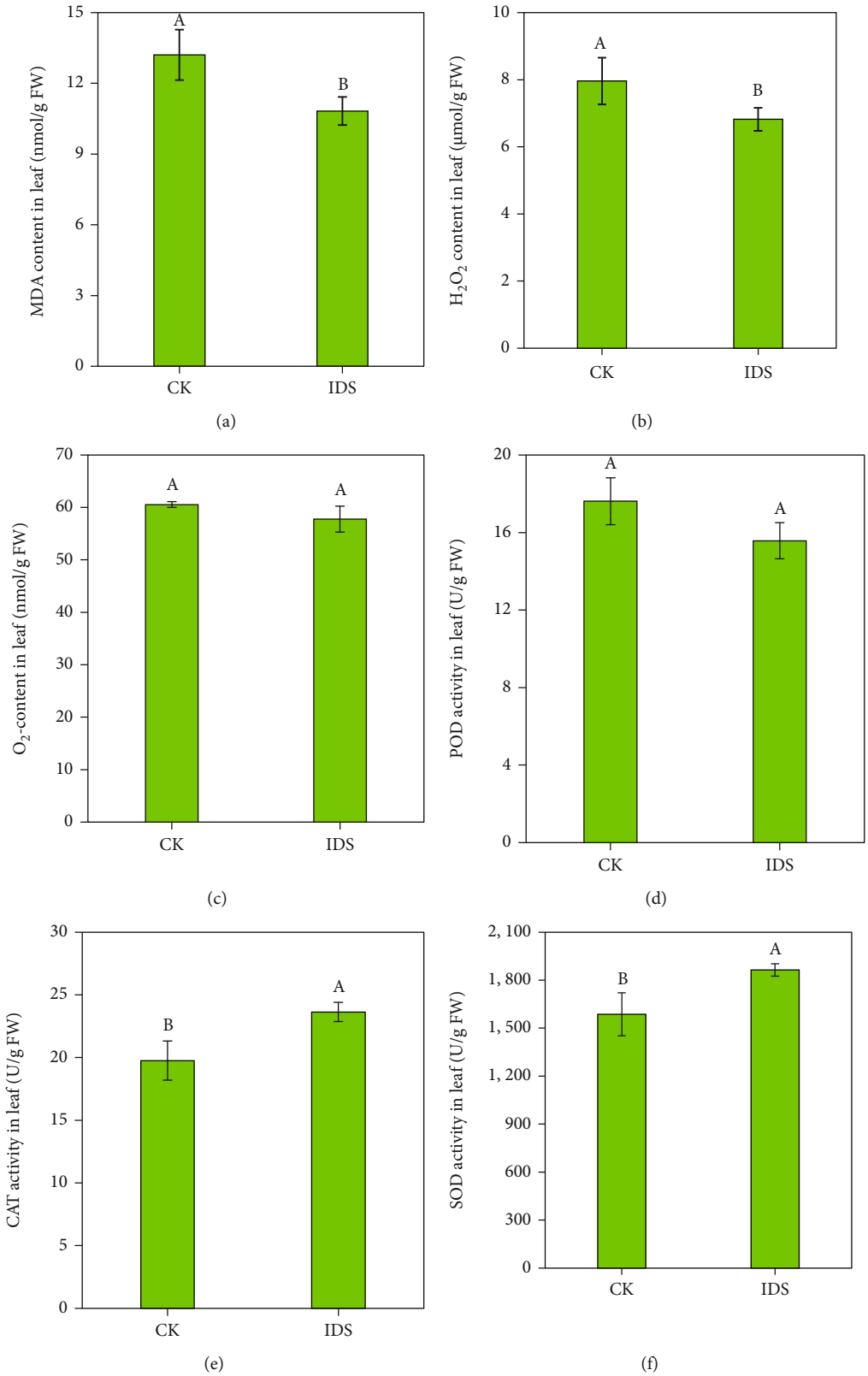

Figure 2: The effects of IDS on MDA, ROS, and antioxidant enzyme system in rapeseed leaves under Cd stress. Mean ± SD ($n = 5$). Different uppercase letters (A, B) indicate significant difference between CK and IDS treatment at $P < 0.05$.

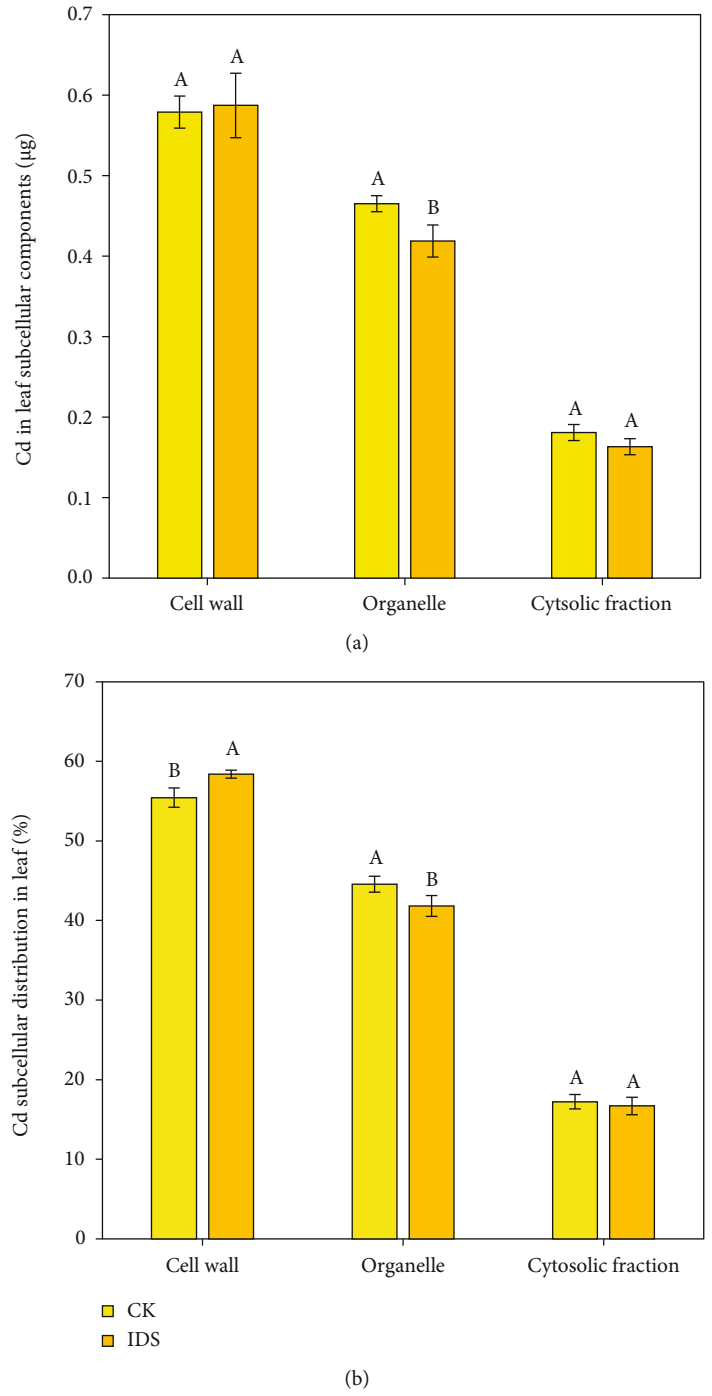

FIGURE 3: The effects of IDS on the subcellular distribution ratio of Cd in rapeseed leaves. Mean ± SD ($n = 5$). Different uppercase letters (A, B) indicate significant difference between CK and IDS treatment at $P < 0.05$.

accumulation in roots, but decreased Cd concentration and accumulation in leaves. Moreover, the Cd distribution ratios in the leaves and roots of IDS treatment were raised and reduced by 12.5% and 26.8%, respectively, compared to that of CK treatment. Cd transfer coefficient can indicate the ability of Cd transport and distribution from roots to the leaves. The decreased Cd transfer coefficient also suggested that IDS significantly reduced the Cd transport from roots to leaves.

3.3. IDS Decreased Oxidative Stress of ROS on Cells in Rapeseed Leaves. Cadmium could induce MDA and ROS accumulation to exacerbate cell membrane liquid peroxidation and oxidative damage to plant cells. According to the results of MDA, ROS content, and antioxidant enzyme activity in leaves, IDS application on rapeseed seedlings planted in Cd-contaminated soil decreased MDA and H_2O_2 accumulation in leaves at a significant level ($P < 0.05$), but had no obvious effect ($P > 0.05$) on $O_2^{\cdot-}$ contents

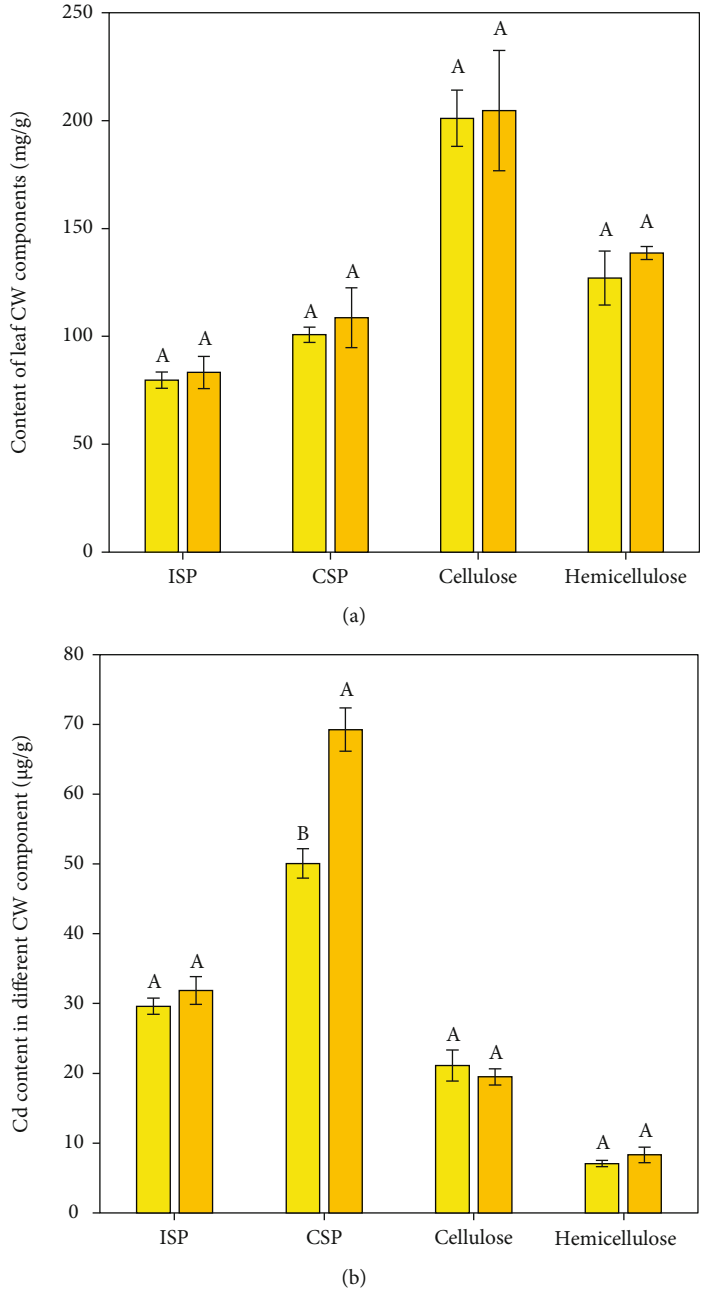

Figure 4: Continued.

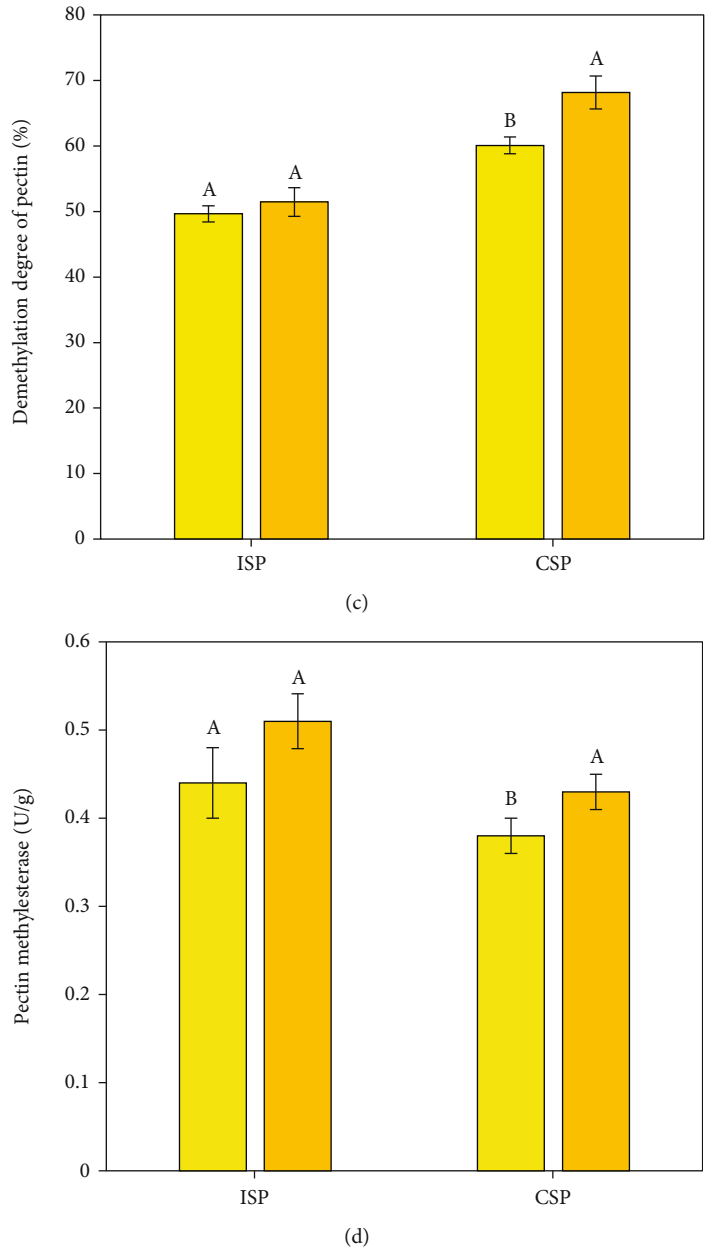

Figure 4: The effects of IDS on CW components, Cd content in CW components, and pectin demethylation in rapeseed leaves. Mean ± SD ($n = 5$). Different uppercase letters (A, B) indicate significant difference between CK and IDS treatment at $P < 0.05$.

(Figures 2(a)–2(c)). Improved activity of CAT and SOD, which is related to the removal of excess ROS in plants, was observed in rapeseed leaves under IDS application (Figures 2(e) and 2(f)). However, there was no significant effect on POD activity (Figure 2(d)).

3.4. IDS Promoted CW Fixation of Cd and Decreased Cd in Organelles in Rapeseed Leaves. To further reveal how IDS affects Cd subcellular distribution, we fractioned different parts of leaves into CWs, organelles, and cytosolic fractions (excluding vacuoles) and measured Cd content in each of these components in rapeseed leaves. IDS application did not affect Cd contents in CWs and cytosolic fractions, while significantly decreased Cd contents in organelles (Figure 3(a)). The Cd distribution ratio in different CW components shown in Figure 3(b) suggests higher Cd distribution in CWs and lower Cd distribution in organelles in leaves treated with IDS, indicating relieving Cd toxicity in organelles. In addition, IDS had no obvious effect on Cd content in cytosolic fractions (Figure 3(a)), indicating that IDS did not affect the vacuolar compartmentalization of Cd.

3.5. IDS Increased Cd Content in CSP by Promoting Pectin Demethylation in Rapeseed Leaves. The Cd in CWs was primarily chelated by various CW components such as cellulose, pectin, and hemicellulose. IDS application to rapeseed under Cd stress did not change the content of CSP, ISP, cellulose, and hemicellulose at a significant level ($P < 0.05$)

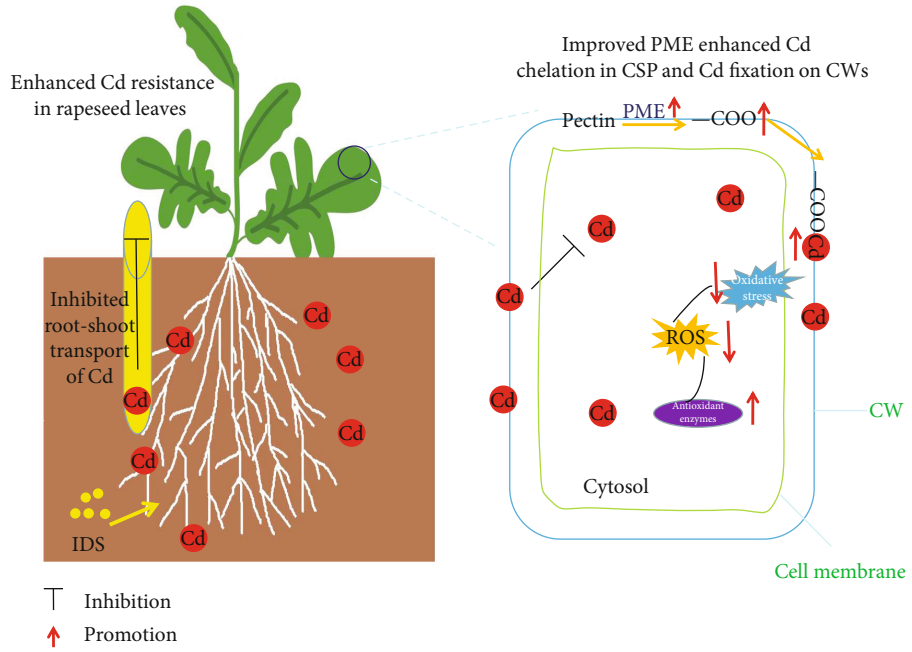

Figure 5: The schematic diagram illustrating the effects of IDS on cell wall components in determining Cd tolerance in leaves of rapeseed.

(Figure 4(a)). Interestingly, Cd contents in CSP were increased from 50.1 μg/g to 69.9 μg/g (Figure 4(b)), indicating that IDS promoted Cd chelation with CSP of the leaf CWs. To identify the ability of pectin to chelate Cd, we determined PME activity and the degree of methyl esterification of pectin, and the results showed that IDS increased PME activity of CSP and promoted demethylation of CSP (Figures 4(c) and 4(d)), thereby improving the carboxyl groups that can bind Cd.

4. Discussions

4.1. IDS Inhibited Cd Transportation from Roots to Shoots in Rapeseed. In plants, water, mineral nutrients, and heavy metals such as Cd absorbed from soil are transported from roots to shoots [38, 39]. In this study, IDS supplication did not significantly affect the mobility of Cd in soil (Table S1) and Cd accumulation in rapeseed roots (Table 1). However, our study indicated that IDS reduced Cd distribution to leaves of rapeseed and significantly decreased Cd transfer coefficient from roots to shoots (Table 1), suggesting that IDS inhibited the root-shoot transportation of Cd and ultimately alleviated Cd stress in the edible part of rapeseed [14], which is conducive to reducing the potential safety hazards of agricultural products.

4.2. IDS Decreased ROS Accumulation and Activated Antioxidant Enzymes in Leaves. Excessive Cd in plants usually increases the MDA content, which may raise membrane lipid peroxidation degree and indirectly aggravate the oxidative stress in cells [2, 18, 40]. ROS accumulation also causes oxidative damage to plants [41]. The presence of heavy metals can not only change the soil enzyme system, such as urease, protease, catalase, phosphatase, and β-glucosidase [42, 43], but also antioxidant enzymes in plants [2]. Higher antioxidant enzyme activity has been widely perceived to reduce ROS accumulation in plants under different stress [44–46]. Many studies have proposed that the activated antioxidant enzyme system plays an essential role in improving plant Cd resistance and acts as ROS scavengers [47]. In the present study, activated activities of CAT and SOD by IDS application contributed to decreased MDA content and reduced H_2O_2 accumulation under Cd toxicity in leaves (Figure 2). However, the significantly decreased Cd concentration in leaves with IDS supply (Table 1) may result in higher antioxidant enzyme activity, lower MDA, and ROS accumulation.

4.3. IDS Enhanced Cd Fixation in Leaf CWs by Increasing the Cd Chelation with CSP. It has been reported that the Cd subcellular reallocation determines Cd resistance in plants [15, 19, 41]. CW fixation and vacuole compartmentalization both play pivotal roles in enhancing plant Cd resistance [9, 16, 48]. 0.3% IDS application had no remarkable effect on Cd sequestration into vacuoles, but promoted Cd fixation in CWs, thereby decreasing Cd stress in organelles (Figure 3). The CW is the first barrier preventing Cd from entering cells, and CW fixation of Cd depends on the chelation of Cd in different CW components [9, 17]. To further investigate which CW component was mainly involved in improving Cd chelation with leaf CWs by IDS treatment, the content of different CW component and their Cd concentration was further analyzed. The results indicated that IDS did not affect the content of ISP, cellulose, CSP, and hemicellulose, while the Cd concentration in CSP was increased by IDS (Figures 4(a) and 4(b)).

Among the several CW components, pectin is the main component in Cd adsorption to CWs, and the pectin is

demethylated by PME and releases COO- that could form complexes with Cd^{2+} [17]. Our study found that IDS did not increase CSP content (Figure 4(b)), but significantly improved the degree of demethylation of CSP by raising PME activity (Figures 4(c) and 4(d)), producing more available groups for Cd binding to CWs and, thereby, improving Cd detoxification [14, 49]. The results indicated that the primary cause of improving Cd chelation with pectin was due to enhanced PME activity of CSP by IDS supply.

In summary, reducing Cd transport from roots to leaves combined with promoting more Cd retention in the CSP of leaf CWs induced by IDS application contributed to alleviating Cd stress in rapeseed leaves (Figure 5).

5. Conclusions

The results demonstrated that IDS significantly increased the dry matter and photosynthetic pigment contents and decreased Cd transfer coefficient from roots to leaves of rapeseed in Cd-polluted soil. In the meantime, decreased Cd in leaves resulted in higher activity of CAT and SOD, which led to less H_2O_2 accumulation and alleviated oxidative damage to cells. Additionally, the higher PME activity and lower demethylation degree of CSP induced by IDS were the main cause of higher chelation of Cd with CSP in leaves, which could be attributed to more distribution of Cd in CWs and less in organelles. Overall, the study results concluded that IDS application contributed to alleviating Cd stress in leaves of rapeseed by reducing Cd transport from roots to leaves combined with promoting more Cd retention in the CSP of leaf CWs. Our study enriches the theoretical basis of IDS improving Cd resistance of rapeseed leaves at a cellular level, and the results suggest that IDS has a good prospect for decreasing Cd in edible crops such as rapeseed.

Data Availability

The datasets used or analyzed during the current study are available from the corresponding author on reasonable request.

Disclosure

An earlier version of preprint on the manuscript has been presented as Research Square according to the following link https://www.researchsquare.com/article/rs-1098394/v1.

Conflicts of Interest

The authors declare that they have no conflict of interest financially or otherwise.

Authors' Contributions

All authors contributed to the study conception and design. Material preparation, data collection, and analysis were performed by Hui Tian, Zihan Zhu, and Haixing Song. The first draft of the manuscript was written by Xiuwen Wu, and all authors commented on previous versions of the manuscript. All authors read and approved the final manuscript.

Acknowledgments

This project is financially supported by the Natural Science Foundation of Shandong Province (ZR202102190565), the Start-up Fund for Introduced Talent of Qingdao Agricultural University (1121013), and the Scientific research project of Xuchang company of Henan Tobacco Company (6602421124).

Supplementary Materials

Supplementary Materials Table S1 Comparisons of soil characteristics between the control (CK) and IDS treatment. Mean ± SD ($n = 5$). Different lowercase indicates significant difference between these two treatments at $P < 0.05$ level. *(Supplementary Materials)*

References

[1] S. Clemens, "Safer food through plant science: reducing toxic element accumulation in crops," *Journal of Experimental Botany*, vol. 70, no. 20, pp. 5537–5557, 2019.

[2] X. W. Wu, H. X. Song, C. Y. Guan, and Z. H. Zhang, "Boron mitigates cadmium toxicity to rapeseed (Brassica napus) shoots by relieving oxidative stress and enhancing cadmium chelation onto cell walls," *Environmental Pollution*, vol. 263, p. 114546, 2020.

[3] M. Riaz, M. Kamran, Y. Fang et al., "Arbuscular mycorrhizal fungi-induced mitigation of heavy metal phytotoxicity in metal contaminated soils: a critical review," *Journal of Hazardous Materials*, vol. 402, p. 123919, 2021.

[4] S. Satarug, S. H. Garrett, M. A. Sens, and D. A. Sens, "Cadmium, environmental exposure, and health outcomes," *Environmental Health Perspectives*, vol. 118, no. 2, pp. 182–190, 2010.

[5] Y. L. Liu, B. Q. Tie, Y. X. Li et al., "Inoculation of soil with cadmium-resistant bacterium Delftia sp. b9 reduces cadmium accumulation in rice (Oryza sativa l.) grains," *Ecotoxicology and Environmental Safety*, vol. 163, pp. 223–229, 2018.

[6] Y. L. Liu, B. Q. Tie, O. Peng et al., "Inoculation of Cd-contaminated paddy soil with biochar-supported microbial cell composite: a novel approach to reducing cadmium accumulation in rice grains," *Chemosphere*, vol. 247, p. 125850, 2020.

[7] G. H. Li, Q. Cheng, and H. Chen, "Remediation of cd contaminated acidic rice fields using the combined application of lime and organic matter," *Environmental Sciences*, vol. 42, no. 2, pp. 925–931, 2021.

[8] H. Khalid, M. Zia-ur-Rehman, A. Naeem et al., "Solanum nigrum L.: A Novel Hyperaccumulator for the Phyto-Management of Cadmium Contaminated Soils," in *Cadmium Toxicity and Tolerance in Plants*, Academic Press, 2019.

[9] J. S. Peng, Y. J. Wang, G. Ding, H. L. Ma, Y. J. Zhang, and J. M. Gong, "A pivotal role of cell wall in cadmium accumulation in the Crassulaceae hyperaccumulator Sedum plumbizincicola," *Molecular Plant*, vol. 10, no. 5, pp. 771–774, 2017.

[10] J. Zhang, X. Cao, Z. Yao, Q. Lin, and G. Chen, "Phytoremediation of cd-contaminated farmland soil via various Sedum alfredii-oilseed rape cropping systems: efficiency comparison and cost-benefit analysis," *Journal of Hazardous Materials*, vol. 419, p. 126489, 2021.

[11] C. Chang, R. Yin, H. Zhang, and L. Yao, "Bioaccumulation and health risk assessment of heavy metals in the soil–rice system in a typical seleniferous area in central China," *Environmental Toxicology and Chemistry*, vol. 38, no. 7, pp. 1577–1584, 2019.

[12] S. Clemens, M. G. M. Aarts, S. Thomine, and N. Verbruggen, "Plant science: the key to preventing slow cadmium poisoning," *Trends in Plant Science*, vol. 18, no. 2, pp. 92–99, 2013.

[13] R. Blackshaw, E. Johnson, Y. Gan, W. May, D. Mcandrew, and V. Barthet, "Alternative oilseed crops for biodiesel feedstock on the Canadian prairies," *Canadian Journal of Plant Science*, vol. 91, no. 5, pp. 889–896, 2011.

[14] X. W. Wu, H. X. Song, C. Y. Guan, and Z. H. Zhang, "Boron alleviates cadmium toxicity in Brassica napus by promoting the chelation of cadmium onto the root cell wall components," *Science of The Total Environment*, vol. 728, p. 138833, 2020.

[15] X. Hu, T. Li, W. Xu, and Y. Chai, "Distribution of cadmium in subcellular fraction and expression difference of its transport genes among three cultivars of pepper," *Ecotoxicology and Environmental Safety*, vol. 216, no. 112182, pp. 112182–112182, 2021.

[16] S. S. Sharma, K. J. Dietz, and T. Mimura, "Vacuolar compartmentalization as indispensable component of heavy metal detoxification in plants," *Plant, Cell & Environment*, vol. 39, no. 5, pp. 1112–1126, 2016.

[17] A. Gutsch, S. Zouaghi, J. Renaut, A. Cuypers, J. F. Hausman, and K. Sergeant, "Changes in the proteome of Medicago sativa leaves in response to long-term cadmium exposure using a cell-wall targeted approach," *International Journal of Molecular Sciences*, vol. 19, no. 9, p. 2498, 2018.

[18] X. W. Wu, H. Tian, L. Li, C. Y. Guan, and Z. H. Zhang, "Higher Cd-accumulating oilseed rape has stronger Cd tolerance due to stronger Cd fixation in pectin and hemicellulose and higher Cd chelation," *Environmental Pollution*, vol. 285, p. 117218, 2021.

[19] Z. H. Zhang, T. Zhou, T. J. Tang et al., "A multiomics approach reveals the pivotal role of subcellular reallocation in determining rapeseed resistance to cadmium toxicity," *Journal of Experimental Botany*, vol. 70, no. 19, pp. 5437–5455, 2019.

[20] J. Cui, T. Liu, F. Li, J. Yi, C. Liu, and H. Yu, "Silica nanoparticles alleviate cadmium toxicity in rice cells: mechanisms and size effects," *Environmental Pollution*, vol. 228, pp. 363–369, 2017.

[21] M. Wójcik, J. Vangronsveld, J. D'Haen, and A. Tukiendorf, "Cadmium tolerance in Thlaspi caerulescens: II. Localization of cadmium in Thlaspi caerulescens," *Environmental and Experimental Botany*, vol. 53, no. 2, pp. 163–171, 2005.

[22] F. Paynel, A. Schaumann, M. Arkoun, O. Douchiche, and C. Morvan, "Temporal regulation of cell-wall pectin methylesterase and peroxidase isoforms in cadmium-treated flax hypocotyl," *Annals of Botany*, vol. 104, no. 7, pp. 1363–1372, 2009.

[23] D. Kołodyńska, "Iminodisuccinic acid as a new complexing agent for removal of heavy metal ions from industrial effluents," *Chemical Engineering Journal*, vol. 152, no. 1, pp. 277–288, 2009.

[24] M. Farid, S. Ali, and M. B. Shakoor, "EDTA Assisted Phytoremediation of Cadmium by Enhancing Growth and Antioxidant Defense System in Brassica napus L," *Environmental Science and Pollution Research*, vol. 22, no. 2, pp. 1534–1544, 2015.

[25] U. Habiba, S. Ali, M. Farid et al., "EDTA enhanced plant growth, antioxidant defense system, and phytoextraction of copper by Brassica napus L," *Environmental Science and Pollution Research*, vol. 22, no. 2, pp. 1534–1544, 2015.

[26] X. W. Wu, H. Tian, L. Li, and X. Q. Wang, "Polyaspartic acid alleviates cadmium toxicity in rapeseed leaves by affecting cadmium translocation and cell wall fixation of cadmium," *Ecotoxicology and Environmental Safety*, vol. 224, p. 112685, 2021.

[27] L. I. Jing and Y. Q. Wang, "Stabilizing effect of iminodisuccinic acid on metal ions," *Chinese Journal of Applied Chemistry*, vol. 20, no. 3, pp. 275–277, 2003.

[28] J. Ren, L. H. Wu, H. Y. Liu, and Y. M. Luo, "Effect of amendments on phytoextraction efficiency and metal uptake of following vegetable in heavy metal contaminated soil," *The Soil*, vol. 45, no. 2, pp. 233–238, 2013.

[29] J. Y. Liu and X. Liu, *Experimental course of plant physiology. Determination of H_2O_2 and $O_2^{\bullet-}$ concentration in plants, nineteenth ed*, Higher Education Press, Beijing, 2010.

[30] C. N. Giannopolitis and S. K. Ries, "Superoxide dismutases I. occurrence in higher plants," *Plant Physiology*, vol. 59, no. 2, pp. 309–314, 1977.

[31] G. O. Reff, "Peroxide levels and the activities of catalase, peroxidase, and indole acetic acid oxidase during and after chilling cucumber seedlings," *Plant Physiology*, vol. 65, no. 2, pp. 407-408, 1980.

[32] A. D. de Azevedo Neto, J. T. Prisco, J. Enéas-Filho, C. E. B. de Abreu, and E. Gomes-Filho, "Effect of salt stress on antioxidative enzymes and lipid peroxidation in leaves and roots of salt-tolerant and salt-sensitive maize genotypes," *Environmental and Experimental Botany*, vol. 56, no. 1, pp. 87–94, 2006.

[33] J. A. Buege and S. D. Aust, "Microsomal lipid peroxidation," *Methods in Enzymology*, vol. 52, pp. 302–310, 1978.

[34] V. S. Rathore, Y. P. S. Bajaj, and S. H. Wittwer, "Subcellular localization of zinc and calcium in bean (Phaseolus vulgaris L.) tissues," *Plant Physiology*, vol. 49, no. 2, pp. 207–211, 1972.

[35] J. J. Weigel and H. J. Jager, "Subcellular distribution and chemical form of cadmium in bean plant," *Plant Physiology*, vol. 65, no. 3, pp. 480–482, 1980.

[36] H. Hu and P. H. Brown, "Localization of boron in cell walls of squash and tobacco and its association with pectin (evidence for a structural role of boron in the cell wall)," *Plant Physiology*, vol. 105, no. 2, pp. 681–689, 1994.

[37] G. E. Anthon and D. M. Barrett, "Combined enzymatic and colorimetric method for determining the uronic acid and methylester content of pectin: application to tomato products," *Food Chemistry*, vol. 110, no. 1, pp. 239–247, 2008.

[38] A. De Boer and V. Volkov, "Logistics of water and salt transport through the plant: structure and functioning of the xylem," *Plant, Cell & Environment*, vol. 26, no. 1, pp. 87–101, 2003.

[39] J. S. Luo and Z. H. Zhang, "Proteomic changes in the xylem sap of brassica napus under cadmium stress and functional validation," *BMC Plant Biology*, vol. 19, no. 1, p. 280, 2019.

[40] R. L. Qiu, X. Zhao, Y. T. Tang, F. M. Yu, and P. J. Hu, "Antioxidative response to Cd in a newly discovered cadmium hyperaccumulator, Arabis paniculata F," *Chemosphere*, vol. 74, no. 1, pp. 6–12, 2008.

[41] M. Shahid, C. Dumat, S. Khalid, N. K. Niazi, and P. M. C. Antunes, "Cadmium bioavailability, uptake, toxicity and detoxification in soil-plant system," *Reviews of Environmental Contamination and Toxicology*, vol. 241, pp. 73–137, 2017.

[42] C. Duan, L. Fang, C. Yang, W. Chen, Y. Cui, and S. Li, "Reveal the response of enzyme activities to heavy metals through in

situ zymography," *Ecotoxicology and Environmental Safety*, vol. 156, pp. 106–115, 2018.

[43] L. Fang, Y. Liu, H. Tian, H. Chen, Y. Wang, and M. Huang, "Proper land use for heavy metal-polluted soil based on enzyme activity analysis around a Pb-Zn mine in Feng County, China," *Environmental Science and Pollution Research*, vol. 24, no. 36, pp. 28152–28164, 2017.

[44] L. Charton, A. Plett, and N. Linka, "Plant peroxisomal solute transporter proteins," *Journal of Integrative Plant Biology*, vol. 7, pp. 817–835, 2019.

[45] T. E. Rasafi, A. Oukarroum, A. Haddioui, H. Song, and J. Rinklebe, "Cadmium stress in plants: a critical review of the effects, mechanisms, and tolerance strategies," *Critical Reviews in Environmental Science and Technology*, vol. 1, pp. 1–52, 2022.

[46] M. Riaz, L. Yan, X. W. Wu, S. Hussain, O. Aziz, and C. C. Jiang, "Boron increases root elongation by reducing aluminum induced disorganized distribution of HG epitopes and alterations in subcellular cell wall structure of trifoliate orange roots," *Ecotoxicology and Environmental Safety*, vol. 165, pp. 202–210, 2018.

[47] D. M. Chen, D. Q. Chen, R. R. Xue et al., "Effects of boron, silicon and their interactions on cadmium accumulation and toxicity in rice plants," *Journal of Hazardous Materials*, vol. 367, pp. 447–455, 2019.

[48] Y. Huang, J. Chen, D. Zhang et al., "Enhanced vacuole compartmentalization of cadmium in root cells contributes to glutathione-induced reduction of cadmium translocation from roots to shoots in pakchoi (Brassica chinensis L.)," *Ecotoxicology and Environmental Safety*, vol. 208, p. 111616, 2021.

[49] C. Q. Zhu, X. C. Cao, L. F. Zhu et al., "Ammonium mitigates Cd toxicity in rice (Oryza sativa) via putrescine-dependent alterations of cell wall composition," *Plant Physiology and Biochemistry*, vol. 132, pp. 189–201, 2018.

Hindawi
Adsorption Science & Technology
Volume 2022, Article ID 4195119, 13 pages
https://doi.org/10.1155/2022/4195119

Research Article

Mechanisms of Stress Alleviation after Lime and Biochar Applications for *Brassica napus* L. in Cadmium-Contaminated Soil

Ming Lei,[1] Zhuoqing Li,[1] Beibei Zhang,[1] Xinqi Wang,[1] Boqing Tie,[1] Tehreem Ayaz,[1] and Xia Lu[1,2]

[1]*College of Resource and Environment, Hunan Agricultural University, Changsha 410128, China*
[2]*School of Art and Design, Shenzhen Polytechnic, Shenzhen 518055, China*

Correspondence should be addressed to Xinqi Wang; xinqiwang@hunau.edu.cn

Received 3 March 2022; Accepted 25 April 2022; Published 20 May 2022

Academic Editor: Haijian Bing

Lime and biochar amendments are widely used to immobilize cadmium (Cd) in agricultural soils and to ensure food security. However, the effects of these two soil amendments on the mechanisms of Cd stress alleviation in crops are unclear. Therefore, the effects of lime and biochar applications on Cd uptake, transport, subcellular distribution, antioxidant system, N metabolism, and related factors were examined in a soil-*Brassica napus* L. (*B. napus*) system. We found that lime application significantly increased the root Cd content by 41.5% but decreased Cd TF and shoot Cd by 81.0% and 74.3%, respectively, whereas biochar amendment decreased root and shoot Cd contents by 67.6% and 34.3%, respectively, but increased Cd TF by 104.1%. Lime treatment immobilized Cd in the cell wall of the root to reduce Cd transport, but biochar treatment increased the soluble fraction of Cd in root cells to improve the migration capacity of Cd. The significant negative relationship between the soil exchangeable Cd and Ca and the positive relationships between Cd and Ca both in shoot and root indicated that the Ca mediated Cd transport from soil to *B. napus* after lime and biochar applications. Additionally, lime amendment increased Cd proportion in the root cell walls to immobilize Cd, but biochar amendment increased Cd proportion in the soluble fraction to enhance Cd migration. Furthermore, biochar application significantly increased SOD, CAT, and POD by 17.5%, 95.4%, and 26.6%, whereas lime amendment only significantly enhanced CAT by 51.0%. Besides, both of biochar and lime applications increased shoot N content and GDH activity, but only the shoot NO_3^- content and nitrate reductase under biochar treatment were significantly altered. Overall, these findings suggested that lime is more efficient in reducing the transport of Cd from underground to aboveground and in improving Cd tolerance, whereas biochar tends to improve the antioxidant capacity and facilitate N metabolism. These results will provide significant strategies for selecting appropriate amendments to ensure the crops safety.

1. Introduction

Cadmium (Cd) levels in agricultural soils are continuously increasing in China [1, 2], which is usually due to human activities, such as sewage irrigation, atmospheric deposition, and application of chemical fertilizers and pesticides [3–5]. Cd is a nonessential element for plants but can disrupt physiological processes, accumulate in crops, and even enter the food chain to threaten human health since it has a relatively high solubility in soil and high translocation in plants [1, 6, 7]. It is of great significance to remediate Cd-contaminated agricultural soil.

Application of soil amendments is commonly used to remediate Cd-contaminated agricultural soils, which can decrease the Cd contents in crops by immobilizing Cd through complexation, adsorption, or ion exchange [8]. Lime and biochar are typical soil amendments because of their low cost, availability, and high efficiency [8–11]. Lime can effectively decrease the ability/bioavailability of Cd in soils by increasing soil pH, which thereby restricts crop Cd uptake [11, 12]. The large amount

calcium (Ca^{2+}) derived from liming materials not only has a significant positive effect on soil aggregation and structural stability, but also mediate the growth and stress alleviation of plant because it was the essential macroelement [13, 14]. However, little is known about the effect of Ca on plant stress alleviation after lime application in Cd-contaminated soils. Biochar has larger surface areas, higher cation exchange capacity, and higher porosity compared to other amendments [2, 4]. Numerous studies have shown that biochar can immobilize Cd and act as a slow-acting fertilizer [4, 15, 16], whereas the underlying mechanisms of stress alleviation in plants after biochar amendment are still unclear.

Crops have developed various mechanisms to cope with Cd stress, such as cell wall fixation, vacuolar compartmentalization, and antioxidant systems [6]. Cell wall components, namely, pectin, cellulose, and hemicellulose, can fix Cd by negatively charged groups such as $-COO^-$, -OH, and -SH [17, 18]. Ca^{2+} is an essential macroelement and also cross-linked with negatively charged $-COO^-$ to contribute to the cell wall structure and extensibility [13]. Larger Ca^{2+} contents in roots may stimulate the cell wall to produce more $-COO^-$, which may promote the fixation of more Cd^{2+} because of the same divalent cations and share transport channels and binding sites [19]. Both of lime and biochar amendments could change the soil exchangeable Ca^{2+}; however, whether these amendments mediated Cd transformation and tolerance in plants by Ca dynamics in the soil-plant system is still unclear. In addition, vacuoles can compartmentalize Cd by forming complexes with phytochelatins, S_2^-, organic acid anions, and amino acids [1]. These two tolerance mechanisms tend to fix Cd belowground and thus reduce its transport to the aerial plant parts. Although many studies have reported that lime and biochar can significantly reduce the available Cd contents in soils and decrease Cd concentrations in plants [11, 12, 20], whether the subcellular reallocation, cell wall composition, and the underlying physiological mechanisms are different after lime and biochar amendment remains unclear.

Plants can also stimulate the antioxidant enzyme system to alleviate oxidative stress (i.e., membrane permeability and subsequent generation of reactive oxygen species (ROS)) caused by Cd, such as by synthesizing superoxide (SOD), catalase (CAT), and peroxidase (POD) [21]. Some studies showed that biochar amendments enhanced SOD, CAT, and POD activities and reduced the ROS content [15, 22, 23]. Lime application also improved the activities of antioxidant enzymes by decreasing Cd stress [24]. The activity of plant antioxidant enzymes also increased with soil nutrient status [25–27]. But biochar application increased nutrient supply in Cd-contaminated soil, and the mechanism of its influence on antioxidant enzyme activity needs further study.

Nitrogen (N) is an important component of various structural, functional, and genetic molecules in plant cells and plays a vital role in defending various stresses [27–29]. Soil amendments not only change Cd migration and plant resistance but may also affect N metabolism. Previous studies have found that applications of lime [30] and biochar [31] could increase N availability. Furthermore, lime enhanced the activity of nitrate reductase (NR) and N use efficiency of maize [32]. Biochar also enhanced the N use efficiency by improving the activities of N metabolic enzymes (e.g., NR, glutamine synthetase (GS), and glutamate dehydrogenase (GDH), which accelerated nitrate (NO_3^-) assimilation in crabapple and cabbage [31, 33]. However, these studies were all conducted in clean soil that were not contaminated by heavy metals. The effect of lime or biochar on plant N metabolism in Cd-contaminated agricultural systems needs to be further explored.

Brassica napus L. (*B. napus*) is a widely cultivated oil crop in southern China, but its growth is constrained by Cd stress and low N use efficiency [17, 34]. Previous studies focused on the stabilization mechanism of soil Cd under the applications of lime and biochar, but little attention was paid to the tolerance mechanism of Cd in plant after lime and biochar treatments. To better understand the comprehensive effects of commonly used soil amendments on Cd-contaminated soil-*B. napus* systems, we conducted *B. napus* pot experiments with lime or biochar application. Specifically, we hypothesized that (1) the Cd migration in soil-*B. napus* systems varies between lime and biochar treatments, (2) the biochar treatment had stronger impacts on *B. napus* antioxidant system, and (3) the N metabolism for *B. napus*.

2. Materials and Methods

2.1. Soil Collection, Plant Materials, and Growth Conditions. Cd-contaminated soil (0–15 cm of tillage layer) was collected from an oilseed rape-rice rotation system in Zhuzhou (26.82°N, 113.53°E), China. The total Cd content was 1.66 mg/kg, and the pH was 5.58 in the soil, which exceeded the risk intervention value (0.3 mg/kg) but was lower than the risk control value (2 mg/kg) when compared to the standard values for paddy soil (GB 15618–2018). It is essential to remediate these moderately Cd-contaminated agricultural soils and maintain their quality and health for the sustainability of ecosystem services and food security because of the limited cultivated area in China [1]. The soil was air-dried and ground to pass through a 2-mm nylon sieve, and then, it was thoroughly mixed for the pot experiment. This study involved three treatments (four replicates each): no amendment (CK), 0.3% lime (the common application rate in this contaminated region), and 1.0% biochar (produced from rice straw at 250°C for 2.5 h; the common amendment rate from [8, 22, 23]). The characterization method and information in the biochar are presented in the Supporting Information (Table S1, Figure S1). Each pot contained 1.0 kg of soil and base fertilizers (e.g., 0.25 g/kg urea, 0.41 g/kg $Ca(H_2PO_4)_2{\cdot}H_2O$, 0.13 g/kg KCl, and 0.05 g/kg H_3BO_3). After stabilization for one week, two plump *B. napus* (Westar 10) were transplanted into black plastic pots with different treatments. These pots were placed in a greenhouse at a temperature of 20~25°C and 55~60% relative humidity for 40 days and were irrigated with ultrapure water.

At the end of cultivation, samples from soils, roots, and shoots were collected and thoroughly mixed and then

divided into multiple subsamples according to the requirements of the property to be analyzed.

2.2. Determination of Soil and Plant Elements. The soil samples were ground and passed through sieves (2 mm and 0.149 mm) after air-drying. The soil pH levels were measured at a v/w ratio of 2.5 with a pH meter (Seven Compact S220, Mettler Toledo). Ammonium acetate (NH_4OAc, 1 M) was used to extract the exchangeable Ca (EX-Ca) in the soil [35]. The soil was digested in an acid mixture of HNO_3/HCl/$HClO_4$ [36] by an electronic heat digestion furnace (Digi-Block EHD36, Lab Tech) for Cd and Ca analysis. The soil exchangeable Cd (EX-Cd) was extracted with 1.0 M $MgCl_2$ solution (v/w ratio, 10 : 1) [37]. In addition, the roots and shoots were ground into fine powder and subsequently digested in an acid mixture of HNO_3/$HClO_4$ (4 : 1, v/v) at 200°C for 2 h [38].

The obtained elements were quantified with inductively coupled plasma mass spectrometry (ICP-MS, NexION™ 350X; PerkinElmer, MA, USA). EX-Ca was quantified with a flame atomic absorption spectrophotometer (AA-6880, Shimadzu, Japan). The Chinese national standard reference materials (e.g., GSS-6, GSS-8, and CSV-2) were used to determine the reliability of the results. The recovery rate for soil and plant Cd was 88–98% and 95–102%, respectively.

2.3. Cd Determinations in Subcellular Structures and Xylem Sap. Fresh roots and shoots were used to determine the Cd contents at the subcellular level by using a method described by Wu et al. [38]. Fresh samples were ground with a mixed solution (e.g., sucrose, dithiothreitol, and Tris-HCl buffer solution) and separated into cell walls, organelles, and soluble parts by different centrifugal forces. Xylem sap was collected based on the method of Lu et al. [14]. Finally, the method of element determination described in the previous section was used to determine the Cd contents in the subcellular structures and xylem sap.

2.4. Determination of Cell Wall Components. The cell wall material of the shoots was separated according to Hu and Brown [39]. The levels of the different cell wall components (e.g., ionic soluble pectin (ISP), covalent soluble pectin (CSP), lignin, cellulose, and hemicellulose) were determined using the corresponding kits (Suzhou Comin Biotechnology Co., Ltd, China).

2.5. Determination of ROS, MDA, and Antioxidant Enzymes in Shoots. A malondialdehyde (MDA) supernatant was obtained by grinding fresh shoots in 0.1% (w/v) cold trichloroacetic acid and centrifuging at 4°C for 30 min (6,000×*g*) [21]. To determine the H_2O_2 and $O_2^{-}\cdot$ content and POD, SOD, and CAT activities, fresh shoots were ground in 0.05 M phosphate buffer and were then centrifuged at 12,000*g* for 10 min at 4°C [23]. Finally, the levels or activities of MDA, H_2O_2, O_2^{-}, SOD, CAT, and POD in the supernatants were measured according to the kit instructions (Suzhou Comin Biotechnology Co., Ltd, China).

2.6. Determination of N Metabolism Traits in Shoots. The N concentration in shoots was determined with the Kjeldahl method. The shoot NO_3^{-} concentration was determined spectrophotometrically using the salicylic acid nitration method according to Xiong et al. [40]. The activities of NR, GS, and GDH were measured by using a modified method based on Ma et al. [29] and Zhang et al. [41].

2.7. Bioconcentration Factor (BCF) and Translocation Factor (TF). The bioconcentration factor (BCF) was defined as the ratio of the Cd concentration in the roots to the Cd concentration in the soil; the translocation factor (TF) was defined as the ratio of the Cd concentration in the roots to that in the shoots. These calculation formulas are based on Mujeeb et al. [42].

2.8. Statistical Analysis. One-way analysis of variance (ANOVA) and least significant difference (LSD) were conducted to analyze the differences among treatments. Linear regression analyses were used to determine the correlations among variables ($P < 0.05$ and $P < 0.01$). Principal component analysis (PCA) was used to analyze the relationships among the *B. napus* traits and identify a few traits that explain most of the variance observed in a large of manifest traits. Statistical analyses were conducted using SPSS ver. 25.0 (SPSS Inc.) and R ver.4.0.2.

3. Results

3.1. Cd Transfer in the Soil-B. napus System. The soil EX-Cd content reduced by 33.6% and 16.9% after applications of lime and biochar (Figure 1(a), $P < 0.05$), respectively, while the pH increased by 1.58 and 0.77 units, respectively. In addition, the EX-Ca content increased by 35.8% and 9.0% under the lime and biochar treatments, respectively (Figure 1(b), $P < 0.05$). Furthermore, neither lime nor biochar significantly reduced the total Cd contents in the soil (Figure S2a). The EX-Ca content and pH were significantly negatively related to the EX-Cd values (Figure 1(h), $P < 0.05$).

The Cd accumulation patterns were different for *B. napus* under the lime and biochar amendments (Figure 1(d), $P < 0.05$). For the lime treatment, the root Cd content increased by 41.5%, and the shoot Cd content decreased by 74.3%. However, the root and shoot Cd level were reduced by 67.6% and 34.3%, respectively, under the biochar treatment. The BCF decreased (70.0%) after biochar amendment, but no significant changes were found for the lime application (Figure 1(f)). Furthermore, the Cd content in xylem sap decreased by 71.0% after lime application, but those after biochar amendment did not change significantly (Figure 1(c)). The TF values decreased significantly by 81.0% after lime application, while that for the biochar treatments increased by 104.1% (Figure 1(f), $P < 0.05$). Additionally, the Cd concentration was positively correlated with the Ca content ($P < 0.05$) in both the roots and shoots (Figure 1(g)).

3.2. Subcellular Distribution of Cd and Cell Wall Fractions. The Cd redistribution in the roots was markedly different at the subcellular level after the lime and biochar applications (Figure 1(e), $P < 0.05$). The Cd proportion in the cell walls increased by 19.4%, while that in the organelle fraction decreased by 7.18% and that in the soluble fraction did not

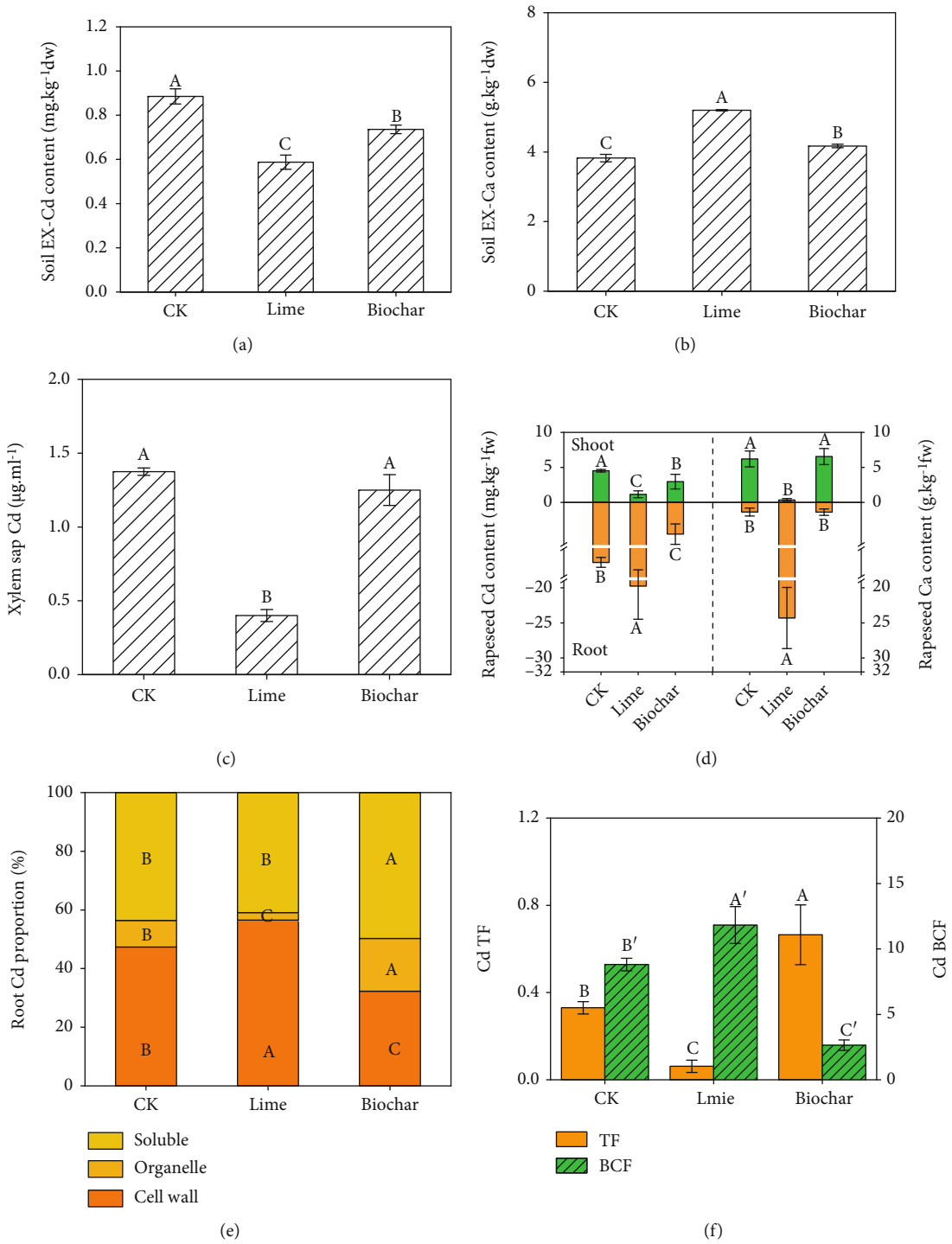

Figure 1: Continued.

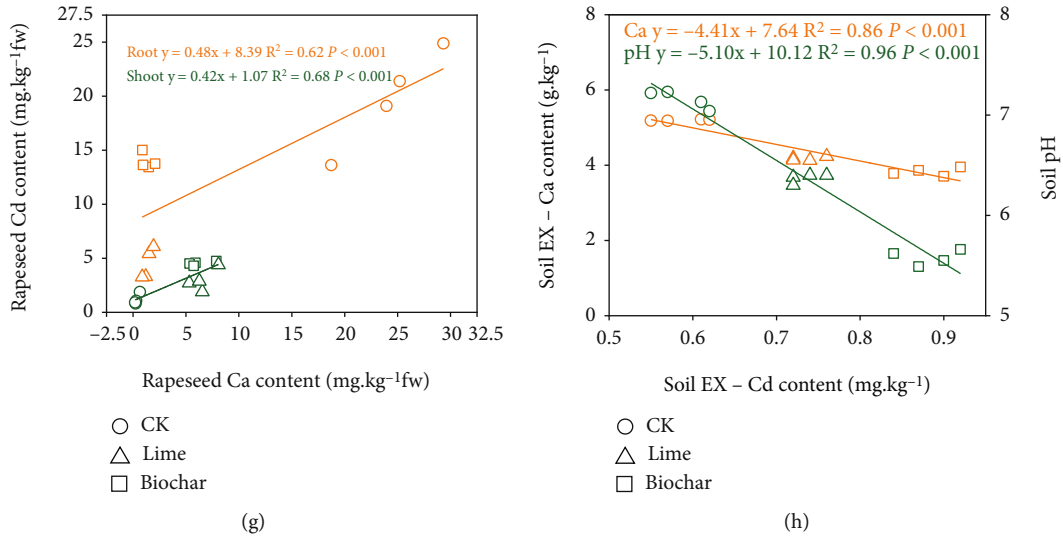

Figure 1: Cd accumulations and related factors in soil-*B. napus* system under three treatments. *B. napus*: *Brassica napus L.*; EX-Cd: exchangeable cadmium; EX-Ca: exchangeable calcium; TF: translocation factor; and BCF: bioconcentration factor. Means ± SD ($n = 4$). Different lowercase letters indicate significant differences ($P < 0.05$) between the three treatments.

change after lime treatment. The Cd proportions in the soluble and organelle fractions increased by 98.8% and 14.0%, respectively, whereas that in the cell wall fraction decreased by 31.9% after biochar amendment. However, the Cd redistributions in the shoots among the three treatments were not significantly different (Figure S2e, $P > 0.05$). However, the Cd redistributions in the shoots among the three treatments were not significantly different (Figure S2e, $P > 0.05$).

Regarding the cell wall fractions in the shoots, the lignin content reduced by 22.8% and 11.6% after the applications of lime and biochar, respectively (Figure 2(a)). The CSP and ISP levels increased by 15.5% and 14.6%, respectively, for the lime treatment, while those for the biochar amendment increased by 19.7% and 16.8%, respectively (Figures 2(b) and 2(c), $P < 0.05$). No significant differences were found in the hemicellulose and cellulose levels among all treatments. (Figure S2b–S2c, $P > 0.05$). In addition, the lignin content was positively correlated with the Cd content in shoots (Figure 3(a), $P < 0.05$).

3.3. The Antioxidant System in the Shoots. For the biochar treatment, the SOD, CAT, and POD activities increased significantly increased by 17.5%, 95.4%, and 26.6%, respectively (Figures 2(d)–2(f), $P < 0.05$). However, only the CAT activity was significantly enhanced (by 51.0%) after lime application (Figure 2(e), $P < 0.05$). In addition, the MDA and H_2O_2 levels were significantly reduced by both lime and biochar amendments (by 20.2% and 29.0%, respectively, and by 16.0% and 16.6%, respectively, Figures 2(g) and 2(i), $P < 0.05$). The $O_2^{-}\cdot$ concentrations were markedly reduced after the lime application, while no significant changes were observed after biochar application (Figure 2(h)). Furthermore, the MDA, $O_2^{-}\cdot$, and H_2O_2 levels were positively correlated with Cd contents (Figures 3(b)–3(d), $P < 0.05$), but no correlations were found among the antioxidant enzymes and the Cd content (Figure S3a–c, $P > 0.05$).

3.4. N Metabolism in B. napus. The N content in roots increased significantly after both the lime and biochar applications, while the increment for the latter was 2.3 times greater than that of CK (Figure 2(j), $P < 0.05$). The NO_3^- content decreased by 19.7% and the NR activity improved by 18.2% in the shoots under biochar application ($P < 0.05$), while no significant changes were found for the lime amendment (Figures 2(l) and 2(m), $P > 0.05$). The GDH activity improved by 49.3% and 38.0% (Figure 2(n), $P < 0.05$) after the applications of lime and biochar, respectively. No significant differences in the GS activity were observed among all treatments (Figure S2d, $P > 0.05$). Furthermore, negative correlations were found for the Cd content and the N content in the roots and shoots (Figures 3(e) and 3(f), $P < 0.05$) and for the Cd content with the GDH activity in the shoots (Figure 3(g), $P < 0.05$). In addition, no relationships were found between the Cd content and NO_3^- and NR (Figure S3d–e, $P > 0.05$).

3.5. Principal Component Analysis. PCA was used to explore the patterns of the traits associated with stress alleviation in *B. napus* by combining the data across the three treatments (Figure 4). PCA axis 1 showed strong positive loadings for root Cd and shoot N but negative loadings for MDA, ROS (H_2O_2 and $O_2^{-}\cdot$), lignin, shoot Ca, Cd TF, and Cd in the shoot, xylem sap, and root organelle fractions. PCA axis 2 had strong positive loadings for shoot NO_3^-, root Cd and cell wall Cd fractions but negative loadings for antioxidant enzymes (e.g., CAT, POD, and SOD), N metabolism (e.g., root N, NR, and GDH), pectin (CSP and ISP), and Cd in the root soluble fraction. Additionally, the detoxification traits (e.g., root Ca content and cell wall Cd fractions), which

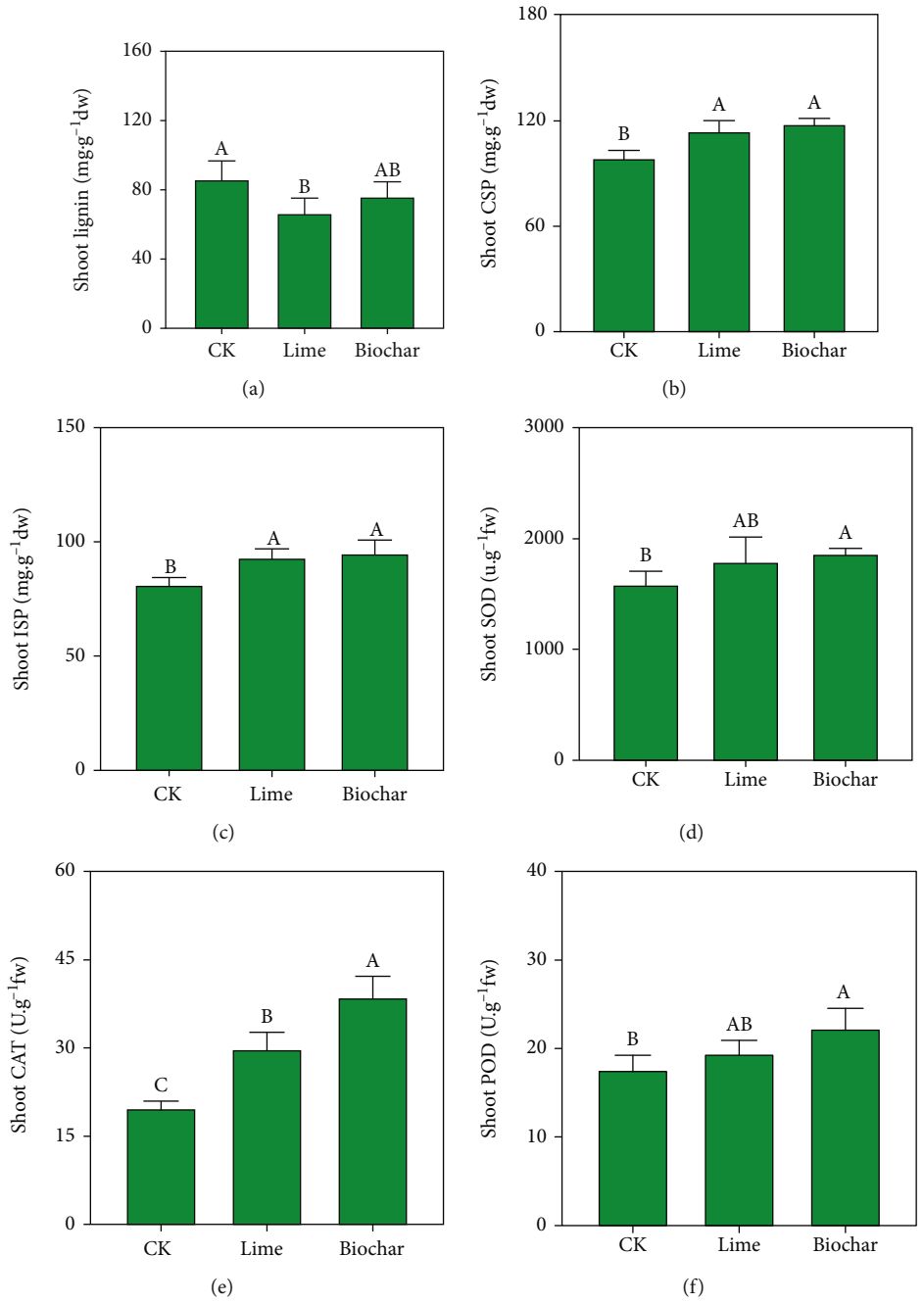

Figure 2: Continued.

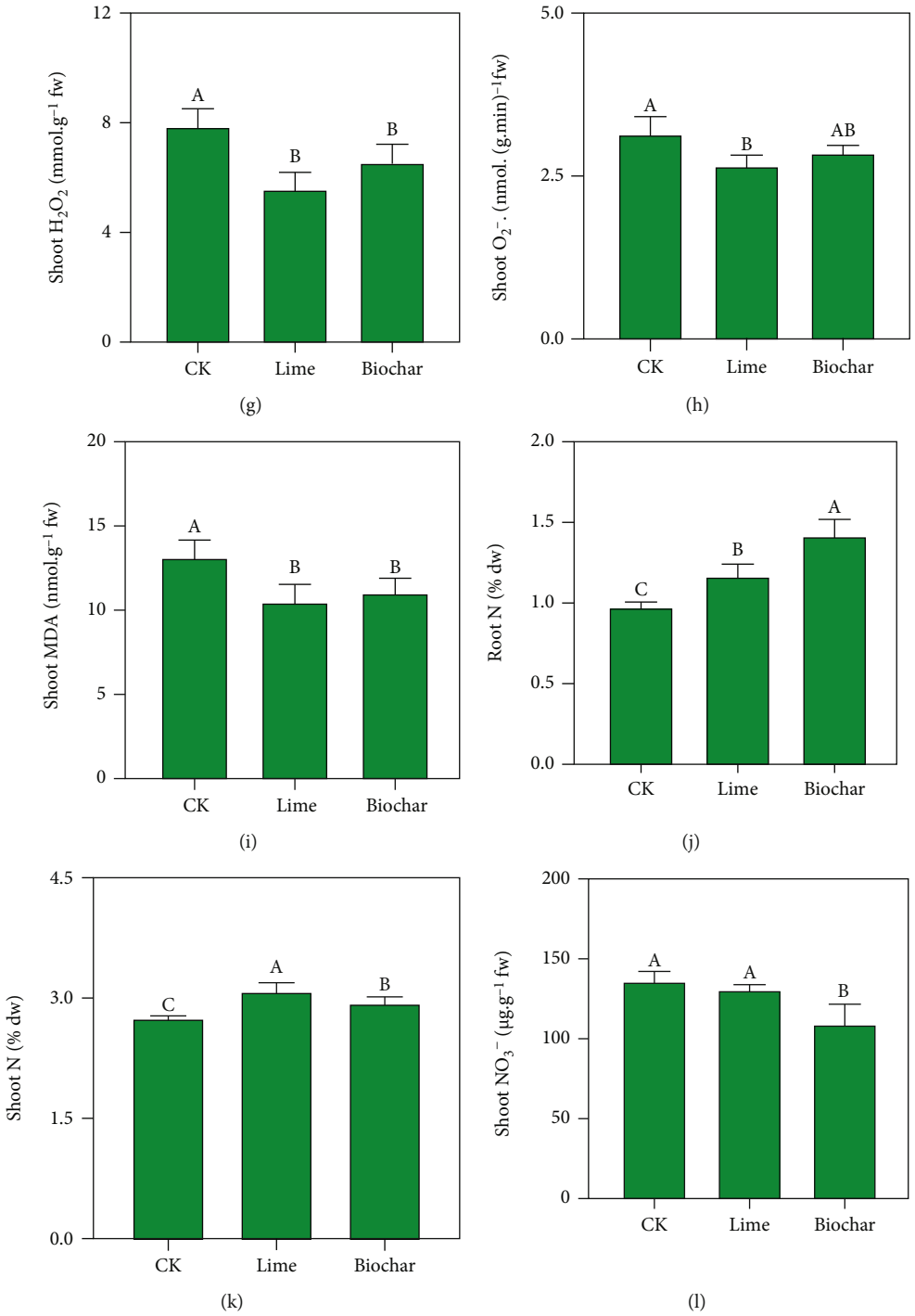

Figure 2: Continued.

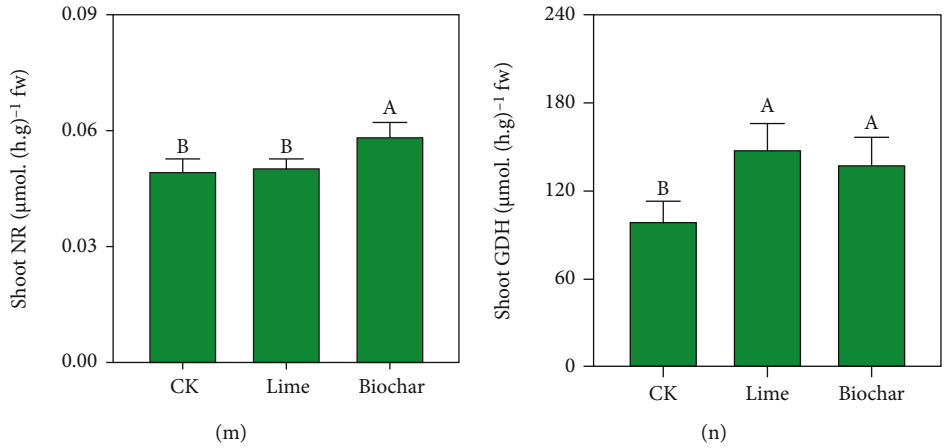

Figure 2: Responses of *B. napus* physiological characteristics under three treatments. *B. napus*: *Brassica napus L.*; ISP: ion-bound pectin; CSP: covalently bound pectin; MDA: malondialdehyde; H_2O_2: hydrogen peroxide; O_2^{-}·: superoxide anion; SOD: superoxide dismutase; CAT: catalase; POD: peroxidase; NO_3^-: nitrate; NR: nitrate reductase; GDH, and glutamate dehydrogenase. Means ± SD ($n = 4$). Different lowercase letters indicate significant differences ($P < 0.05$) between the three treatments.

are shown in the upper right part of Figure 4, are associated with lime treatment, while different traits (e.g., antioxidant enzymes and N metabolism), which are shown in the lower part of Figure 4, are associated with biochar treatment.

4. Discussion

4.1. Effects of Lime and Biochar on Cd Translocation in Soil-B. napus System. Partially supporting our first hypothesis, we found that the Cd migration patterns from soil to roots and from roots to shoots between lime and biochar treatments were different, whereas the Cd distribution in the shoots showed similar dynamics. Specifically, the Cd content in the *B. napus* roots increased after lime amendment but decreased after biochar amendment (Figure 1(d)), and these different root Cd levels resulted in differences in the BCF (Figure 1(f)). The divergent effects of lime and biochar on the root Cd content and BCF may result from the influence of Ca since the root Cd content increased with Ca (Figure 1(g)). Ca and Cd are both divalent cations and share many transporters, transport channels, and binding sites [43]. Lu et al. [14] demonstrated that Cd could enter plant guard cells through Ca channels and synergistic interactions and thus accelerate Cd accumulation in plants. Therefore, although the soil Cd was immobilized after lime application (Figure 1(a)), large amounts of Ca may entice the transport channel to promote Cd absorption by the roots. Moreover, biochar application reduced the root Cd content (Figure 1(d)). Numerous studies demonstrated that the application of biochar to soil significantly decreased the phytoavailability of Cd and its uptake by *B. napus* [4, 44, 45]. These results may be attributed to the increased soil pH and formation of an organic matter Cd fraction that prevented Cd uptake by the roots [8, 46].

The patterns of subcellular localization (e.g., cell wall, organelles, and soluble fraction) can help determine Cd accumulation, translocation, and detoxification mechanisms in plants [17]. First, the cell wall Cd fractions in the roots increased significantly after lime application, but not after biochar amendment (Figure 1(e)). Recent studies have indicated that the cell wall is the most important defense mechanism because of the negative charges present on it (i.e., $-COO^-$, -OH, and -SH), which can bind Cd [17–19]. Ca^{2+}, an essential component that is cross-linked with negatively charged $-COO^-$, contributes to the cell wall structure and extensibility [13]. Cd^{2+} can replace Ca^{2+} because of its stronger ion binding and replacement capabilities [19]. Therefore, a larger Ca^{2+} uptake by roots after lime application may stimulate the cell wall to produce more $-COO^-$, which then promotes the fixation of more Cd^{2+} [19]. In addition, the Cd content in the xylem sap was significantly reduced after lime application, but not after biochar amendment, indicating that the amount of Cd that migrated from the underground to aboveground plant parts was greatly reduced. These differences in root Cd content, cell wall Cd fractions in the roots, and Cd contents in the xylem sap further result in a lower TF in lime treatment but a higher one in the biochar treatment. Second, the soluble Cd fraction in the roots was not significantly altered after lime amendment but increased by biochar application (Figure 1(e)), which is consistent with the results of Li et al. [16]. The mobility of the soluble fraction of Cd is stronger than those of the cell wall and organelle components [17, 38]. The increased soluble Cd fraction could further enhance Cd translocation from roots to shoots and then lead to a higher TF level after biochar amendment (Figure 1(f)) [16].

The cell wall Cd fractions in the shoots were not significantly changed (Figure S2e), while some of the cell wall components for the shoots were significantly altered and showed similar changes after lime and biochar amendments (Figures 2(a)–2(c)). We found that the lignin amounts in the shoots decreased significantly and were positively correlated with the Cd contents (Figure 3(a), $P < 0.05$), which was consistent with other studies [47, 48]. Moura et al. [49] indicated that lignin deposition may result from Cd stress in plant cells. Furthermore, the lignification of cell

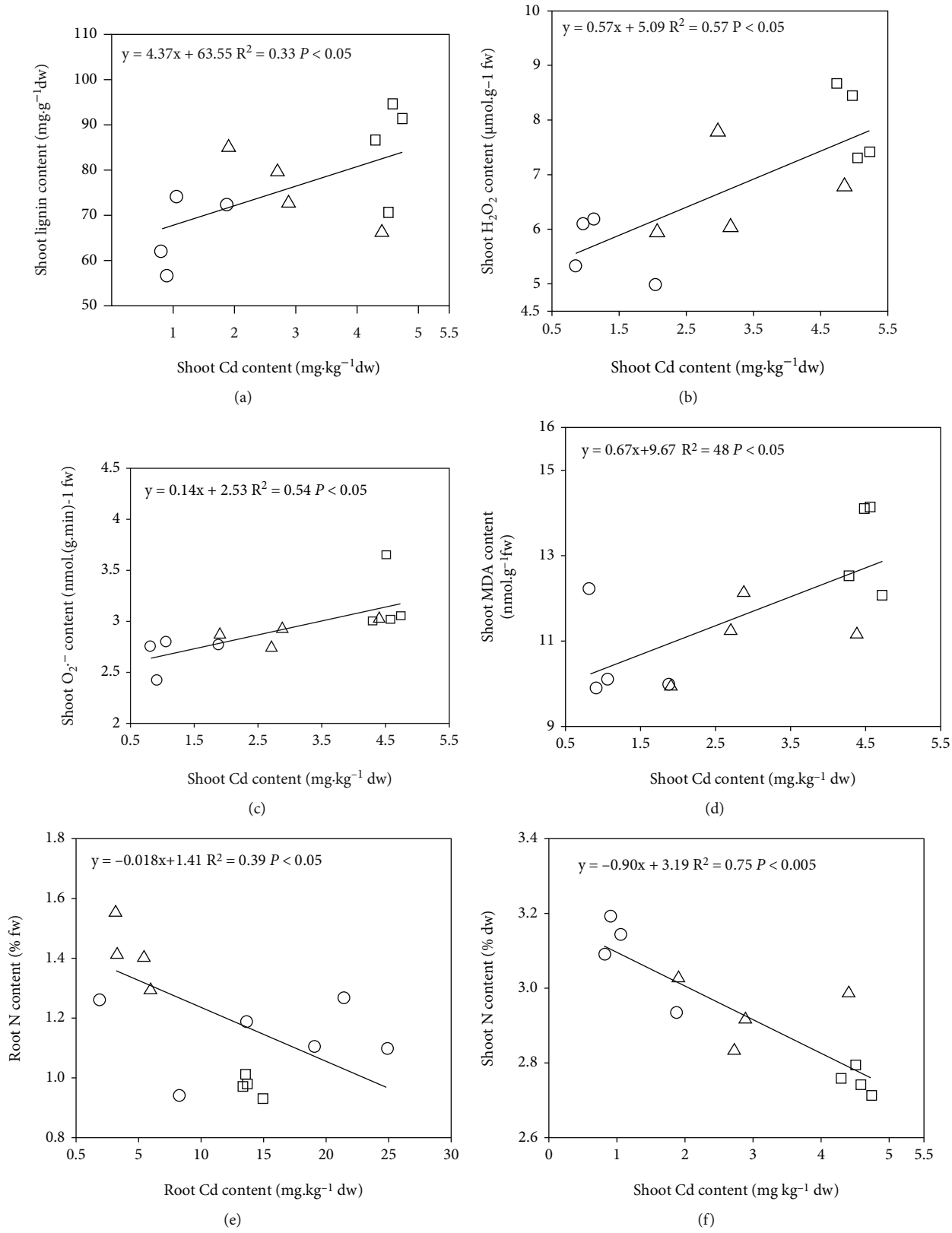

Figure 3: Continued.

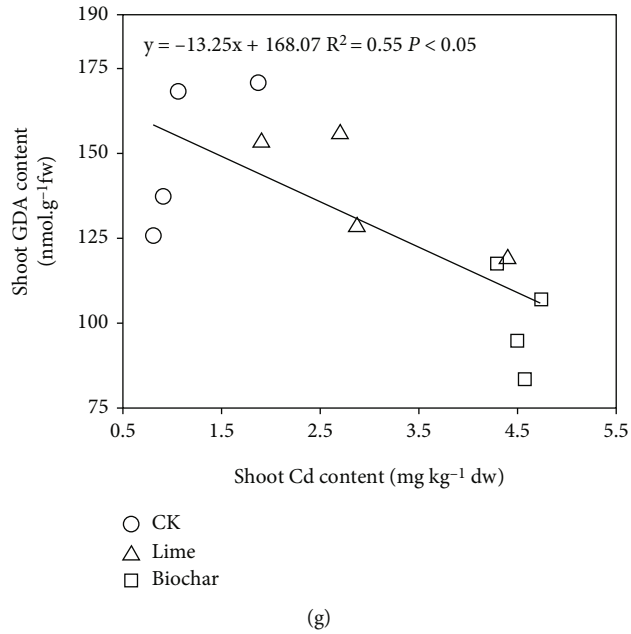

(g)

Figure 3: Relationships between Cd accumulation and related physiological traits. MDA: malondialdehyde; H_2O_2: hydrogen peroxide; O_2^-·: superoxide anion; and GDH: glutamate dehydrogenase.

walls can also inhibit plant growth [18]. Therefore, the lignin content decreased in shoots indicated that applications of lime and biochar reduced Cd stress on shoot cells. Moreover, the pectin (e.g., CSP and ISP) levels increased after the lime and biochar applications, which indicated the alleviation of Cd toxicity to shoot cells [38].

4.2. Responses of the Antioxidant System of B. napus after Lime and Biochar Applications. ROS (O_2^- and H_2O_2) and MDA accumulate in plant cells under Cd stress, which can result in organelle damage [21]. This study found that the ROS and MDA levels decreased after both lime and biochar applications (Figures 2(g)–2(i)), which was consistent with the studies of Kamran et al. [45] and Huang et al. [24]. Additionally, the ROS and MDA levels in the shoots exhibited a positive relationship with the Cd content (Figures 3(b)–3(d)). These results implied that the decreased Cd contents in the shoots after lime and biochar applications could directly alleviate oxidative stress [24, 45]. Furthermore, the antioxidant system is an important defense mechanism for plants to cope with Cd stress. For example, SOD can convert O_2^-· to H_2O_2, and CAT and POD can degrade H_2O_2 to H_2O, thus reducing the MDA content in cells [21, 47]. Supporting our second hypothesis, biochar amendment had relatively greater impacts on antioxidant enzyme activities. Specifically, the SOD, CAT, and POD activities were enhanced significantly after biochar application, while only the CAT activity improved after lime application (Figures 2(d)–2(f)). Previous studies found that biochar treatment could upregulate pathways and genes associated with plant defense, thereby enhancing enzyme activities [50, 51]. Numerous studies also proved that biochar application improved the activities of SOD, CAT, and POD and reduced the MDA and ROS contents, which decreased oxidative stress [15, 22, 23, 45]. Therefore, compared with lime application, biochar amendment tends to exert stronger effects on antioxidant enzymes to avoid oxidative damage.

4.3. N Metabolism Responses in B. napus after Lime and Biochar Applications. B. napus production is often N-limited because of the low N use efficiency [34]. In the present study, the N content increased in both roots and shoots under lime and biochar applications (Figures 2(j) and 2(k)). Other studies have also found that the applications of lime and biochar increased the N contents in crops [30–32, 51]. Additionally, the N content was negatively correlated with the Cd content in both roots and shoots (Figures 3(e) and 3(f)), implying that decreased Cd contents may improve the N uptake of *B. napus*. NO_3^- and N metabolic enzymes (such as NR, GS, and GDH) are important limiting factors for the N metabolism process in plants [28, 29, 52]. Yang et al. [27] found that the plant N content and metabolic enzyme activities decreased under Cd stress. Our study found that the NO_3^- content decreased and the NR activity was improved in the shoots after biochar application, while no significant changes were observed after lime amendment (Figures 2(l) and 2(m)), supporting our third hypothesis. This result implied that biochar application accelerated the process of N assimilation, i.e., incentivized NR activity to improve the conversion of NO_3^- to NO_2-. Some studies also found that biochar application improved the activities of metabolic enzymes (e.g., NR and GDH) in crops [31, 53]. Therefore, in comparison with lime application, biochar amendment was not only an efficient way to reduce Cd stress but was also an appropriate method to enhance N use efficiency for N-limited crops.

The PCA results showed that higher Cd levels increased oxidative stress since the higher ROS and lignin contents in

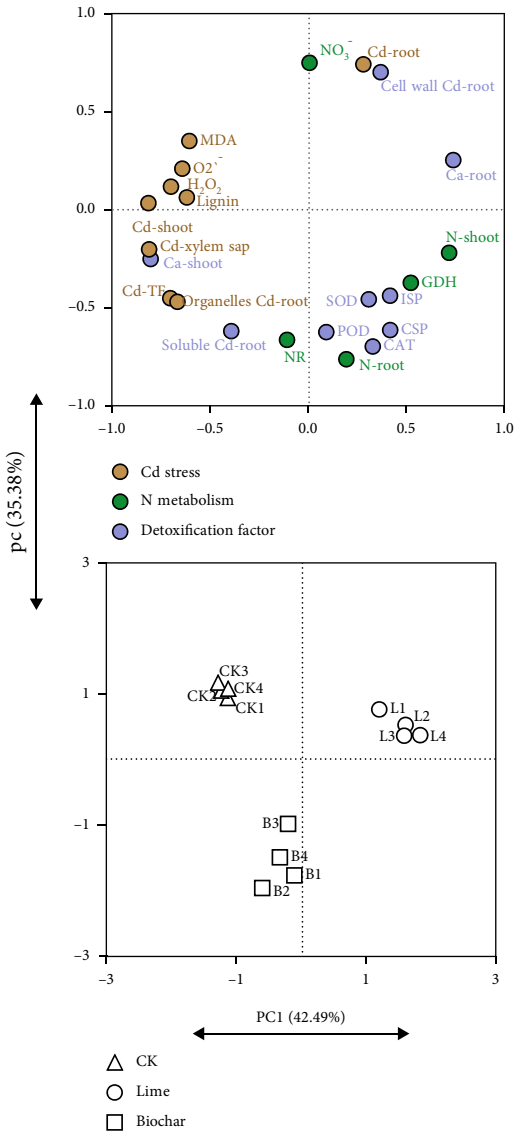

FIGURE 4: Principal component analysis. Principal component analysis for (a) the 23 traits and (b) the 3 treatments for the first two axes. ISP: ion-bound pectin; CSP: covalently bound pectin; MDA: malondialdehyde; H_2O_2: hydrogen peroxide; O_2^{-}: superoxide anion; SOD: superoxide dismutase; CAT: catalase; POD: peroxidase; NO_3^{-}: nitrate; NR: nitrate reductase; GDH: glutamate dehydrogenase; and TF: translocation factor.

shoots were accompanied by higher Cd levels (Figure 4(a)). Additionally, the PCA results further confirmed the different mechanisms that alleviate Cd stress in *B. napus* after lime and biochar applications. First, the root Ca level was negatively correlated with the Cd TF and Cd level in the shoots and xylem sap, which further demonstrated that an increase in root Ca could prevent Cd translocation to reduce shoot damage after lime application. Additionally, the antioxidant enzymes (e.g., SOD, CAT, and POD) and N metabolism (e.g., root N content, NO_3^{-}, NR, and GDH activity) on the lower sides were associated with biochar treatments, and the N metabolism traits were closely related to the antioxidant enzyme activities, which indicated that higher N metabolism might facilitate antioxidant enzyme synthesis to enhance Cd tolerance after biochar application. Yao et.al [25] reported that supplemental N increased activity of antioxidant enzymes (POD, SOD, and CAT) and reduced the ROS content. Additionally, the N deficiency reduced the antioxidant enzyme activities in plants [26].

5. Conclusion

B. napus growth in southern China is usually restricted by Cd stress and low N use efficiency. Large amounts of soil Ca promoted the uptake of Cd by the roots but blocked Cd on the cell wall and reduced Cd translocation from roots to shoots after lime application. In addition, lime amendment also enhanced CAT activity to Cd stress in the shoot. In contrast, biochar application immobilized soil Cd to decrease the uptake of Cd by *B. napus*. Biochar application also improved SOD, CAT, and POD activities to alleviate oxidative stress. Furthermore, the N metabolic processes were accelerated only after biochar application. Therefore, lime is more efficient in reducing the migration of Cd from belowground to crops and improving Cd tolerance, while biochar tends to facilitate N metabolism and antioxidant capacity. These studies will provide significant information for the appropriate selection of remediation approaches. These findings will improve information for the remediation mechanism of soil amendments in agricultural ecosystems and provide strategies for selecting appropriate amendments that both decrease Cd accumulation and enhance resistance in crops.

Data Availability

The datasets used or analyzed during the current study are available from the corresponding author on reasonable request.

Conflicts of Interest

We declare that we have no financial and personal relationships with other people or organizations that can inappropriately influence our work.

Authors' Contributions

Ming Lei designed this study. Zhuoqing Li and Xinqi Wang analyzed the results and wrote the original draft. Zhuoqing Li, Xinqi Wang, and Beibei Zhang performed experiments. Boqing Tie, Tehreem Ayaz, and Xia Lu reviewed and edited this paper.

Acknowledgments

This work was supported by the National Key Research & Development Plan of China (2018YFD0800700), the National Science Foundation of China (41671475), and the Changsha Municipal Natural Science Foundation (kq2202217). We are grateful to Jihai Shao and Yuexi Jiang for their experimental assistance.

Supplementary Materials

Supplementary data to this article can be found online at https://doi.org/10.1155/2022/4195119. *(Supplementary materials)*

References

[1] F.-J. Zhao and P. Wang, "Arsenic and cadmium accumulation in rice and mitigation strategies," *Plant and Soil*, vol. 446, no. 1-2, pp. 1–21, 2020.

[2] Y. Liu, H. Luo, B. Tie et al., "The long-term effectiveness of ferromanganese biochar in soil Cd stabilization and reduction of Cd bioaccumulation in rice," *Biochar*, vol. 3, no. 4, pp. 499–509, 2021.

[3] H. Du, Y. Li, D. Wan, C. Sun, and J. Sun, "Tungsten distribution and vertical migration in soils near a typical abandoned tungsten smelter," *Journal of Hazardous Materials*, vol. 429, p. 128292, 2022.

[4] M. Kamran, Z. Malik, A. Parveen et al., "Ameliorative effects of biochar on rapeseed (Brassica napus L.) growth and heavy metal immobilization in soil irrigated with untreated wastewater," *Journal of Plant Growth Regulation*, vol. 39, no. 1, pp. 266–281, 2020.

[5] F. J. Zhao, Y. Ma, Y. G. Zhu, Z. Tang, and S. P. McGrath, "Soil contamination in China: current status and mitigation strategies," *Environmental Science & Technology*, vol. 49, no. 2, pp. 750–759, 2015.

[6] M. Jaskulak and A. Grobelak, "Cadmium phytotoxicity—biomarkers," *In Cadmium Tolerance in Plants*, pp. 177–191, 2019.

[7] H. Du, N. Nie, W. Rao, L. Lu, M. Lei, and B. Tie, "Ferrihydrite-organo composites are a suitable analog for predicting Cd(II)-As(V) coexistence behaviors at the soil solid-liquid interfaces," *Environmental Pollution*, vol. 290, p. 118040, 2021.

[8] Y. Hamid, L. Tang, M. I. Sohail et al., "An explanation of soil amendments to reduce cadmium phytoavailability and transfer to food chain," *Science of The Total Environment*, vol. 660, pp. 80–96, 2019.

[9] X. Wang, X. Lu, Z. Li, Q. Cheng, Y. Zhou, and M. Lei, "Liming alters microbial community composition and its co-occurrence patterns in Cd- and Pb-contaminated agricultural soil," *Applied Soil Ecology*, vol. 166, 2021.

[10] X. Wang, X. Wu, B. Zhang et al., "Bacterial diversity rather than available Cd is the main driver of exoenzyme activity and stoichiometry after soil amendments in mildly contaminated soil," *Journal of Soils and Sediments*, vol. 22, no. 2, pp. 443–456, 2022.

[11] H. Li, H. Xu, S. Zhou et al., "Distribution and transformation of lead in rice plants grown in contaminated soil amended with biochar and lime," *Ecotoxicology and Environmental Safety*, vol. 165, pp. 589–596, 2018.

[12] G. Huang, C. Ding, F. Guo, X. Li, T. Zhang, and X. Wang, "Underlying mechanisms and effects of hydrated lime and selenium application on cadmium uptake by rice (Oryza sativa L.) seedlings," *Environmental Science and Pollution Research*, vol. 24, no. 23, pp. 18926–18935, 2017.

[13] K. Thor, "Calcium-nutrient and messenger," *Frontiers in Plant Science*, vol. 10, p. 440, 2019.

[14] L. Lu, S. Tian, M. Zhang, J. Zhang, X. Yang, and H. Jiang, "The role of Ca pathway in Cd uptake and translocation by the hyperaccumulator Sedum alfredii," *Journal of Hazardous Materials*, vol. 183, no. 1-3, pp. 22–28, 2010.

[15] Y. Zhu, H. Wang, X. Lv, Y. Zhang, and W. Wang, "Effects of biochar and biofertilizer on cadmium-contaminated cotton growth and the antioxidative defense system," *Scientific Reports*, vol. 10, no. 1, p. 20112, 2020.

[16] H. Li, Y. Yu, Y. Chen, Y. Li, M. Wang, and G. Wang, "Biochar reduced soil extractable cd but increased its accumulation in rice (Oryza sativa L.) cultivated on contaminated soils," *Journal of Soils and Sediments*, vol. 19, no. 2, pp. 862–871, 2019.

[17] X. Wu, H. Song, C. Guan, and Z. Zhang, "Boron mitigates cadmium toxicity to rapeseed (Brassica napus) shoots by relieving oxidative stress and enhancing cadmium chelation onto cell walls," *Environmental Pollution*, vol. 263, article 114546, 2020.

[18] X. Guo, J. Luo, Y. Du et al., "Coordination between root cell wall thickening and pectin modification is involved in cadmium accumulation in Sedum alfredii," *Environmental Pollution*, vol. 268, article 115665, 2021.

[19] J. Pelloux, C. Rusterucci, and E. J. Mellerowicz, "New insights into pectin methylesterase structure and function," *Trends in Plant Science*, vol. 12, no. 6, pp. 267–277, 2007.

[20] Q. Zhang, L. Zhang, T. Liu et al., "The influence of liming on cadmium accumulation in rice grains via iron- reducing bacteria," *Science of the Total Environmental*, vol. 645, pp. 109–118, 2018.

[21] Z. Wu, X. Zhao, X. Sun et al., "Antioxidant enzyme systems and the ascorbate-glutathione cycle as contributing factors to cadmium accumulation and tolerance in two oilseed rape cultivars (Brassica napus L.) under moderate cadmium stress," *Chemosphere*, vol. 138, pp. 526–536, 2015.

[22] M. Kashif Irshad, C. Chen, A. Noman, M. Ibrahim, M. Adeel, and J. Shang, "Goethite-modified biochar restricts the mobility and transfer of cadmium in soil-rice system," *Chemosphere*, vol. 242, p. 125152, 2020.

[23] M. A. Naeem, A. Shabbir, M. Amjad et al., "Acid treated biochar enhances cadmium tolerance by restricting its uptake and improving physio-chemical attributes in quinoa (Chenopodium quinoa Willd)," *Ecotoxicology and Environmental Safety*, vol. 191, p. 110218, 2020.

[24] S. Huang, G. Rao, U. Ashraf et al., "Application of inorganic passivators reduced Cd contents in brown rice in oilseed rape-rice rotation under Cd contaminated soil," *Chemosphere*, vol. 259, p. 127404, 2020.

[25] X. Yao and Q. Liu, "Changes in photosynthesis and antioxidant defenses of Picea asperata seedlings to enhanced ultraviolet-B and to nitrogen supply," *Physiologia Plantarum*, vol. 129, no. 2, pp. 364–374, 2007.

[26] Y.-L. Lin, Y.-Y. Chao, W.-D. Huang, and C. H. Kao, "Effect of nitrogen deficiency on antioxidant status and cd toxicity in rice seedlings," *Plant Growth Regulation*, vol. 64, no. 3, pp. 263–273, 2011.

[27] Y. Yang, J. Xiong, L. Tao et al., "Regulatory mechanisms of nitrogen (N) on cadmium (Cd) uptake and accumulation in plants: a review," *Science of the Total Environment*, vol. 708, p. 135186, 2020.

[28] Y. Cheng, Y. Bao, X. Chen et al., "Different nitrogen forms differentially affect Cd uptake and accumulation in dwarf Polish wheat (Triticum polonicum L.) seedlings," *Journal of Hazardous Materials*, vol. 400, article 123209, 2020.

[29] Q. Ma, X. Cao, X. Tan, L. Si, and L. Wu, "Effects of cadmium stress on pakchoi (Brassica chinensis L.) growth and uptake

of inorganic and organic nitrogenous compounds," *Environmental and Experimental Botany*, vol. 137, pp. 49–57, 2017.

[30] E. Vázquez, M. Benito, R. Espejo, and N. Teutscherova, "No-tillage and liming increase the root mycorrhizal colonization, plant biomass and N content of a mixed oat and vetch crop," *Soil and Tillage Research*, vol. 200, p. 104623, 2020.

[31] H. Cao, L. Ning, M. Xun et al., "Biochar can increase nitrogen use efficiency of Malus hupehensis by modulating nitrate reduction of soil and root," *Applied Soil Ecology*, vol. 135, pp. 25–32, 2019.

[32] O. Victoria, A. Ping, S. Yang, and E. Eneji, "Liming and nitrogen effects on maize yield and nitrogen use efficiency," *Communications in Soil Science and Plant Analysis*, vol. 50, no. 16, pp. 2041–2055, 2019.

[33] P. Saffeullah, N. Nabi, M. B. Zaman, S. Liaqat, T. O. Siddiqi, and S. Umar, "Efficacy of characterized prosopis wood biochar amendments in improving growth, nitrogen use efficiency, nitrate accumulation, and mineral content in cabbage genotypes," *Journal of Soil Science and Plant Nutrition*, vol. 21, no. 1, pp. 690–708, 2021.

[34] H. I. Jung, B. R. Lee, M. J. Chae et al., "Ascorbate-mediated modulation of cadmium stress responses: reactive oxygen species and redox status in Brassica napus," *Frontiers in Plant Science*, vol. 11, p. 586547, 2020.

[35] E. Di Carlo, A. Boullemant, and R. Courtney, "Plant available Al and Na in rehabilitated bauxite residue: a field study assessment," *Environmental Science and Pollution Research*, vol. 27, no. 14, pp. 17023–17031, 2020.

[36] X. Wang, S. Deng, Y. Zhou et al., "Application of different foliar iron fertilizers for enhancing the growth and antioxidant capacity of rice and minimizing cadmium accumulation," *Environmental Science and Pollution Research*, vol. 28, no. 7, pp. 7828–7839, 2021.

[37] B. Li, L. Yang, C. Q. Wang, S. Q. Zheng, R. Xiao, and Y. Guo, "Effects of organic-inorganic amendments on the cadmium fraction in soil and its accumulation in rice (Oryza sativa L.)," *Environmental Science and Pollution Research*, vol. 26, no. 14, pp. 13762–13772, 2019.

[38] X. Wu, H. Song, C. Guan, and Z. Zhang, "Boron alleviates cadmium toxicity in Brassica napus by promoting the chelation of cadmium onto the root cell wall components," *Science of the Total Environmental*, vol. 728, p. 138833, 2020.

[39] H. Hu and P. H. Brown, "Localization of boron in cell walls of squash and tobacco and its association with pectin (evidence for a structural role of boron in the cell wall)," *Plant Physiology*, vol. 105, no. 2, pp. 681–689, 1994.

[40] Z. T. Xiong, C. Liu, and B. Geng, "Phytotoxic effects of copper on nitrogen metabolism and plant growth in Brassica pekinensis Rupr," *Ecotoxicology and Environmental Safety*, vol. 64, no. 3, pp. 273–280, 2006.

[41] X. Zhang, Y. Zhang, X. Liu et al., "Cd uptake by Phytolacca americana L. promoted by cornstalk biochar amendments in Cd-contaminated soil," *International Journal of Phytoremediation*, vol. 22, no. 3, pp. 251–258, 2020.

[42] A. Mujeeb, I. Aziz, M. Z. Ahmed, S. K. Alvi, and S. Shafiq, "Comparative assessment of heavy metal accumulation and bio-indication in coastal dune halophytes," *Ecotoxicology and Environmental Safety*, vol. 195, p. 110486, 2020.

[43] D. Huang, X. Gong, Y. Liu et al., "Effects of calcium at toxic concentrations of cadmium in plants," *Planta*, vol. 245, no. 5, pp. 863–873, 2017.

[44] S. M. Shaheen and J. Rinklebe, "Impact of emerging and low cost alternative amendments on the (im)mobilization and phytoavailability of Cd and Pb in a contaminated floodplain soil," *Ecological Engineering*, vol. 74, pp. 319–326, 2015.

[45] Y. Zong, Q. Xiao, Z. Malik, Y. Su, Y. Wang, and S. Lu, "Crop straw-derived biochar alleviated cadmium and copper phytotoxicity by reducing bioavailability and accumulation in a field experiment of rice-rape-corn rotation system," *Chemosphere*, vol. 280, p. 130830, 2021.

[46] M. Kamran, Z. Malik, A. Parveen et al., "Biochar alleviates Cd phytotoxicity by minimizing bioavailability and oxidative stress in pak choi (Brassica chinensis L.) cultivated in Cd-polluted soil," *Journal of Environmental Management*, vol. 250, p. 109500, 2019.

[47] H. Rui, C. Chen, X. Zhang, Z. Shen, and F. Zhang, "Cd-induced oxidative stress and lignification in the roots of two Vicia sativa L. varieties with different Cd tolerances," *Journal of Hazardous Materials*, vol. 301, pp. 304–313, 2016.

[48] Y.-J. Yang, L.-M. Cheng, and Z.-H. Liu, "Rapid effect of cadmium on lignin biosynthesis in soybean roots," *Plant Science*, vol. 172, no. 3, pp. 632–639, 2007.

[49] J. C. Moura, C. A. Bonine, J. de Oliveira Fernandes Viana, M. C. Dornelas, and P. Mazzafera, "Abiotic and biotic stresses and changes in the lignin content and composition in plants," *Journal of Integrative Plant Biology*, vol. 52, no. 4, pp. 360–376, 2010.

[50] A. K. Jaiswal, N. Alkan, Y. Elad et al., "Molecular insights into biochar-mediated plant growth promotion and systemic resistance in tomato against Fusarium crown and root rot disease," *Scientific reports*, vol. 10, no. 1, pp. 1–15, 2020.

[51] F. Zhang, X. Wan, and Y. Zhong, "Nitrogen as an important detoxification factor to cadmium stress in poplar plants," *Journal of Plant Interactions*, vol. 9, no. 1, pp. 249–258, 2013.

[52] L. Qian, L. Chen, S. Joseph et al., "Biochar compound fertilizer as an option to reach high productivity but low carbon intensity in rice agriculture of China," *Carbon Management*, vol. 5, no. 2, pp. 145–154, 2014.

[53] Z. Liu, X. Wu, S. Li et al., "Quantitative assessment of the effects of biochar amendment on photosynthetic carbon assimilation and dynamics in a rice-soil system," vol. 232, Tech. Rep. 3, New Phytologist, 2021.